

Wheatland, Jonathan, Spencer, Kate, Droppo, Ian, Carr, Simon ORCID: <https://orcid.org/0000-0003-4487-3551> and Bushby, Andy (2020) Development of novel 2D and 3D correlative microscopy to characterise the composition and multiscale structure of suspended sediment aggregates. *Continental Shelf Research*, 200 . pp. 104-112.

Downloaded from: <http://insight.cumbria.ac.uk/id/eprint/5533/>

***Usage of any items from the University of Cumbria's institutional repository 'Insight' must conform to the following fair usage guidelines.***

Any item and its associated metadata held in the University of Cumbria's institutional repository Insight (unless stated otherwise on the metadata record) may be copied, displayed or performed, and stored in line with the JISC fair dealing guidelines (available [here](#)) for educational and not-for-profit activities

**provided that**

- the authors, title and full bibliographic details of the item are cited clearly when any part of the work is referred to verbally or in the written form
  - a hyperlink/URL to the original Insight record of that item is included in any citations of the work
- the content is not changed in any way
- all files required for usage of the item are kept together with the main item file.

**You may not**

- sell any part of an item
- refer to any part of an item without citation
- amend any item or contextualise it in a way that will impugn the creator's reputation
- remove or alter the copyright statement on an item.

The full policy can be found [here](#).

Alternatively contact the University of Cumbria Repository Editor by emailing [insight@cumbria.ac.uk](mailto:insight@cumbria.ac.uk).

1 **Development of novel 2D and 3D correlative microscopy to characterise the**  
2 **composition and multiscale structure of suspended sediment aggregates.**

3

4 Jonathan A.T. Wheatland <sup>a,b,c</sup>, Kate L. Spencer <sup>c</sup>, Ian G. Droppo <sup>d</sup>, Simon J. Carr <sup>c,e</sup>  
5 Andrew J. Bushby<sup>a,b,\*</sup>

6 <sup>a</sup> School of Engineering & Materials Science, Queen Mary University of London, Mile  
7 End Road, London E1 4NS, UK

8 <sup>b</sup> The NanoVision Centre, Queen Mary University of London, Mile End Road, London  
9 E1 4NS, UK

10 <sup>c</sup> School of Geography, Queen Mary University of London, Mile End Road, London  
11 E1 4NS, UK

12 <sup>d</sup> Environment and Climate Change Canada, 867 Lakehouse Road, P.O. Box 5050,  
13 Burlington, Ontario L7S 1A1, Canada

14 <sup>e</sup> Department of Science, Natural Resources and Outdoor Studies, University of  
15 Cumbria, Ambleside, Cumbria LA22 8BB, UK

16 \* Corresponding author. Email address: [a.j.bushby@qmul.ac.uk](mailto:a.j.bushby@qmul.ac.uk)

17

18 **Abstract**

19 Suspended cohesive sediments form aggregates or ‘flocs’ and are often closely  
20 associated with carbon, nutrients, pathogens and pollutants, which makes  
21 understanding their composition, transport and fate highly desirable. Accurate  
22 prediction of floc behaviour requires the quantification of 3-dimensional (3D)  
23 properties (size, shape and internal structure) that span several scales (i.e.  
24 nanometre [nm] to millimetre [mm]-scale). Traditional techniques (optical cameras  
25 and electron microscopy [EM]), however, can only provide 2-dimensional (2D)

26 simplifications of 3D floc geometries. Additionally, the existence of a resolution gap  
27 between conventional optical microscopy (COM) and transmission EM (TEM)  
28 prevents an understanding of how floc nm-scale constituents and internal structure  
29 influence mm-scale floc properties. Here, we develop a novel correlative imaging  
30 workflow combining 3D X-ray micro-computed tomography ( $\mu$ CT), 3D focused ion  
31 beam nanotomography (FIB-nt) and 2D scanning EM (SEM) and TEM (STEM) which  
32 allows us to stabilise, visualise and quantify the composition and multi-scale  
33 structure of sediment flocs for the first time. This new technique allowed the  
34 quantification of 3D floc geometries, the identification of individual floc components  
35 (e.g., clays, non-clay minerals and bacteria), and characterisation of particle-particle  
36 and structural associations across scales. This novel dataset demonstrates the truly  
37 complex structure of natural flocs at multiple scales. The integration of multi scale,  
38 state-of-the-art instrumentation/techniques offers the potential to generate  
39 fundamental new understanding of floc composition, structure and behaviour.

#### 40 **Keywords**

41 Aquatic sediments, sediment aggregates, flocs, multiscale imaging, 2D and 3D  
42 correlative microscopy

43

#### 44 **1. Introduction**

45 Cohesive fine-grained sediments and mixed sediments in suspension influence a  
46 wide array of environmental processes and material transfers, including the  
47 transport, fate and effect of carbon, nutrients, microbiota (including pathogens) and  
48 pollutants within lakes, rivers, estuaries and the marine environment (Azam & Long  
49 2001; Rusconi et al. 2014; Rummel et al. 2017). Understanding the composition and  
50 behaviour of cohesive and mixed sediments is therefore a major issue for the

51 management of aquatic environments. However, in suspension this biotic and abiotic  
52 particulate matter forms loosely bound, complex and fragile aggregates, or 'flocs'.  
53 Flocs exhibit hydrodynamics (e.g., transport dynamics and settling) that differ  
54 significantly from those of their constituent particles (Droppo 2001; Burd & Jackson  
55 2009; Manning et al. 2010).

56 To predict the movement of cohesive sediments requires accurate  
57 quantification of floc properties that control their behaviour (e.g., size, shape,  
58 porosity and density) (Soulsby et al. 2013). Additionally, an understanding of floc  
59 composition and particle associations provides a mechanistic understanding of e.g.,  
60 pathogen and pollutant transport and elucidates microbial dynamics (Liss 2002). Yet,  
61 obtaining such empirical data is challenging since flocs are inherently fragile and  
62 their properties often span several spatial scales, i.e. nm to mm-scale. Flocs are  
63 routinely characterised based on their 'gross' scale properties (e.g., external size and  
64 shape) that can be measured in situ relatively simply and non-destructively. Floc  
65 camera systems (e.g., LabSFLOC, Manning & Dyer 2002) and laser diffraction  
66 particle sizers (e.g., LISST, Agrawal & Pottsmith 2000) are commonly used and  
67 provide additional measurements of floc settling velocities. Internal floc  
68 characteristics (e.g., structure, density and porosity) cannot be measured directly  
69 using these methods, but can be estimated using Stokes' Law and the assumption of  
70 spherical shape and fractal behaviour, i.e. structural self-similarity (Winterwerp 1998;  
71 Jarvis et al. 2005). Alternatively, sub- $\mu\text{m}$  structures and the internal composition can  
72 be observed by, for instance, TEM (Leppard et al. 1996) or optical measurement of  
73 cell colonisation (e.g., Nguyen et al. 2017). However, there is no one method that  
74 allows floc structure and composition to be observed at all relevant spatial scales or  
75 that reflects the inherent 3D nature of these characteristics. A major challenge

76 therefore is the development of methods that enable empirical observation and  
77 accurate quantification of floc characteristics, correlated across multiple length-  
78 scales.

79         The combined application of two or more imaging methods, known as  
80 correlative microscopy, overcomes the resolution limitations associated with using a  
81 single imaging technique (Liss et al. 1996; Burnett et al. 2014). Previously, COM has  
82 been applied correlatively with confocal laser scanning microscopy (CLSM) and TEM  
83 enabling the investigation of floc mm-and nm-scale properties (Leppard 1992;  
84 Droppo et al. 1996; Liss et al. 1996; Leppard et al. 1996). Observations using this  
85 approach have provided valuable insights into floc structure-function relationships,  
86 highlighting the importance of floc-colonising microorganisms and their associated  
87 exopolymeric substances (EPS) (Droppo 2001; Tolhurst et al. 2002). However, the  
88 use of these imaging methods in a truly correlative manner is hindered by the  
89 specific preparation requirements, differences in contrast mechanisms, lack of  
90 overlap in resolution and their 2-dimensionality. Methods that can combine different  
91 spatial scales and similar contrast mechanisms with both 2D and 3D information are  
92 needed to understand delicate floc structures that include both organic and inorganic  
93 materials that extend across multiple scales. The combination of X-ray tomography  
94 with EM has the capability to achieve this across length-scales from mm to nm and  
95 the resolution gap can be closed. Furthermore, with similar sample preparation  
96 procedures, both imaging techniques can be applied to a single floc sample. Such  
97 methods have been used within materials science to visualise and quantify complex,  
98 multiscale structures from the cm to nm-scale (Handschuh et al. 2013; Burnett et al.  
99 2014), and in the biological sciences (Bushby et al. 2012), but have not yet been  
100 applied to study natural environmental samples.

101             $\mu$ CT and FIB-nt are both capable of imaging complex samples in 3D.  $\mu$ CT is  
102 capable of analysing volumes at a higher resolution than COM, and for small  
103 samples can reach a resolution of tens of  $\mu$ m down to submicrometre (Cnudde &  
104 Boone 2013). It is non-destructive and thus suited to imaging delicate samples,  
105 including sediments and hydrated, flocculated clays (e.g., Sharma et al. 2017; Zhang  
106 et al. 2018). FIB-nt is capable of resolutions approaching that of TEM (c. 10 nm,  
107 Holzer et al. 2004), and occupies a niche between TEM and  $\mu$ CT. Although FIB-nt is  
108 destructive, delicate samples can be stabilised to preserve their integrity during  
109 analysis (e.g., Bushby et al. 2011), and it has recently been successfully applied to  
110 investigate the internal structure of hydrated flocs (Wheatland et al. 2017).  
111 Significantly, both  $\mu$ CT and FIB-nt provide quantitative data (Holzer et al. 2004;  
112 Ketcham & Carlson 2001), which can be used to characterise suspended sediment  
113 flocs and potentially parameterise computational models that describe floc  
114 behaviour.

115            The aim of this study is to develop a correlative workflow that enables  
116 observation, characterisation and quantification of natural suspended sediment floc  
117 structure and composition from the mm to nm-scale for the first time. This workflow,  
118 which combines 3D  $\mu$ CT and FIB-nt with 2D SEM and STEM, is applied to the  
119 investigation of natural estuarine sediment flocs. Based on feature greyscale, size  
120 and morphology criteria are developed to distinguish floc components (e.g., clay  
121 minerals, bacteria etc.) observed at different spatial scales, which are used to  
122 segment the datasets.

123

124 **2. Materials and Methods**

125 **2.1. Considerations for Correlative Imaging**

126 Several challenges exist for the correlative imaging of sediment flocs. Firstly, fragile  
127 flocs must be sampled and stabilised and contrast agents (e.g., stains) applied to  
128 enable feature recognition using different imaging modalities operating at different  
129 scales (Wheatland et al. 2017).  $\mu$ CT and EM share similar contrast mechanisms  
130 allowing object(s) of interest to be identified and correlated between datasets.  
131 However, electron-dense stains must be introduced to allow organics to be  
132 distinguished. Secondly, to achieve correlation between the different imaging  
133 methods, datasets must be registered using fiducial markers that can be imaged by  
134 all methods. Thirdly, the process of identifying nm-scale datasets nested within mm-  
135 scale samples is represents a significant challenge (Bushby et al. 2011; Burnett et al.  
136 2014). Therefore, workflows must follow a targeted approach whereby a sample is  
137 sequentially imaged at a finer scale and/or by a complimentary modality, the data  
138 from which is used to selected further regions of interest (RoI) for analysis at higher  
139 resolutions. Finally, the imaging methods used should each adequately resolve both  
140 the biotic and abiotic floc components for correlation. For example,  $\mu$ CT maps X-ray  
141 attenuation and hence images the density of an object or concentration of floc  
142 constituents at the  $\mu$ m to mm-scale. In comparison, SEM (using secondary and  
143 backscattered electrons) provides information on morphology and elemental  
144 composition at the nm to  $\mu$ m-scale. Combining this information enables important  
145 features (e.g., a pore space, clay mineral or bacteria) to be identified at different  
146 scales and resolutions. Once features have been identified, they can be segmented,  
147 quantified and visualised in both  $\mu$ CT and FIB-nt.

148

149 **2.2. Floc Capture and Stabilisation**

150 Natural sediment collected from the Thames Estuary, SE England. These sediments  
151 are typically fully saline, fine grained silty clays with organic content typically < 10%  
152 (measured as % loss on ignition, e.g., O'Shea et al. 2018). Sediment was added to  
153 an artificial seawater solution (Sigma sea salts 34 g L<sup>-1</sup>) and gently agitated using a  
154 magnetic stirrer to induce flocculation. Fragile flocs were sampled following the  
155 protocol outlined in Droppo et al. (1996), which involved settling flocs directly into  
156 plankton chambers and immobilising flocs in agarose gel.  $\mu$ CT scans of a test  
157 sample (FS0, see Fig. S1 of Supplementary Materials) were conducted in order to  
158 assess potential artefacts associated with this technique (e.g., particle-particle  
159 overlap, Droppo et al. 1996). Immobilised flocs were subsequently prepared for  
160 imaging following the block staining protocol outlined in Wheatland et al. (2017). Floc  
161 samples were rendered vacuum stable by resin embedding, which included the  
162 addition of electron dense stains (e.g., uranyl acetate etc.) to improve the contrast of  
163 organic constituents. Following resin embedding, fiducial markers (aluminium wire, c.  
164 0.5 mm diameter) were implanted in the base of each resin block for the purpose of  
165 data co-registration (see Section 2.3). Aluminium was selected as it could be easily  
166 distinguished from natural sedimentary material using all imaging methods  
167 (Hands Schuh et al. 2013).

168

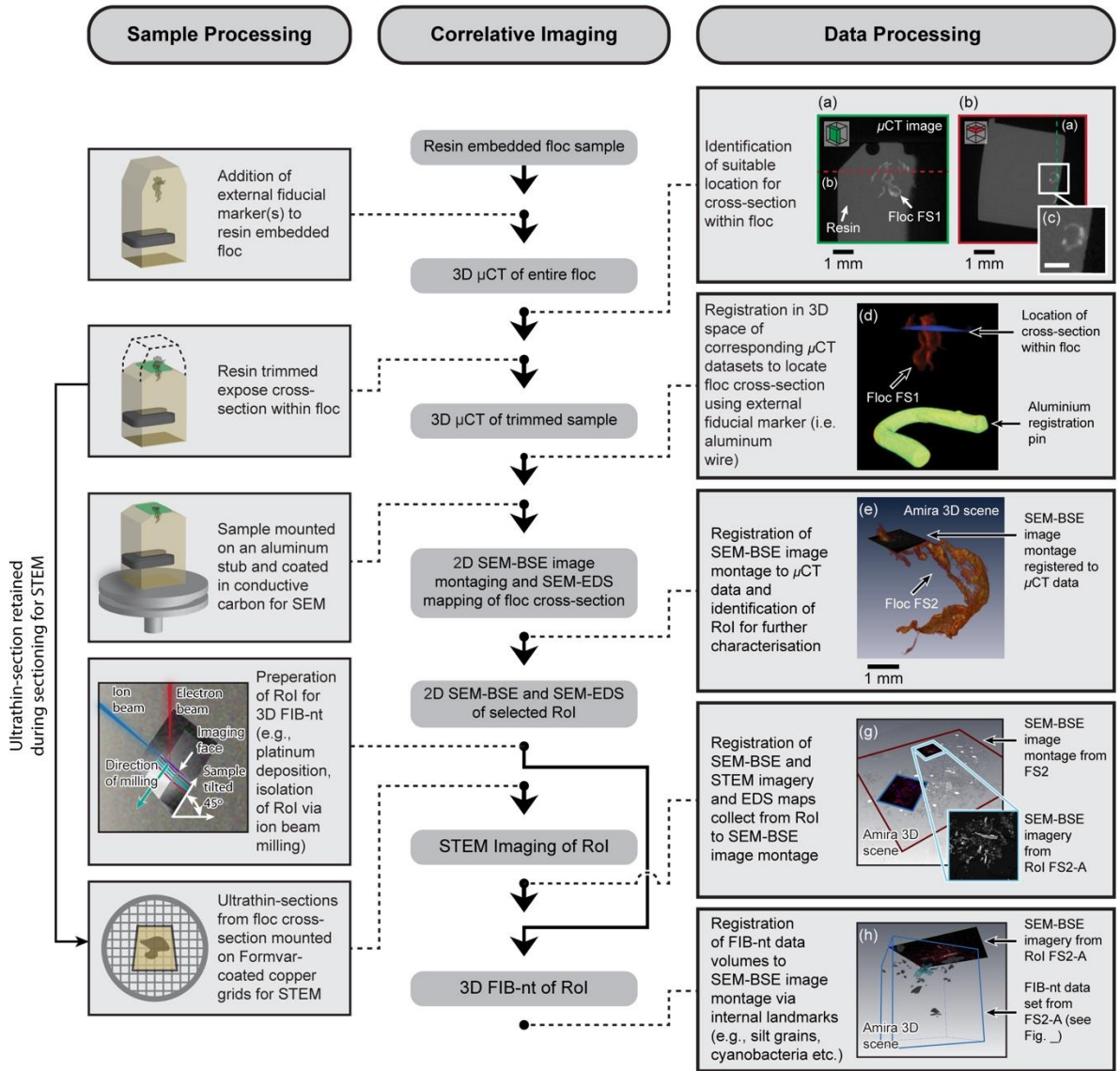


**Figure 1.** Flow diagram outlining the various stages in the correlative imaging workflow, including steps required for sample and data processing. Images (a) and (b) are orthogonal slices from the  $\mu$ CT scan of floc FS1. Grey-scale variations reflect regions of high and low X-ray attenuation (c), and indicate variability of floc constituents and structure at the sub-voxel scale. This information helps guide the selection of a suitable site for a cross-section within the floc which is exposed via ultramicrotomy. The precise location of the cross-section within the floc is then verified by re-scanning the sample using  $\mu$ CT and registering the two corresponding  $\mu$ CT datasets using the aluminium registration pin (d). 2D SEM-BSE image montages of the floc cross-section, obtained to identify suitable Rol for further analysis, are then registered to the  $\mu$ CT data (e). Following 2D SEM-BSE imaging, Rol are prepared for 3D FIB-nt (h). 2D SEM-BSE and STEM imagery and 3D FIB-nt data obtained from Rol can be registered to the image montage based on ‘internal’ fiducial markers (e.g., silt grains, cyanobacteria etc.) that can be identified in the corresponding datasets (g and h).

### 170 **2.3. Description of the Correlative Workflow**

171 The correlative workflow developed for investigating floc composition and multiscale  
172 structure is shown in Fig. 1. Low-resolution  $\mu$ CT scans (3D pixel or 'voxel' size, c. 10  
173  $\mu\text{m}^3$ ) were initially conducted to characterise floc size and morphology and identify  
174 RoI for further analysis (Fig. 1a and b). At this resolution individual floc constituents  
175  $<100\ \mu\text{m}$  (e.g., bacteria and clay minerals) cannot be resolved. However, variations  
176 in X-ray attenuation (Fig. 1c and Fig. S2 of Supplementary Materials) indicate the  
177 variability of floc constituents and structure at the sub-voxel scale. Subsequently,  
178 selected RoIs were exposed by trimming the resin-block using an ultramicrotome  
179 (Leica UCT ultramicrotome), creating a smooth cross-section suitable for 2D SEM  
180 and 3D FIB-nt. During this process, ultrathin-sections (thickness, 70–100 nm) cut  
181 directly adjacent to the cross-section were retained for STEM (Fig. 1).

182 The accurate co-registration of  $\mu\text{m}$  and nm-scale EM datasets with mm-scale  
183  $\mu$ CT scans relied on the location and characterisation of the cross-section created  
184 within the floc. Therefore, samples were re-scanned using  $\mu$ CT following  
185 ultramicrotomy to locate the floc cross-section within the original  $\mu$ CT data (Fig. 1d).  
186 This was facilitated by 'external' fiducial markers (aluminium wire) identifiable in the  
187 corresponding  $\mu$ CT datasets (Fig. 1d, see section 3.1.1). To ensure these repeat  
188 scans were directly comparable to the original  $\mu$ CT data and accurate co-  
189 registration, the position of the mechanical stage, manipulator settings (i.e. voltage  
190 and current) and resolution were kept constant.

191 2D SEM-BSE image montaging of the cross-section (block-face SEM) then  
192 provided the context within which to locate 3D FIB-nt volumes and 2D STEM  
193 imagery based on identification of 'internal' landmarks within the floc (Fig. 1g and h).  
194 Landmarks were selected that could be identified across scales and imaging

195 modalities, e.g., silt grains and cyanobacteria (see Table 1). Image montages were  
 196 obtained by systematic imaging using 2D SEM, resulting in 10's – 100's of images  
 197 that were stitched together to provide a 'panoramic' view of the entire cross-section  
 198 (pixel resolution, c. 100 nm<sup>2</sup>). Following SEM imaging, elemental maps were  
 199 obtained from selected ROI via energy dispersive X-ray spectroscopy (SEM-EDS)  
 200 which, in conjunction with contrast and morphological information from SEM  
 201 imagery, enabled identification and mapping of materials.

202 2D SEM imagery and EDS maps informed the selection suitable sites for 3D  
 203 FIB-nt. Representativity is a key consideration when selecting parameters for FIB-nt  
 204 (i.e. volume size and resolution), and must be optimised to resolve features of  
 205 interest and ensure that a representative number of particles are characterised for  
 206 statistical analysis (Bushby et al. 2011). Natural flocs are compositionally complex,  
 207 containing particles of varying morphology and size (e.g., blocky silt grains, platy  
 208 clays, and filamentous organics), and high-resolution datasets are desirable (10-15  
 209 nm) to characterise individual particles. However, a trade-off must be made between  
 210 the resolution and volume size to ensure the  $\mu$ m-scale structures into which floc  
 211 constituents are organised are adequately characterised.

212

Imaging Technique; Successive Techniques Applied $\longrightarrow$							
CT Datasets		SEM-BSE Montaging		SEM and STEM		FIB-nt	
Material	Identification Criteria	Material	Identification Criteria	Material	Identification Criteria	Material	Identification Criteria
<i>Floc</i>	Mid-range greyscale (c. 19,000 – 40,000)	<i>Floc Matrix</i>	Material with diameter c. <10 $\mu$ m, low to mid-range greyscales (c. 20 – 200)	<i>Clay Minerals</i>	2D planar morphology, size c. <5 $\mu$ m, mid-range greyscale (c. 10 - 170)	<i>Clay minerals</i>	3D planar morphology, size c. <5 $\mu$ m, mid-range greyscale (c. 10 - 170)
	Variability in composition and structure at the sub-voxel scale		Regions of low and high occupation	<i>Microbial Cells</i>	Small size (c. <10 $\mu$ m), high greyscale (c. 200 - 250),	<i>Cell Morpho-type</i>	Five cell morphotypes recognised based on

	recognised based on X-ray attenuation: low greyscale values (c. 25,000 – 40,000) correlated to regions of low-occupation, high greyscale values (c. 19,000 – 25,000) correlated to regions of high-occupation	identified based on greyscale, e.g., low occupation c. <50, high occupation c. >70		differential staining of subcellular structures		criteria outlined in Dazzo & Niccum (2015) (see Fig. 5)	
					<i>Intra-cellular Integrity</i>	Three categories of intracellular integrity (indicative of metabolic state) recognised based on criteria outlined by Heissenberger et al. (1996) (see Fig. 5)	
			<i>Organo-Mineral Debris</i>	Geometric structure, mid-range greyscale (c. 10 - 170)	<i>Organo-Mineral Debris</i>	Geometric structure, mid-range greyscale (c. 10 - 170)	
			<i>EPS</i>	Fibrillar material, diameter (2 – 15 nm)	NA		
		<i>Non-Clay Minerals</i>	Blocky/irregular morphology, particle size c. 5 – 40 µm, mid-range greyscales (c. 20 – 100)	<i>Non-Clay Minerals</i>	Blocky/irregular morphology Particle size c. 5 – 40 µm, mid-range greyscales (c. 20 – 100)	<i>Non-Clay Minerals</i>	Blocky/irregular morphology Particle size c. 5 – 40 µm, mid-range greyscales (c. 20 – 100)
		<i>Bio-Organic Material</i>	Irregularly shaped, high greyscales (c. 200 – 255)	<i>Bio-Organic Material</i>	Irregularly shaped, high greyscales (c. 200 – 255)	<i>Bio-Organic Material</i>	Irregularly shaped, high greyscales (c. 200 – 255)
		<i>Resin External to the Floc</i>	Resin external to the floc matrix, grey-scale (c. 0 – 20)	<i>Resin External to the Floc</i>	0 – 20	NA	
<i>Resin</i>	Low greyscale (c. 7,000 – 17,000)	<i>Resin Filled Pore-Space</i>	Resin filled pores within the floc matrix, low grey-scale (c. 0 – 20). NB only possible to resolve pores with diameter >30 µm	<i>µm-Scale Pore</i>	Resin filled pores within the floc matrix, low grey-scale (c. 0 – 20), diameter <10 µm	<i>µm-Scale Pore</i>	Resin filled pores within the floc matrix, low grey-scale (c. 0 – 20), diameter <10 µm
				<i>nm-Scale Pores</i>	Resin filled pores within the floc matrix, low grey-scale (c. 0 – 20), diameter >10 µm	<i>nm-Scale Pores</i>	Resin filled pores within the floc matrix, low grey-scale (c. 0 – 20), diameter >10 µm

---

<i>Aluminium</i>	High greyscale
<i>Pin</i>	(c. 45,000 – NA 65,535)

---

213 **Table 1.** Materials identified within the various 2D and 3D datasets, and the criteria used for their  
214 identification/segmentation, e.g., size, morphology, and greyscale characteristics. Note, that the  $\mu$ CT  
215 are 16-bit and therefore have a pixel depth of 65,535 greyscales, whereas the SEM and STEM  
216 imagery and FIB-nt data volumes are 8-bit with a 256 greyscale range.

217

218 Ultrathin-sections collected adjacent to the surface of the cross-section during  
219 ultramicrotomy were mounted on Formvar-covered copper grids (Gilder Grids) and  
220 coated in conductive carbon for STEM. STEM provided details of the pore space  
221 that cannot be obtained using SEM. Additionally, high-resolution elemental analysis  
222 via STEM X-ray spectroscopy (STEM-EDS) conducted on floc cross-section (SEM-  
223 EDS) enabled the precise classification of individual floc constituents that cannot be  
224 achieved via SEM-EDS.

225

## 226 **2.4. Acquisition of Image Data**

### 227 **2.4.1. 3D $\mu$ CT**

228  $\mu$ CT scans were performed using a Nikon Metrology XT-H 225 (Tokyo, Japan)  
229 micro-tomograph. This scanner was configured with a 25-225 kV 0-2000  $\mu$ A X-ray  
230 source with tungsten reflection target capable of generating polychromatic X-rays  
231 (focal spot size, c. 3  $\mu$ m), and a Perkin Elmer (Waltham, Massachusetts, USA) 16-bit  
232 flat-panel detector. Scan parameters were set to optimise contrast and resolution  
233 (voltage 150 kV; current 160  $\mu$ A; acquisition time between projections 2829 ms) with  
234 2-frame averaging. Maintaining the same scan parameters for all  $\mu$ CT scans  
235 ensured comparability between datasets. The greyscale values of resulting

236 projections represented differences in X-ray energy attenuation, related to material  
237 density and the attenuation coefficient of the materials being imaged.

238

#### 239 **2.4.2. 2D SEM, STEM and EDS**

240 2D SEM image montaging (block-face SEM) was conducted using an FIB-SEM (FEI  
241 Quanta 3D FEG, Hillsboro, Oregon, USA) fitted with a low-kV backscattered electron  
242 detector. Backscattered electron (BSE) images were collected at 3 kV accelerating  
243 voltage and 4 nA beam current to minimise the electron beam interaction volume  
244 and improve the spatial resolution of the BSE signal. Greyscale contrast of BSE  
245 images typically reflects composition. Systematic imaging of the floc cross-section  
246 generated 100's of images (pixel resolution, c. 30 – 60 nm<sup>2</sup>). Images were  
247 subsequently stitched together into montages using the Grid/Collection Stitching  
248 plugin in open source software FIJI/ImageJ (Preibisch et al. 2009).

249 SEM-EDS elemental maps, STEM images and STEM-EDS point spectra were  
250 obtained using an FEI Inspect-F SEM fitted with a split field STEM detector  
251 (Hillsboro, Oregon, USA) and equipped with an Oxford Instruments (Oxford, UK)  
252 INCA X-act energy dispersive X-ray spectrometer. For low-resolution SEM-EDS  
253 mapping of the entire floc cross-section and high-resolution elemental mapping of  
254 Rol (see section 2.3) an accelerating voltage of 10 kV (counting period, 10 – 30 min).  
255 Counting periods varied between Rol and were selected to minimise damage to the  
256 sample surface. Dark-field STEM imaging of the ultrathin-sections was achieved at  
257 an accelerating voltage of 30 kV. Point spectra (STEM-EDS) were obtained from  
258 individual particles, at an accelerating voltage of 10 kV.

259

### 260 **2.4.3. 3D FIB-nt Data Volumes**

261 3D FIB-nt was performed using a FIB-SEM (FEI Quanta 3D FEG, Hillsboro, Oregon,  
262 USA) following the protocol outlined by Bushby et al. (2011). This relied on using the  
263 automated serial sectioning and imaging software Slice & View software (FEI  
264 Hillsboro, Oregon, USA). Experimentation revealed an accelerating voltage of 30 kV  
265 and a current of 0.5 – 5 nA for the ion beam to be optimal for milling. Images were  
266 captured using the BSE signal detector operated at a voltage of 3 kV and current of  
267 4 nA, selected to match those used for 2D SEM (see section 2.4.2). The accuracy of  
268 FIB-nt relies on the stability of the FIB during milling and its ability to maintain regular  
269 intervals (i.e. slice thicknesses) between consecutive slices. An automated  
270 correction algorithm was applied during the serial sectioning procedure, which  
271 reduces or eliminates drift phenomena.

272

### 273 **2.4.4. Reconstruction and Segmentation of the 3D Data**

274 The product of  $\mu$ CT and FIB-nt are 2D projections/images of the sample/volume of  
275 interest that must be reconstructed to generate 3D volumes for visualisation and  
276 quantification. The reconstruction of  $\mu$ CT datasets was conducted using CTPro 3D  
277 (Nikon, Tokyo, Japan). Each scan generated 1,609 raw X-ray projections, yielding  
278 volumes with dimensions of  $1,024 \times 1,024 \times 1,024$  voxels (voxel size resolution, 10  
279  $\mu\text{m}^3$ ). During reconstruction artefacts (e.g., beam hardening, Ketcham & Carlson  
280 2001) were addressed by the application of specific algorithms. FIB-nt datasets were  
281 reconstructed following the protocol outlined by Bushby et al. (2011) using  
282 FIJI/ImageJ v2 (Schindelin et al. 2012). The number of images comprising FIB-nt  
283 datasets varied depending on the size of the analysed volume, ranging between 400

284 – 600 images. During setup for FIB-nt the mill thickness was adjusted to match the  
285 pixel resolution of the images, ensuring an isotropic voxel size suitable for  
286 quantitative analysis (Bushby et al. 2012).

287

#### 288 **2.4.5. Visualisation and Quantification of the Correlative Datasets**

289 The quantification and visualisation of both  $\mu$ CT and FIB-nt datasets was conducted  
290 in in FIJI/ImageJ and required material segmentation, i.e. the classification of  
291 material phases based on greyscale values and/or shape, a critical stage in image  
292 processing (Cnudde & Boone 2013). Segmentation was achieved via greyscale  
293 thresholding or using a semi-automated segmentation tool plugin (Trainable WEKA  
294 Segmentation, TWS v2.1.0) capable of machine learning (Arganda-Carreras et al.  
295 2017). The choice between these segmentation methods was guided by appraisal of  
296 dataset complexity, including the number of bulk phases and the overlap between  
297 phase greyscale envelopes common in natural environmental materials. Resulting  
298 binary volumes were then quantified using the 3DRoiManager plugin (Ollion et al.  
299 2013), which provided quantitative measurements of material properties, e.g., size,  
300 shape and greyscale intensities etc.

301

#### 302 **2.4.6. Co-Registration of Datasets**

303 The process of aligning multiscale datasets (i.e. co-registration) is a critical aspect of  
304 the correlative workflow, allowing information obtained using different imaging  
305 modalities and different spatial scales to be directly related. Co-registration of the  
306 multiscale 2D/3D datasets was achieved in the visualisation software Avizo (FEI  
307 Visualisation Sciences Group, Berlin, Germany). The success of registration is  
308 dependent upon the identification of fiducial markers in the different datasets. Co-

309 registration of  $\mu$ CT datasets relied upon the identification of the aluminium wire  
310 implanted within the resin block, whilst internal landmarks (e.g., silt particles, bacteria  
311 etc.) were used in the co-registration of higher resolution 2D and 3D datasets. Fig. 1  
312 shows the sequence of steps taken to co-register the correlative datasets. Coarse  
313 alignment was manually conducted using the Transform Editor tool within Avizo,  
314 while fine registration was conducted automatically using the Landmark Surface  
315 Warp module applied using a rigid transformation algorithm.

316

### 317 **3. Results and Discussion**

#### 318 **3.1. Overview of the Multiscale Datasets**

##### 319 **3.1.1. 3D Floc Sub-mm Structure and Internal Density**

320 Volumetric renderings of three floc samples (FS1, FS2 and FS3) generated based  
321 on the  $\mu$ CT data (resolution, c.  $10 \mu\text{m}^3$ ) are shown in Fig. 2. For each 3D  
322 reconstruction greyscale contrast (16-bit pixel depth, e.g., 65,536 greyscales)  
323 between the flocs, surrounding resin and aluminium fiducial markers was sufficient to  
324 allow segmentation based on simple thresholding. This is illustrated in Fig. 1a and b  
325 that show cross-sectional greyscale images taken from the reconstructed  $\mu$ CT scan  
326 of FS1, in which the floc and surrounding resin are easily distinguishable. Scan  
327 parameters were kept constant for each of the flocs, and thus datasets are directly  
328 comparable. Table 1 details the criteria (e.g., greyscale range, size and shape etc.)  
329 for identify the different material phases; i) resin ii) floc, and iii) aluminium registration  
330 pin. The result of the segmentation procedure was a binary masks which formed the  
331 basis for subsequent visualisations and quantitative analysis (Fig. 2 and Table 2).

332 Quantitative analysis of the floc samples showed FS2 to have the largest  
333 volume, with a total occupied volume (i.e. voxel count) of  $5.04 \times 10^8 \mu\text{m}$  (Table 2).

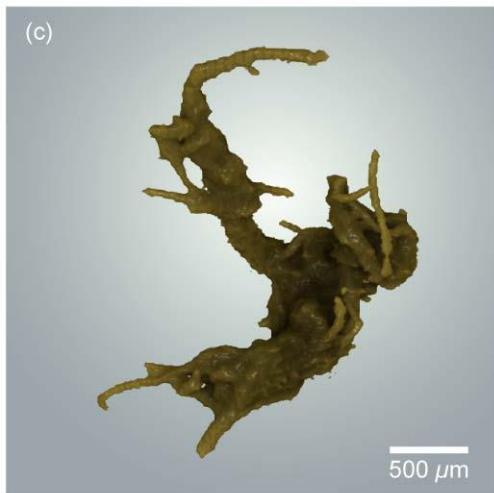
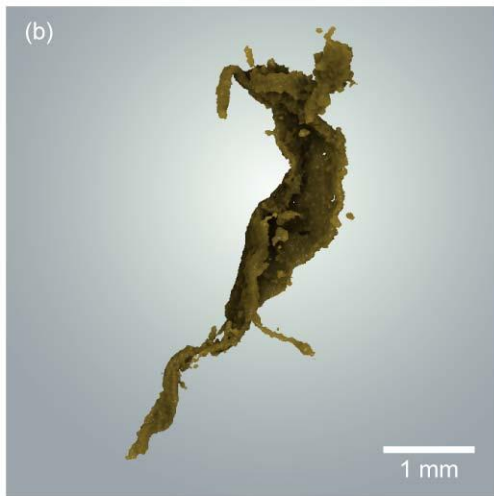
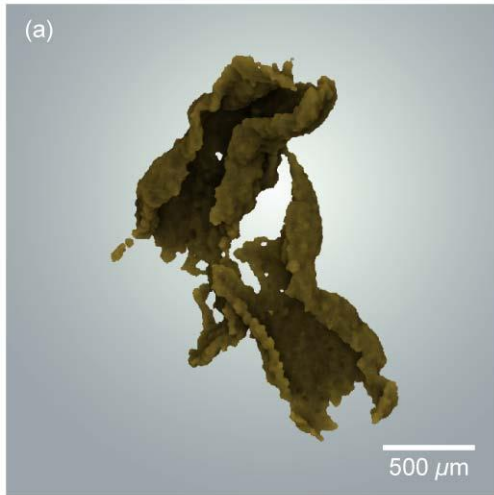


**Figure 2.** 3D visualisations of the floc samples FS1 (a) and FS2 (b) and FS3 (c) generated in Drishti from X-ray  $\mu\text{CT}$  data.

334 Descriptions of floc diameter ( $D$ ) and height to width ratios ( $H/W$ ) were made using  
335 the Feret diameter, i.e. the distance between two parallel planes enclosing an object.

336 Based on these the floc samples can be described as macroflocs ( $D > 160 \mu\text{m}$ ;  
 337 Manning & Dyer 2002) that exhibit elongate ( $H/W > 2:1$ ) and highly contorted  
 338 morphologies. Flocs FS2 and FS3 exhibit filamentous protuberances projecting  
 339 beyond their peripheries, likely related to the presence of cyanobacteria (confirmed  
 340 by SEM, STEM and FIB-nt dataset, see sections 3.1.2, 3.1.3 and 3.1.4). FS1 was  
 341 observed to differ significantly from FS2 and FS3, being composed of three distinct  
 342 sub-units, connected by narrow linkages  $c. \leq 30 \mu\text{m}$ . Each of the floc samples  
 343 exhibited regions of high and low X-ray attenuation (Table 1 and Fig. 2c and Fig. S2  
 344 of Supplementary Materials). The distribution of regions of high attenuating elements  
 345 within floc FS2 are shown in a 3D rendering in Fig. S2 of Supplementary Materials.  
 346 This information provided a means of identifying RoI for further analysis (see Section  
 347 3.1.2 and Fig. 3a-c and Fig. S3 of Supplementary Materials).

348

Floc Sample	Floc Volume ( $\mu\text{m}^3$ )	Feret Diameter ( $\mu\text{m}$ )			H/W
		Major	Intermediate	Minor	
FS1	$1.95 \times 10^8$	2414.54	1298.65	631.29	3:1
FS2	$5.04 \times 10^8$	11183.83	755.82	266.06	4:1
FS3	$2.44 \times 10^8$	945.03	800.19	323.23	2:1

349 **Table 2.** 3D quantitative measures of floc geometry (volume and Feret diameter) and  
 350 shape (height/width ratio).

351

### 352 **3.1.2. 2D Floc Micrometre-Structure and Composition Revealed in** 353 **Cross-Section**

354 Fig. 3c shows the 2D SEM-BSE image montage collected from the cross-section of  
 355 floc FS1 (resolution,  $c. 60 \text{ nm}^2$ ), (FS2, resolution,  $c. 30 \text{ nm}^2$  and individual SEM-EDS

356 elemental maps are shown in Fig. S2 and Fig. S4 respectively). Similar to  $\mu$ CT,  
 357 greyscale contrast (8-bit pixel depth, e.g., 256 greyscales) was sufficient to allow  
 358 flocculated material to be segmented from surrounding resin. However, the higher  
 359 resolution of SEM also enabled the recognition of additional floc components, which  
 360 could be classified based on particle size, shape and greyscale value and further  
 361 validated by comparison with SEM-EDS elemental maps. Four additional materials  
 362 were identified; i) resin filled pore-space, ii) floc matrix (e.g., clays, unicellular  
 363 bacteria, organo-mineral debris), iii) individual non-clay mineral grains (e.g., quartz,  
 364 feldspar and mica) and iv) large bio-organic and organic structures (e.g., organic  
 365 detritus, diatoms, cyanobacteria) (Table 1 and Fig. 3d). Particles  $<10\ \mu\text{m}$  (e.g., EPS,

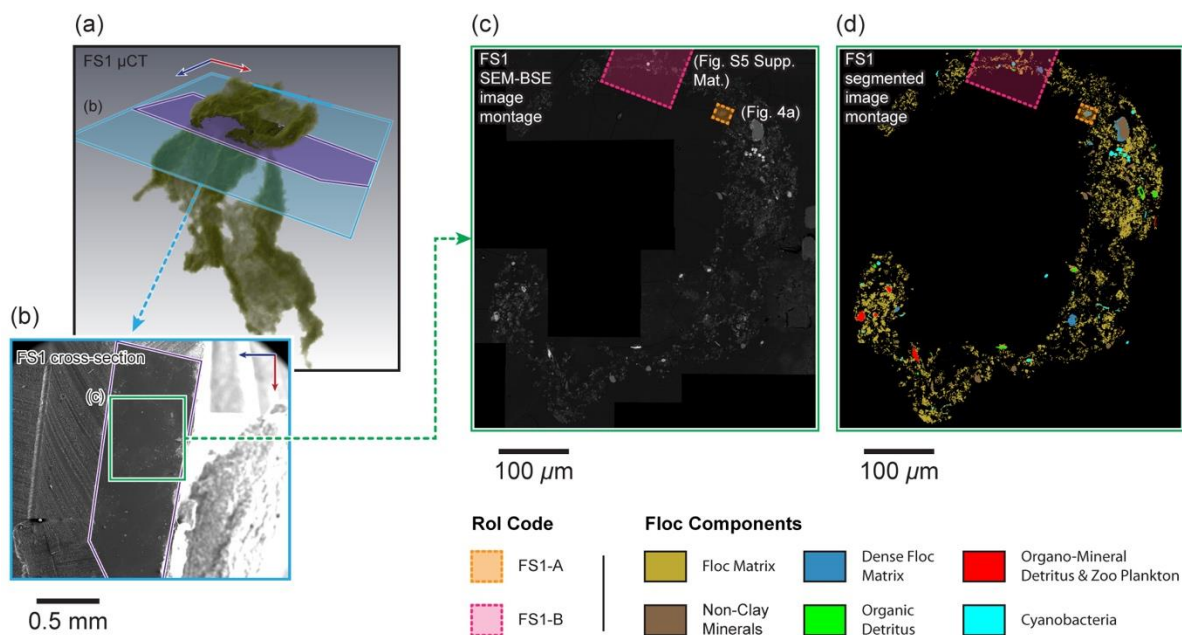


**Figure 3.** Analysis of the cross-section located in floc FS1. The location of the cross-section created within FS1 is shown in (a) and the region of the cross-section containing the floc is shown in (b). The trapezoidal shape of the sectioned block is highlighted in purple both in (a) and (b), while the boundary of the SEM image of the cross-section shown in (b) is defined in 3D space in (a) in blue. The SEM-BSE image montage (c) obtained from the cross-section through floc FS1 enabled the identification of floc constituents (d) and characterisation of floc structure in 2D. The locations of Rol selected for further analysis are shown in (c) and (d).

366 clay minerals and unicellular bacteria) could not be accurately segmented and were  
367 identified collectively as 'floc matrix'. The floc matrix is likely to be compositionally  
368 complex, however, SEM-EDS revealed strong signals for Fe, Al/Si and Si (Fig. S4 of  
369 Supplementary Materials), indicating the presence of iron oxyhydroxides, clay  
370 minerals and silicates. Constituents were unevenly distributed within the floc matrix,  
371 with regions of low occupation characterised by high porosity and low greyscale  
372 values (c. <50) and regions of high occupation exhibiting low porosity and high  
373 greyscale values (c. >70) (Fig. 3 and Table 1).

374 Non-clay mineral grains were differentiated based on their blocky/irregular  
375 morphology, uniform greyscale and elemental signature (Si, Fe). In comparison, bio-  
376 organic material and biota could be identified relatively easily based on their high  
377 greyscale values (c. 200 – 255) due to heavy metal (Pb, Os and U) staining (see  
378 also elemental phase map, Fig. S4 of Supplementary Materials). Strong signals for  
379 Pb, Os and U related to heavy metal-stained organics, typically large features  
380 (diameter, >10 µm) such as cyanobacteria and organic detritus, while an associated  
381 signal of Si (blue) was indicative of eukaryotic plankton (e.g., diatom, foraminifera).

382

### 383 **3.1.3. 2D Submicrometre and Nanometre Structure and Composition of** 384 **Selected Rol**

385 For each floc several Rol were identified based on structural and/or compositional  
386 characteristics revealed in SEM-BSE imagery and SEM-EDS elemental maps (see  
387 Section 3.1.2). Fig. 3 and Fig. S3 of Supplementary Materials show the locations of  
388 Rols selected for FS1 and FS2 respectively. Rols were targeted to either  
389 characterise further floc nm composition and particle-particle interactions via STEM,

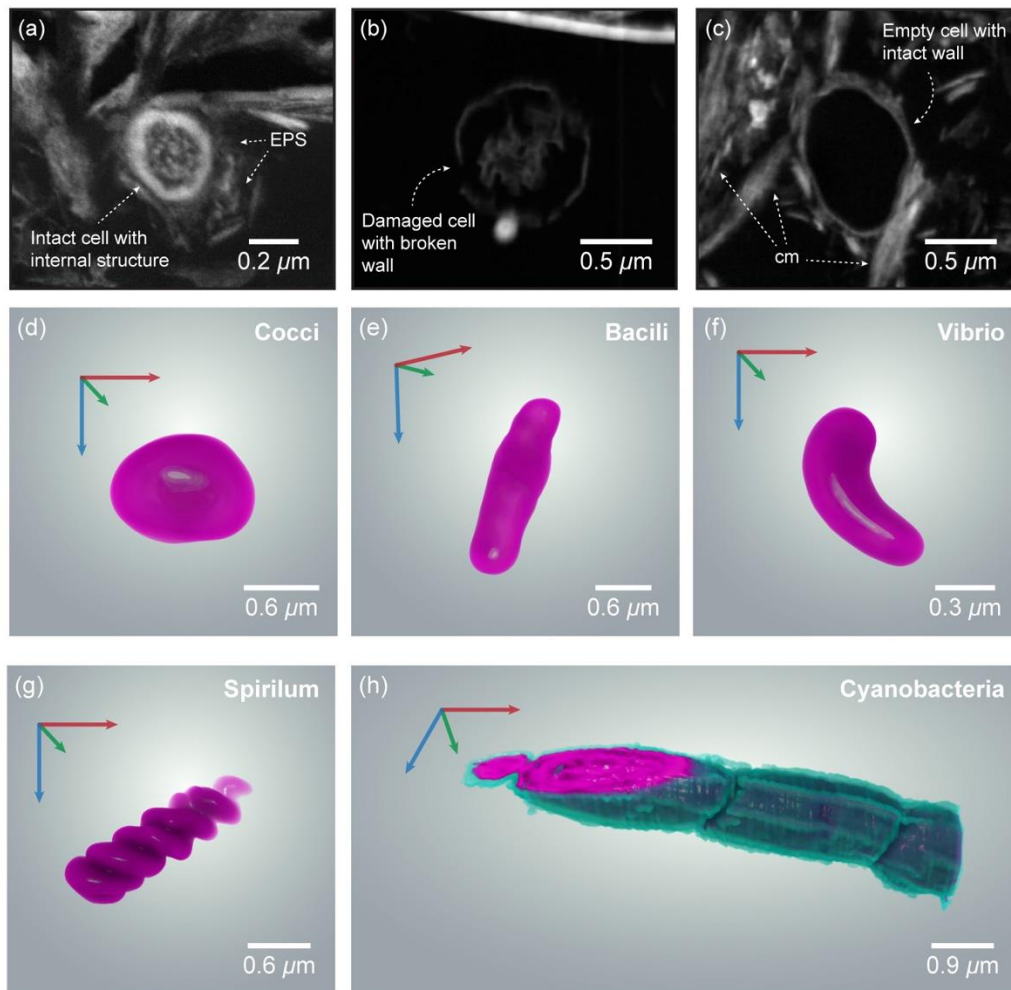


**Figure 5.** Characterisation of bacterial cells. (a – c) STEM images showing examples of the three categories of intracellular integrity used as an indicator of the fidelity of stabilised flocs to their original structure. (d – g) Examples of different bacterial cellular morphologies reconstructed based on 3D FIB-nt data. (a) intact bacteria displaying an undamaged cell wall, cytoplasm (grainy structure) and nucleoplasm (denser region towards the centre of the cell); (b) damaged bacterial cell with a broken cell wall and degraded cytoplasm and/or nucleoplasm; (c) empty cell lacking plasma. (d) cocci, (e) bacilli, (f) vibrio, (g) spirillum and (h) cyanobacteria.

390 or selected for SEM imaging to define submicrometre structure. Selected SEM-BSE  
 391 (resolution, c. 25 - 30 nm<sup>2</sup>) and STEM (resolution, c. 5 - 10 μm<sup>2</sup>) imagery and  
 392 corresponding SEM-EDS elemental maps are shown in Fig. 4 and Fig. S5 of  
 393 Supplementary Materials.

394 The four main floc constituents (pore-space, floc matrix, non-clay mineral  
395 grains, and large bioorganic and organic structures) were also identified in SEM-BSE  
396 and STEM imagery. However, the higher resolution enabled further distinction  
397 between materials within the floc matrix: i) clay minerals, ii) microbial cells, iii)  
398 organo-mineral debris, and iv) EPS (Table 1). Microbial cells could be easily  
399 identified due to their high greyscale values (c. >200) and differential staining of  
400 subcellular structures (Fig. S5 of Supplementary Materials). High-resolution STEM  
401 imagery revealed internal/external cell structure allowing the classification of  
402 microbes based on their metabolic state (Heissenberger et al. 1996) as: i) intact, ii)  
403 damaged and iii) empty (e.g., Fig. 5a – c). Whilst the resolution of SEM imagery  
404 prevented the detection of EPS 2 – 20 nm in diameter (Leppard 1992), its presence  
405 is confirmed by STEM imagery (Fig. S6 of Supplementary Materials). EPS was  
406 observed to be closely associated or ‘bound’ to the cell walls of metabolically active  
407 microbes, whilst ‘soluble’ EPS exuded by microorganisms was found throughout the  
408 floc matrix and often associated with clay minerals (Fig. S6 of Supplementary  
409 Materials).

410 To investigate density variations within the floc matrix (see Section 3.1.2, Fig.  
411 3 and Figs. S3 and S4 of Supplementary Materials), Rols FS1-A and FS2-B (Fig. 4a  
412 and e) were selected to encompass regions exhibiting high and low occupation.  
413 Within both high and low occupation regions clay minerals were rarely observed in  
414 isolation, but were observed in units of 10’s of particles. STEM imagery revealed  
415 several common particle associations, including units of clay platelets aligned face-  
416 to-face and/or edge to face, and clay minerals arranged around a central bacterium  
417 (Fig. S6 of Supplementary Materials). Low density regions of the floc matrix mainly  
418 consisted of particle associations arranged in open, ‘card-house’ structures, and

419 were highly porous (Fig. 4a). STEM showed the nanometre pore space between  
420 primary particles filled with exopolymeric material, whilst EPS was notably absent in  
421 the larger micrometre pore channels (Fig. S6 of Supplementary Materials). In  
422 comparison, high density areas consisted primarily of closely packed clay minerals  
423 dispersed with pyrite (Fe+S) (Fig. 4c), and had a lower porosity and high organic  
424 signal (Fig. 4d).

425

#### 426 **3.1.4. 3D Submicrometre-Structure and Composition of Selected Rol**

427 Volumetric renderings of two FIB-nt volumes obtained from FS2, labelled FS2-A and  
428 FS2-B and corresponding to the Rol of the same name (see Fig. 4e and Fig. S5 of  
429 Supplementary Materials), are shown in Figs. 6 and 7 respectively. The large volume  
430 size of FS2-A (c.  $8 \times 10^4 \mu\text{m}^3$ , voxel size c. 67 nm) enabled the organisation of large  
431 submicrometre structures to be revealed in 3D, while the higher resolution of FS2-B  
432 (c.  $5 \times 10^3 \mu\text{m}^3$ , voxel size c. 15 nm) allowed for the detailed characterisation of  
433 constituents and particle-particle associations.

434 FIB-nt datasets were segmented following Wheatland et al. (2017). The  
435 primary floc constituents (resin filled pore-space, floc matrix, non-clay minerals, and  
436 large bioorganic and organic structures) and floc matrix constituents (clays minerals,  
437 microbial cells and organo-mineral debris) identified in 2D SEM and STEM were also  
438 identified in FIB-nt (Table 1 and Fig. 6 and 7). Additionally, the enhanced spatial  
439 resolution of FS2-B enabled the segmentation of closely packed particles c.  $<2 \mu\text{m}$   
440 (e.g., clays within the floc matrix), enabling their reconstruction in 3D (Fig. 7e). This  
441 is demonstrated in Fig. 7d in which individual clays can be discriminated in 2D slices  
442 from the FIB-nt dataset. Several of the particle-particle associations identified within  
443 SEM and STEM data (see Section 3.1.3 and Fig. S6 of Supplementary Materials)

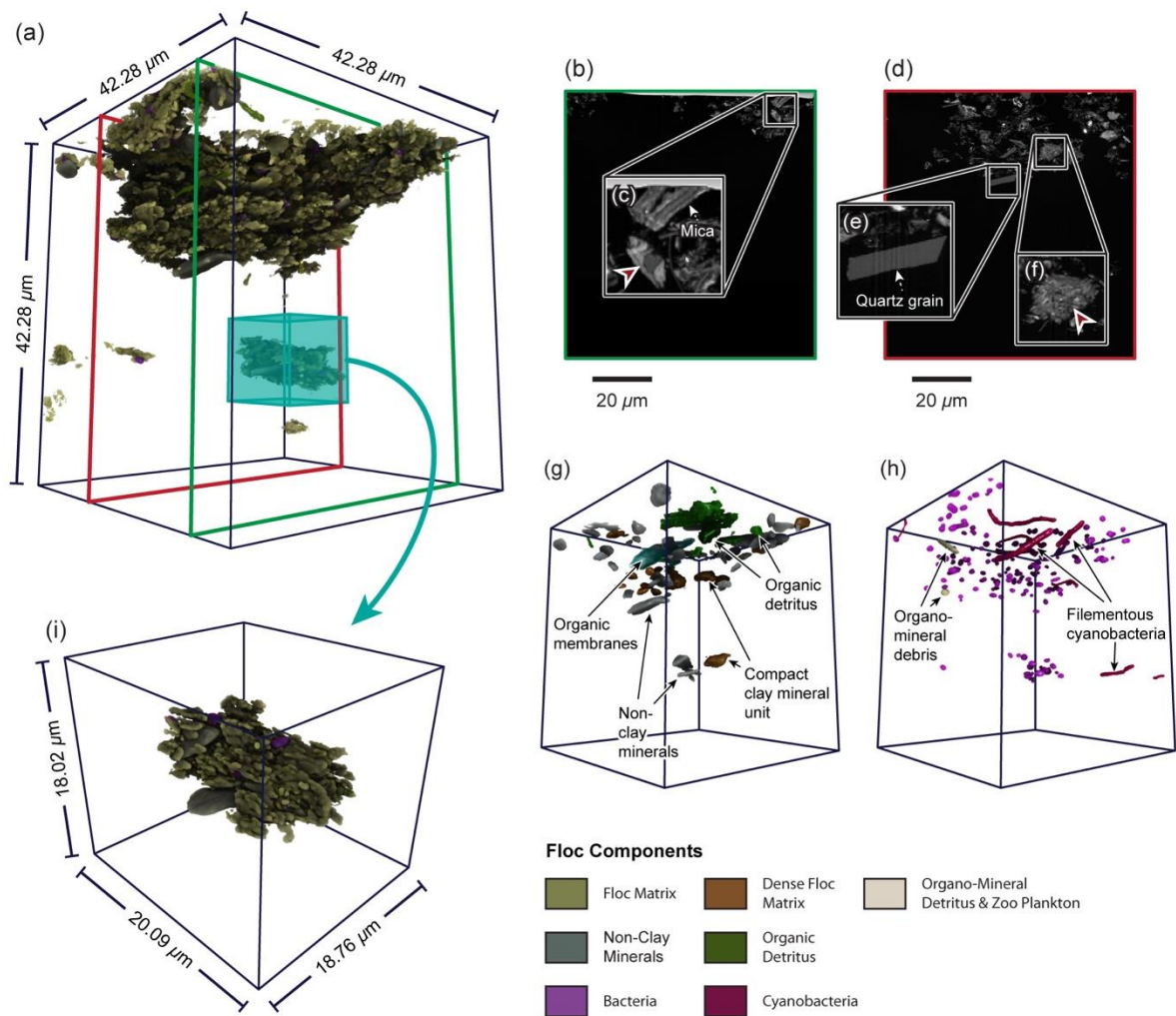


**Figure 6.** 3D reconstructions of the FIB-nt volume Rol FS2-A: (a) 3D rendering of the segmented components identified within FS2-A; (b - c) Selected BSE images from the FIB-nt dataset illustrating the differences in grey-scale and morphology that enable feature segmentation, note the red arrow shown in (c) highlights a region of high particle occupation. The locations from which the 2D BSE images shown in (b) and (c) were taken from within the FIB-nt dataset are indicated by coloured lines shown in (a); (g) Same as (a) but with selected materials rendered transparent to reveal the non-clay minerals, organic membranes and amorphous organic detritus; (h) Same as (a) but with certain materials rendered transparent to reveal the individual bacteria, cyanobacteria and organomineral debris (diatom frustules); (e) Sub-volume taken for FS2-A showing an isolated microfloc (location indicated in (a)).

444 were also identified in FS2-B. Visualised in 3D these structures are revealed to be  
 445 discrete units, separable from surrounding floc matrix by nanopores (Fig. 7e and f).

446 Fig. 7e shows a particle association consisting of clay minerals aligned face-to-face,  
447 while Fig. 7f shows clay particles aligned around a central bacterium. Examination of  
448 the floc matrix reveals micrometre pore channels delineating the boundaries of  
449 discrete structural units 10's  $\mu\text{m}$  in diameter (e.g., Fig. 6i). These structures usually  
450 consist of several particle-particle associations and larger primary particles (e.g., silt  
451 grains, organic detritus), loosely arranged in an open, card-house structure, linked  
452 together by filamentous cyanobacteria.

453 Quantification reveals the occupied volume of FS2-A largely consists of  
454 inorganic material, with clays accounting for c. 98% of occupied space and non-clay  
455 minerals c. 0.5% (Table 3). In contrast, a larger proportion of FS2-B is occupied by  
456 organics, which accounted for c. 34% of the occupied volume compared to inorganic  
457 material, c. 66%. Within both FIB-nt datasets micrometre pore channels can be  
458 identified together with elongated nanopores throughout the floc matrix (Fig. 6 and  
459 7). Combined, these give a total porosity of c. 95 % and c. 52 % for FS2-A and FS2-  
460 B respectively. The resolution and 3D nature of the datasets enabled the  
461 classification of microbial cells based on morphotype (Dazzo & Niccum 2015) and  
462 five categories were recognised: i) cocci, ii) regular straight rods (e.g., bacilli), iii)  
463 curved/U-rods (e.g., vibrio), iv) spirals (e.g., spirilla) and v) unbranched filaments  
464 (e.g., cyanobacteria) (Fig. 6d - h). Cocci were characterised as near spherical  
465 (length/width, <2:1) with diameters <1.5  $\mu\text{m}$  (Fig. 6h), frequently forming groups of  
466 several cells. In comparison, bacilli exhibited a straight, rod-like morphology  
467 (length/width, <16:1) and were larger (diameter, c. 2  $\mu\text{m}$ ). Cells with a crescent  
468 curvature (comma-shaped) were identified as vibrio, and had similar dimensions to  
469 bacilli (Fig. 5d – h). Although observed less frequently, spirilla were classified as  
470 elongated cells displaying a distinctive repeated waveform (e.g., corkscrew-shaped).

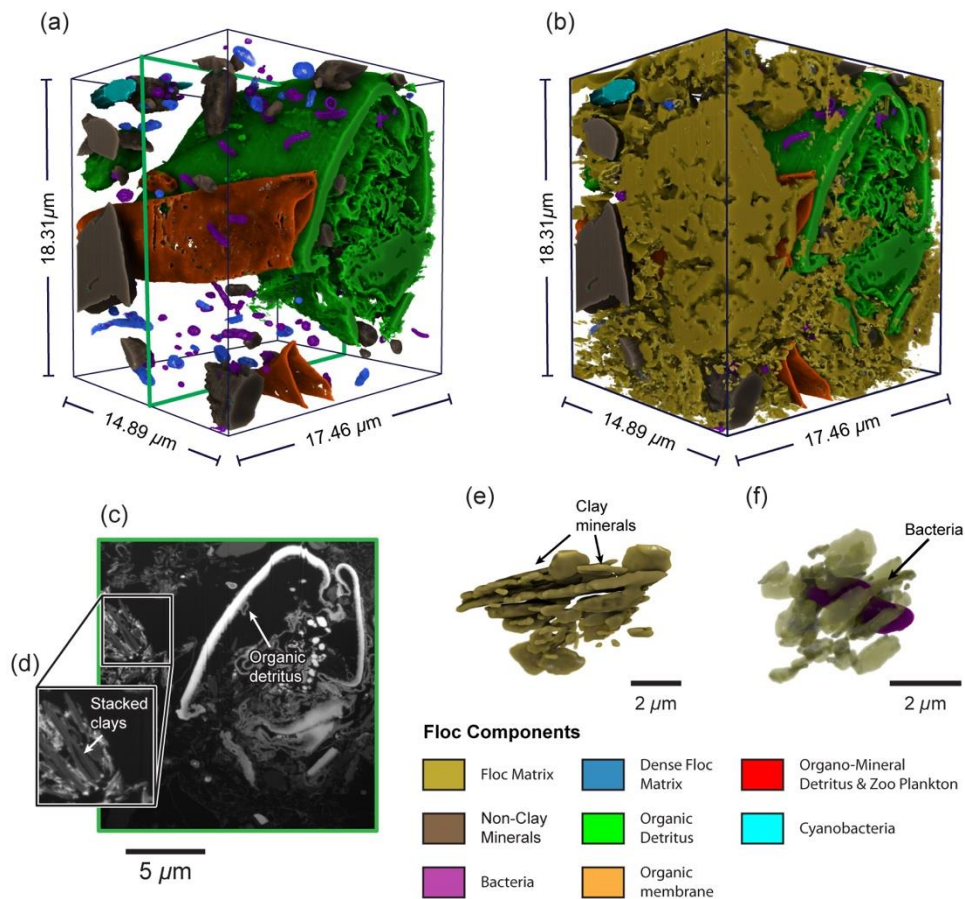


**Figure 7.** 3D reconstructions of the FIB-nt volume Rol FS2-B: (a) 3D rendering of the segmented components identified within FS2-B; (c) Selected BSE image from the FIB-nt dataset illustrating the differences in grey-scale and morphology that enable feature segmentation. The locations from which the 2D BSE image shown in (c) was taken from within the FIB-nt dataset are indicated by the green coloured line shown in (a); (d) Sub-set from (c) showing clay minerals aligned face-to-face and/or edge-to-face; (e) 3D reconstruction of (d); (f) Clay particle arranged radially around a bacterial cell (bacteria false-coloured purple).

471 Filamentous (cyanobacteria) bacteria could be easily distinguished from other cell  
 472 types based on elongated shape (length/width, >16:1), and were present in a  
 473 number of forms, ranging from cells 1 – 2 μm in diameter to larger varieties  
 474 (diameters, c. >3 μm) (Fig. 5h). The quantities of cell morphotypes and their  
 475 intracellular integrity (e.g., intact, damaged or empty, Heissenberger et al. 1996) are  
 476 shown in Table 4.

FIB-nt Sample	Total Volume ( $\mu\text{m}^3$ )	Floc Constituents (Vol. %)						
		Porosity		Floc Matrix			Other	
		Micro-Porosity	Nano-Porosity	Clay Minerals	Bacteria	Organo-Mineral Debris	Organic Detritus	Non-Clay Minerals
FS2-A	c. $8 \times 10^4$	91.4	3.80	4.08	0.07	0.01	0.23	0.41
FS2-B	c. $5 \times 10^3$	-	51.79	31.96	0.45	0.07	17.16	2.15

477 **Table 3.** Volume fractions for the segmented components of FIB-nt datasets FS2-A  
478 and FS2-B.

479

FIB-nt Sample	Total Bacteria (Count)	Intracellular Integrity (% of Total Count)		Cell Morphotype (% of Total Count)				
		Intact Cells	Damaged and Empty Cells	Cocci	Regular Straight Rod	Curved/U-Rod	Unbranched Filament	Spiral
FS2-A	239	73.2	26.8	48.95	28.03	17.57	5.44	0
FS2-B	118	76.4	23.6	41.53	32.20	19.49	4.24	2.54

480 **Table 4.** Total count of bacteria, numbers of intact, damaged and empty cells and  
481 proportions of different cell morphotypes identified in FIB-nt datasets FS2-A and  
482 FS2-B.

483

484

### 485 **3.2. Validation of Floc Stabilisation Method**

486 Interpretation and quantification of 3D flocs relies on an assumption that the  
487 characteristics observed are representative of true floc structure and not artefacts of  
488 sampling, storage and preparation (Liss et al. 1996; Wheatland et al. 2017). The  
489 correlative workflow demonstrated above permits the validation of floc integrity in this  
490 context by enabling observation of 3D floc structure across multiple spatial scales.

491 Fluid exchanges and sample dehydration are essential for the chemical  
492 stabilisation process, but can result in the distortion and/or rupture of delicate cellular  
493 structures. While a number of cells identified in the 3D FIB-nt datasets were  
494 classified as either damaged or empty (Heissenberger et al. 1996) (Table 4),  
495 Wheatland et al. (2017) notes that the presence of damaged cells in itself is not  
496 indicative of inadequate stabilisation, since active microbial communities contain  
497 cells of all states of life including decay. More diagnostic of the state of preservation  
498 is the presence of intact cells, as rupture due to poor stabilisation would be expected  
499 to be systemic. Within the FIB-nt datasets intact cells accounted for c. >50% of the  
500 total number of cells, a higher percentage compared than that of the total number of  
501 metabolically active bacteria usually found in natural microbial communities (c.  
502 <30%, Ward & Johnson 1996). The loss of soluble EPS (i.e. EPS unassociated with  
503 bacterial cells) from the floc matrix during fluid exchanges can result in severe  
504 perturbation (Leppard et al. 1996). Previous studies have estimated up to 50–80% of  
505 EPS can be removed in certain instances from the floc matrix following stabilisation  
506 (Leppard et al. 1996), with the primary effect on the floc being the rearrangement of  
507 primary particles and compression of floc structures (recorded as shrinkage) (Liss et  
508 al. 1996). STEM imagery obtained from the floc samples reveals the presence of  
509 exopolymeric material, observed as dense networks in the nanometre pore space  
510 between primary particles (e.g., clays and bacteria) and distributed throughout the  
511 floc matrix (Fig. S6 of Supplementary Materials). This suggest that the little  
512 extraction of the EPS network within the floc matrix has taken place. The use of  
513 plankton chambers for floc capture and agarose gel for floc immobilisation help  
514 minimise the destructive forces associated with traditional sampling methods (e.g.,  
515 floc breakage via pipetting) (Droppo et al. 1996). However, morphological changes

516 can result if flocs interact once settled, e.g., false aggregation of flocs and/or  
517 pseudoplastic contortion of delicate structures with overburden pressure.  
518 Examination of flocs of immobilised in agarose prior to resin embedding provides a  
519 means of assessing the degree of interaction between neighbouring flocs. 2D cross-  
520 sectional images taken from the  $\mu$ CT of test sample FS0 (Fig. S1 of Supplementary  
521 Materials) reveal minimal overlap between neighbouring floc particles, suggesting  
522 morphological changes to be minimal. This is supported by the 3D visualisation of  
523 individual flocs (FS1, FS2 and FS3, Fig. 3 and Movie 1) that indicate delicate  
524 structures (e.g., filamentous protuberances, Fig. 3b and c) remained intact following  
525 settling and during the addition of agarose and sub-sampling for stabilisation.

526

### 527 **3.3. Merits of the Correlative Workflow**

528 This imaging workflow enables for the first time floc composition and 3D structure to  
529 be investigated at all relevant spatial scales, from primary particles to entire flocs  
530 several mm in size. This represents a significant advance in our ability to  
531 characterise flocs, filling the resolution gap between traditional imaging techniques  
532 (e.g., TEM, CLSM and COM) (Fig. 8).

533 The success of the workflow critically depends upon the quality (i.e. resolution,  
534 signal-to-noise ratio) and degree of similarity (i.e. resolution and mechanisms for  
535 contrast generation) between the different datasets (Caplan et al. 2011; Handschuh  
536 et al. 2013). Image quality is of particular importance, since it determines the  
537 accuracy with which features can be identified, segmented and quantified. Within  
538  $\mu$ CT and EM datasets the boundaries between objects are not always well defined,  
539 but can consist of a transitional zone 3 – 5 pixels wide (Holzer et al. 2014;  
540 Wheatland et a. 2017). Depending on the pixel/voxel resolution of the dataset the

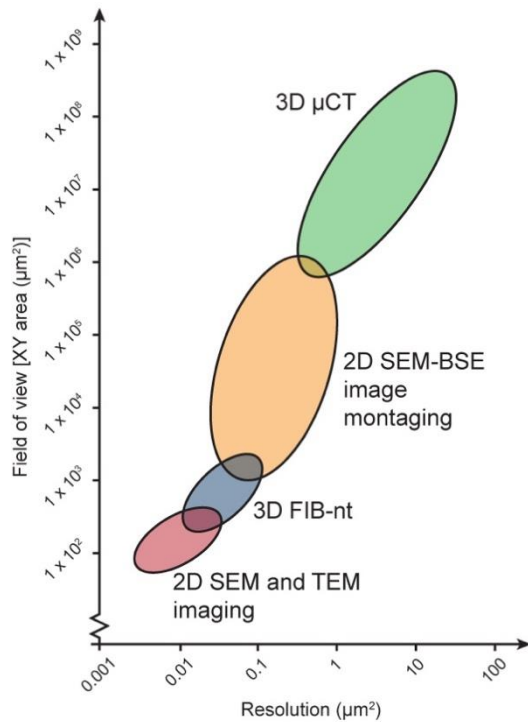


**Figure 8.** Length-scales over which the 2D and 3D imaging techniques employed within correlative workflow operate, with corresponding typical cross-section (XY) and resolution achievable by each technique. Note that the imaging methods used overlap, enabling truly correlative examination of floc structure from the nm to mm-scale.

541 maximum error is usually considered to be half the width of this zone. Further  
 542 discussion regarding the process of segmentation and potential errors is outlined in  
 543 Wheatland et al. (2017).

544 Fig. 3 shows the correlative 2D and 3D datasets collected from FS1 registered  
 545 in a single 3D scene. To locate the floc cross-section, aluminium wire was used as a  
 546 fiducial marker to register the  $\mu$ CT data collected after ultramicrotomy to the original  
 547  $\mu$ CT dataset of the intact flocs (see Section 2.3 and Fig. 1d). Segmentation of the

548 aluminium wire would ideally result in it being represented by similar number voxels

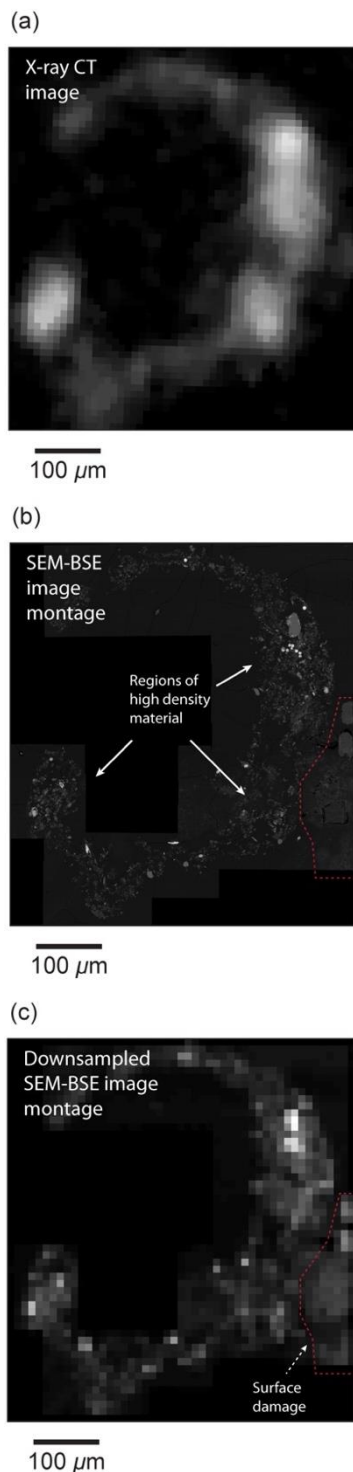


**Figure 9.** Comparison of  $\mu\text{CT}$  with SEM-BSE. Down-sampling the pixel size of the SEM-BSE image montage (c) to match that of the  $\mu\text{CT}$  data (c.  $10\ \mu\text{m}$ ), enabled comparison between the SEM-BSE image montage (b) and corresponding  $\mu\text{CT}$  slice (a). This provides a means of validating the potential floc structures responsible for different greyscale values within the  $\mu\text{CT}$  dataset. Regions of the floc observed to contain high concentrations highlighted in (b) of particles in the BSE-SEM image montages were shown to exhibit high grey-scale values in the  $\mu\text{CT}$  dataset (a).

549 in the corresponding  $\mu$ CT datasets. Within both pairs of  $\mu$ CT data the wire was easily  
550 segmented from other material phases based on its high greyscales (e.g., see  
551 Section 3.1.1 and Fig. 2). However, discrepancies in the size of the segmented  
552 aluminium wire were observed – 1.6% for FS1 and 3.8% for FS2 – which likely  
553 resulted from scan artefacts, i.e. secondary edge effects due to partial volume effect.  
554 Assuming an even distribution of the extraneous voxels around the surface area of  
555 the aluminium fiducial marker, the minimum offset between co-registered datasets  
556 can be estimated to be of the order of less than a voxel (c. 3 – 6  $\mu$ m) over a total 3D  
557 size of  $10 \times 10^8 \mu$ m. With evidence of only minor peripheral misalignment of the  
558 registered datasets, the co-registration of the 3D  $\mu$ CT scans has been successful.

559 2D SEM-BSE image montages of the floc cross-sections were critical for the  
560 co-registration of 2D and 3D nm and  $\mu$ m datasets with the sub mm-scale 3D  $\mu$ CT  
561 data. The trapezoidal shape of the cross-sections (Fig. 3b and Fig. S3 of  
562 Supplementary Materials) can be defined in the  $\mu$ CT datasets, enabling the SEM-  
563 BSE image montages to be tied to the surface within an accuracy of 3 – 6 voxels (c.  
564 30 – 60  $\mu$ m). However, further confidence in the accuracy of the co-registration can  
565 be obtained by comparing the actual shape of the floc boundary depicted in the two  
566 datasets. Reducing the pixel resolution of the SEM-BSE image montages (i.e. down-  
567 sampling) to match that of the  $\mu$ CT datasets (c. 10  $\mu$ m) enables a direct comparison  
568 between the SEM-BSE image montages and  $\mu$ CT data (Fig. 9), which indicates the  
569 error to be less than a voxel (c. <10  $\mu$ m). In addition, the features responsible for the  
570 variations observed in  $\mu$ CT greyscale values, that reflect the variability of floc  
571 constituents and structure at the sub-voxel scale (representing the impact of partial  
572 volume effects, cf. Ketcham & Carlson 2001), can be confirmed by comparing the  
573 down-sampled SEM-BSE image montage with the corresponding  $\mu$ CT slice. Fig. 9

574 demonstrates that regions of the SEM-BSE image montage identified as containing  
575 high concentrations of particles correspond to regions of high attenuation (high  
576 greyscales) within  $\mu$ CT. The similar imaging conditions selected for both SEM-BSE  
577 imaging (montaging and imaging of Rol) and FIB-nt allowed reference landmarks  
578 within the corresponding datasets to be recognised with a high degree of certainty  
579 (20 – 60 nm). As the contrast mechanisms in both SEM-BSE and dark-field STEM  
580 are similar (related to atomic number) fiducial markers internal to the floc (e.g., silt  
581 grains and bacteria etc.) could be easily identified. However, inspection of the  
582 overlaid STEM images following co-registration with SEM imagery revealed  
583 discrepancies in the positions of these markers. These displacements are likely the  
584 result of ultramicrotomy, as shear stresses imposed during sectioning are known to  
585 cause thin-section compression (Peachey 1958).

586

### 587 **3.4 Applications of 3D Floc Structural and Compositional Data**

588 Providing such detailed 3D analysis of flocs is not readily applicable for field scale  
589 quantification of suspended sediment aggregates. However, this technique has the  
590 potential, through targeted experimental or field campaigns, to provide new  
591 understanding of floc composition and controls on floc characteristics and structures.  
592 For example, these datasets quantify 3D floc characteristics (e.g., size, shape and  
593 porosity) that are critical input parameters to cohesive sediment transport models.

594 Additionally, the datasets demonstrate the complex structural associations and  
595 particle-particle interactions found at different spatial scales and levels of  
596 aggregation. These are frequently hypothesised in the literature or inferred from 2D  
597 observations of gross floc characteristics (e.g., Maggi et al. 2007; Lee et al. 2011).  
598 These particle-particle associations reflect the materials present in suspension

599 during floc development and their interactions. Here, the particle associations  
600 including clays oriented face-to-face and/or edge-to-face likely occur due to a  
601 combination of electrochemical interactions (i.e. cohesion), and the additional  
602 binding forces provided by organic materials resulting in bioflocculation, i.e. adhesion  
603 (Liss et al. 1996; Righetti & Lucarelli 2010). Yet the short distances ( $10^1$  to  $10^3$  nm)  
604 over which these forces (cohesion and adhesion) operate mean that these structures  
605 are clearly scale-dependent. Larger structural units consisting of several particle-  
606 particle associations and individual primary particles (e.g., silt grains, amorphous  
607 organic detritus etc.) were found throughout the floc samples. Therefore, this new  
608 method could provide data to challenge or validate simplified descriptors of floc  
609 structure e.g., self-similarity or fractal geometry (e.g., Khelifa & Hill 2006).

610 Our data also demonstrate and quantify the microbial associations with  
611 flocculated material. For example, demonstrating the importance of cell morphotype  
612 on floc shape and strength. Here, filamentous cyanobacteria cross-link smaller  
613 structural units (observed in 2D SEM and 3D FIB-nt) promoting interactions between  
614 these structural units and providing structural connectivity and flexibility (e.g.,  
615 Nguyen et al. 2007). Their strongly elongate shape and propensity to align has a  
616 strong influence on floc development, promoting the growth of non-spherical flocs.  
617 Additionally, filaments extending from the periphery of the flocs provide anchor  
618 points to facilitate floc growth through interactions with other flocs (Burger et al  
619 2017).

620

#### 621 **4. Conclusion**

622 The development of a novel correlative workflow provides datasets demonstrating  
623 the complex composition and multiscale 3D structure of aquatic sediment flocs. This

624 work provides the most detailed floc structural analysis to date and provides the  
625 following specific advantages:

- 626 • 2D and 3D imaging techniques can be applied in a systematic manner to  
627 successfully obtain a complete set of overlapping, co-registered datasets from  
628 a single floc sample. The resultant datasets enable the identification and  
629 quantification of floc composition and structures across multiple length-scales.  
630 This approach improves on traditional 2D correlative microscopy by providing  
631 truly correlative datasets that are quantifiable.
- 632 • The orientation of multi-scale and multi-modal datasets in 3D space presents  
633 a significant challenge, but can be successfully overcome using fiducial  
634 markers. This is reliant on selecting imaging techniques that share similar  
635 contrast mechanisms, to ensure that landmark features can be detected at  
636 different spatial scales.
- 637 • Particle-particle and structural associations can be directly related across  
638 length-scales. Structures that are scale-dependent can be recognised,  
639 providing further evidence for interactions that have previously been  
640 hypothesised. The imaging workflow therefore provides a means of obtaining  
641 quantitative measures of floc composition and structure and a better  
642 understanding of the mechanisms promoting floc growth.
- 643 • The correlative workflow is adaptable, and the potential exists for further  
644 research to design targeted experiments to explore relationships between floc  
645 structure and behaviour, controls on floc stability and structure, and floc  
646 microbial communities.

647

648 **Acknowledgements**

649 J.A.T.W. would like to thank the Engineering and Physical Sciences Research Council  
650 for the award of a scholarship and the Queen Mary University of London Postgraduate  
651 Research Fund. K.L.S, A.J.B and S.J.C acknowledge the Natural Environmental  
652 Research Council (NE/N011678/1) for funding. Jemima Burden (MRC Laboratory for  
653 Molecular Cell Biology, University College London) is thanked for her help with sample  
654 preparation.

655

## 656 **References**

- 657 Agrawal, Y.C., Pottsmith, H.C. 2000. Instruments for particle size and settling  
658 velocity observations in sediment transport. *Mar. Geol.* 168 (1–4), 89-114.
- 659 Arganda-Carreras, I., Kaynig, V., Rueden, C., Eliceiri, K.W., Schindelin, J.,  
660 Cardona, A., Seung, H.S. 2017. Trainable Weka Segmentation: a machine  
661 learning tool for microscopy pixel classification. *Bioinformatics* 33 (15), 2424-  
662 2426.
- 663 Azam, F., Long, R.A. 2001. Sea snow microcosms. *Nature* 414, 495-498.
- 664 Burd, A.B. Jackson, G.A. 2009. Particle aggregation. *Annu. Rev. Mar. Sci.* 1, 65-90.
- 665 Burger, W., Krysiak-Baltyn, K., Scales, P.J., Martin, G.J.O., Stickland, A.D., Gras,  
666 S.L. 2017. The influence of protruding filamentous bacteria on floc stability and  
667 solid-liquid separation in the activated sludge process. *Water Res.* 123, 578-  
668 585.
- 669 Burnett, T.L., McDonald, S.A., Gholinia, A., Geurts, R., Janus, M., Slater, T., Haigh,  
670 S.J., Ornek, C., Almuaili, F., Engelberg, D.L., Thompson, G.E., Withers, P.J.  
671 2014. Correlative tomography. *Sci. Rep.* 4, 1-6.

672 Bushby, A.J., Png, K.M.Y., Young, R.D., Pinali, C., Knupp C., Quantock A.J. 2011.  
673 imaging three-dimensional tissue architectures by focused ion beam scanning  
674 electron microscopy. *Nat. Protoc.* 6 (6), 845-858.

675 Bushby, A.J., Mariggi, G., Armer, H.E.J., Collinson, L.M. 2012. Correlative Light and  
676 Volume EM: Using Focused Ion Beam Scanning Electron Microscopy to image  
677 transient events in model organisms. *Methods Cell Biol.* 111, 357-382.

678 Caplan, J., Niethammer, M., Taylor, R.M., Czymmek, K.J. 2011. The power of  
679 correlative microscopy: multi-modal, multi-scale, multi-dimensional. *Curr. Opin.*  
680 *Struct. Biol.* 21 (5), 686-693.

681 Cnudde, V., Boone, M.N. 2013. High-resolution X-ray computed tomography in  
682 geosciences: A review of the current technology and applications. *Earth-Sci.*  
683 *Rev.* 23, 1-17.

684 Dazzo F.B., Niccum, B.C. 2015. Use of CMEIAS image analysis software to  
685 accurately compute attributes of cell size, morphology, spatial aggregation and  
686 color segmentation that signify in situ ecophysiological adaptations in microbial  
687 biofilm communities. *Computation* 3, 72-98.

688 Droppo, I.G. 2001. Rethinking what constitutes suspended sediments. *Hydrol.*  
689 *Process.* 15 (9), 1551-1564.

690 Droppo, I.G. 2003. A new definition of suspended sediment: implications for the  
691 measurement and prediction of sediment transport. In: Bogen, J., Fergus, T.,  
692 Walling, D. (Eds.), *Erosion and Sediment Transport Measurement in Rivers:*  
693 *Technological and Methodological Advances.* IAHS Publication No. 249,  
694 International Association of Hydrological Sciences, Wallingford, pp. 238.

695 Droppo, I.G., Flannigan, D.T., Leppard, G.G., Jaskot, C., Liss, S.N. 1996. Floc  
696 stabilization for multiple microscopic techniques. *Appl. Environ. Microbiol.* 62,  
697 3508-3515.

698 Handschuh, S., Baeumler, N., Schwaha, T., Ruthensteiner, B. 2013. A correlative  
699 approach for combining microCT, light and transmission electron microscopy in  
700 a single 3D scenario. *Front. Zool.* 10, 1-16.

701 Heissenberger A., Leppard, G.G., Herndl, G.J. 1996. Relationship between the  
702 intracellular integrity and the morphology of the capsular envelope in attached  
703 and free-living marine bacteria. *Appl. Environ. Microbiol.* 62 (12), 4521-4528.

704 Holzer, L., Indutnyi, F., Gasser, P.H., Münch, B., Wegmann, M. 2004. Three-  
705 dimensional analysis of porous BaTiO<sub>3</sub> ceramics using FIB nanotomography.  
706 *J. Microsc.* 216 (1), 84-95.

707 Jarvis, P., Jefferson, B., Gregory, J., Parsons, S.A. 2005. A review of floc strength  
708 and breakage. *Water Res.* 39 (14), 3121-3137.

709 Ketcham, R.A., Carlson, W.D. 2001. Acquisition, optimization and interpretation of X-  
710 ray computed tomographic imagery: applications to the geosciences. *Comput.*  
711 *Geosci.* 27, 381-400.

712 Khelifa, A. Hill, P.S. 2006. Models for effective density and settling velocity of flocs.  
713 *J. Hydraul. Res.* 44, 390-401.

714 Lee, B.J., Toorman, E., Molz, F., Wang, J., 2011. A two-class population balance  
715 equation yielding bimodal flocculation of marine or estuarine sediments. *Water*  
716 *Res.* 45, 2131–2145.

717 Leppard, G.G. 1992. Size, morphology and composition of particulates in aquatic  
718 ecosystems: solving speciation problems by correlative electron microscopy.  
719 *The Analyst* 117 (3), 595-603.

720 Leppard, G.G., Heissenberger, A., Herndl, G.J. 1996. Ultrastructure of marine snow.  
721 I. Transmission electron microscopy methodology. *Mar. Ecol. Prog. Ser.* 135,  
722 289-298.

723 Liss, S.N. 2002. Microbial Flocs Suspended Biofilms. In: Bitton, G. (Ed.),  
724 Encyclopaedia of Environmental Microbiology (Vol. 4). John Wiley and Sons,  
725 New York, NY, pp. 2000-2012.

726 Liss, S.N., Droppo, I.G., Flannigan, D.T., Leppard, G.G. 1996. Floc architecture in  
727 wastewater and natural riverine systems. *Environ. Sci. Technol.* 30 (2), 680-  
728 686.

729 Maggi, F., Mietta, F., Winterwerp, J.C. 2007. Effect of variable fractal dimension on  
730 the floc size distribution of suspended cohesive sediment. *J. Hydrol.* 343 (1-2),  
731 43-55.

732 Manning, A.J., Dyer, K.R. 2002. The use of optics for the in situ determination of  
733 flocculated mud characteristics. *J. Opt. A-Pure Appl. Op.* 4, 71-81.

734 Nguyen, T.H., Tang, F.H., Maggi, F. 2017. Optical Measurement of cell Colonization  
735 Patterns on Individual Suspended Sediment aggregates. *J. Geophys. Res.*  
736 *Earth Surf.* 122 (10), 1794-1807.

737 Nguyen, T.P., Hankins, N.P., Hilal, N. 2007. A comparative study of the flocculation  
738 behaviour and final properties of synthetic and activated sludge in wastewater  
739 treatment. *Desalination* 204 (1), 277-295.

740 Ollion, J., Cochenec, J., Loll, F., Escudé, C., Boudier, T. 2013. TANGO: a generic  
741 tool for high-throughput 3D image analysis for studying nuclear organization.  
742 *Bioinformatics* 29, 1840-1841.

743 O'Shea, F.T., Cundy, A.B, Spencer, K.L. The contaminant legacy from historic  
744 coastal landfills and their potential as source of diffuse pollution. *Mar. Pollut.*  
745 *Bull.* 128, 446-455.

746 Peachey, L.D. 1958. Thin Sections: I. A study of section thickness and physical  
747 distortion produced during microtomy. *J. Biophys. Biochem. Cytol.* 4 (3), 233-  
748 242.

749 Preibisch, S., Saalfeld, S., Tomancak, P. 2009. Globally optimal stitching of tiled 3D  
750 microscopic image acquisitions. *Bioinformatics* 25 (11), 1463-1465.

751 Righetti, M., Lucarelli, C. 2010. Resuspension phenomena of benthic sediments: the  
752 role of cohesion and biological adhesion. *River Res. Appl.* 26, 404-413.

753 Rummel, C.D., Jahnke, A., Gorokhova, E., Kühnel, D., Schmitt-Jansen, M. 2017.  
754 Impacts of Biofilm Formation on the Fate and Potential Effects of Microplastic in  
755 the Aquatic Environment. *Environ. Sci. Technol.* 4 (7), 258 - 267

756 Rusconi, R., Guasto, J. S., Stocker, R. 2014. Bacterial Transport Suppressed by  
757 Fluid Shear. *Nat. Phys.* 10 (3), 212–217.

758 Schindelin, J., Arganda-Carreras, I., Frise, E., Kaynig, V., Longair, M., Pietzsch, T.,  
759 Preibisch, S., Rueden, C., Saalfeld, S., Schmid, B., Tinevez, J-Y., White, D. J.,  
760 Hartenstein, V., Eliceiri, K., Tomancak, P., Cardona, A. 2012. Fiji: an open-  
761 source platform for biological-image analysis. *Nature Methods* 9 (7), 676-682.

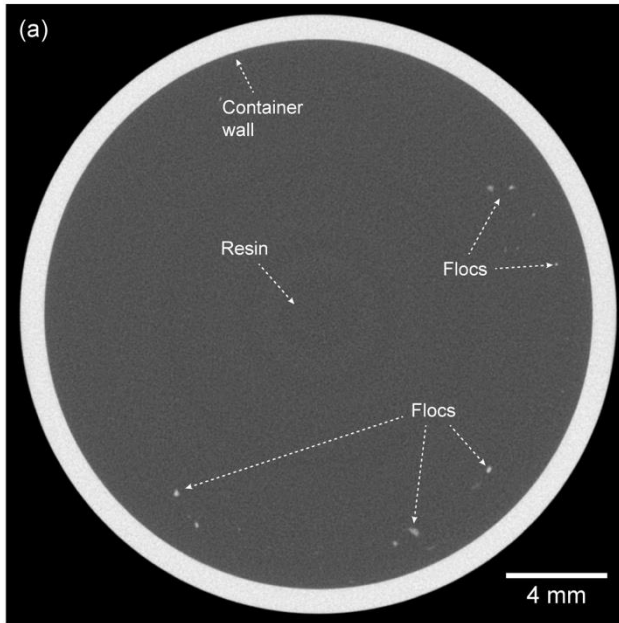
762 Sharma, S., Lin, C-L., Miller, J.D. 2017. Multi-scale features including water content  
763 of polymer induced kaolinite floc structures. *Miner. Eng.* 101, 20-29.

764 Soulsby, R.L., Manning, A.J., Spearman, J., Whitehouse, R.J.S. 2013. Settling  
765 velocity and mass settling flux of flocculated estuarine sediments. *Mar. Geol.*  
766 339, 1-12.

- 767 Tolhurst, T.J., Gust, G., Paterson, D.M. 2002. The influence on an extra-cellular  
768 polymeric substance (EPS) on cohesive sediment stability. In: Winterwerp,  
769 J.C., Kranenburg, C. (Eds.), *Fine Sediment Dynamics in the Marine  
770 Environment - Proceedings in Marine Science 5*. Elsevier Science, Amsterdam,  
771 pp. 409-425
- 772 Ward, A.K., Johnson, M.D. 1996. Heterotrophic microorganisms. In: Hauer, F.R.,  
773 Lamberti, G.A. (Eds.), *Methods in Stream Ecology*. Academic Press, San  
774 Diego, CA, pp. 233-268.
- 775 Wheatland, J.A.T., Bushby, A.J., Spencer, K.L. 2017. Quantifying the structure and  
776 composition of flocculated suspended particulate matter using focused ion  
777 beam nanotomography. *Environ. Sci. Technol.* 51 (16), 8917-8925.
- 778 Winterwerp, J.C. 1998. A simple model for turbulence induced flocculation of  
779 cohesive sediment. *J. Hyd. Eng. Res.* 36 (3), 309-326.
- 780 Zhang, N., Thompson, C.E.L., Townend, I.H., Rankin, K.E., Paterson, D.M., Manning  
781 A.J. 2018. Nondestructive 3D imaging and quantification of hydrated biofilm-  
782 sediment aggregates using X- ray microcomputed tomography. *Environ. Sci.*  
783 *Technol.* 52 (22), 13306-13313.

784

## 785 SUPPLEMENTARY FIGURES



786

787 **Supplementary Fig. S1.**  $\mu$ CT cross-sectional image from the scan of test sample

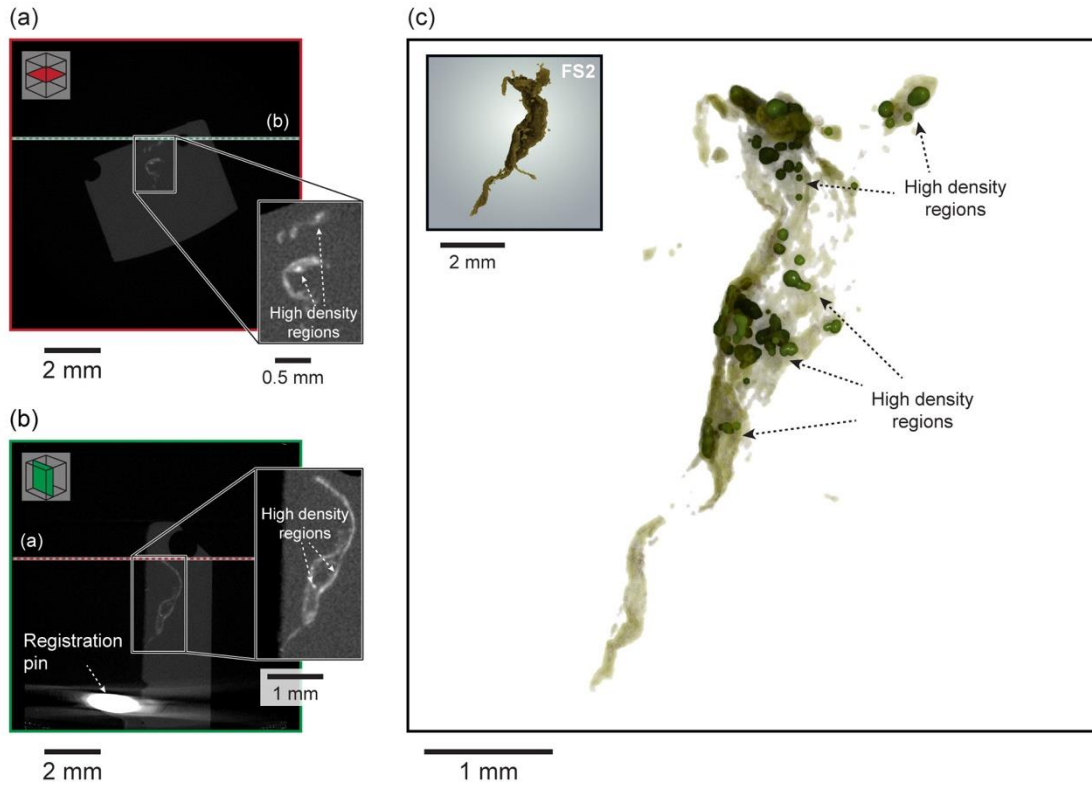
788 FS0, note the minimal overlap between neighbouring floc particles.

789

790

791

792



793

794

795

796

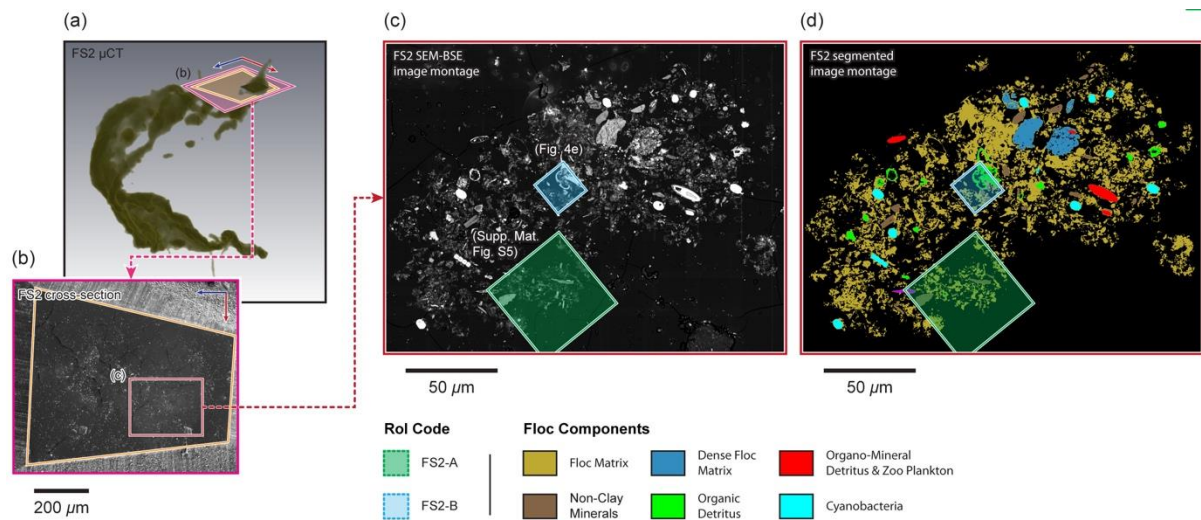
797

798

799

800

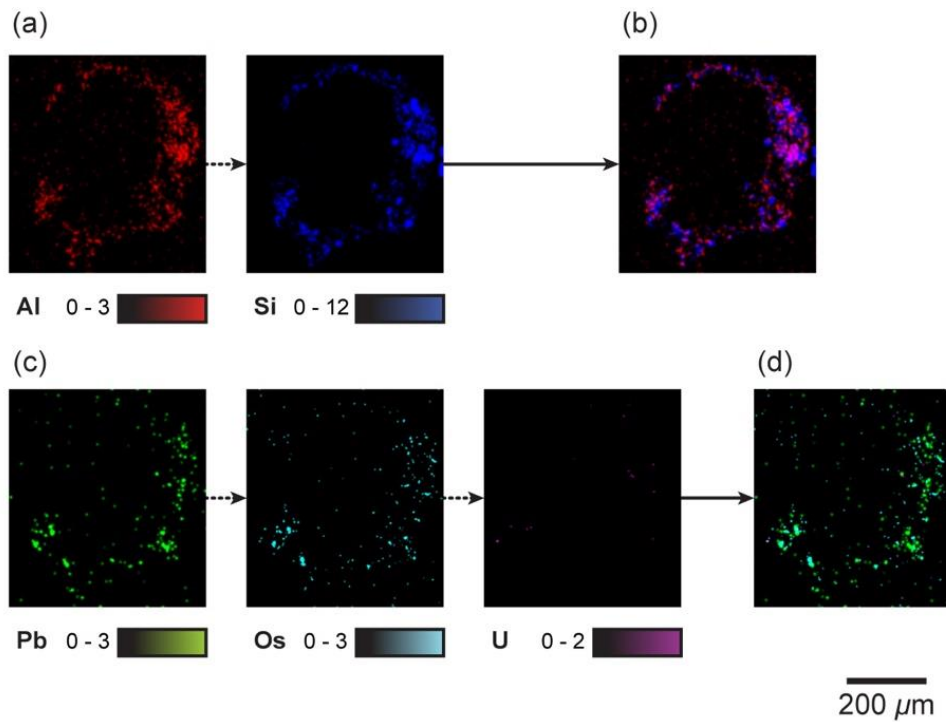
**Supplementary Fig. S2.** 3D visualisations of the floc samples FS2 (c). (a) and (b) are image slices taken in two orthogonal planes from the  $\mu$ CT date; note the regions of high and low X-ray attenuation within the floc shown in the magnified sub-sets; (c) shows a 3D visualisation of floc FS2 but with the regions of low X-ray attenuation rendered semi-transparent to reveal the regions of high attenuation.



801

802 **Supplementary Fig. S3.** Analysis of the cross-section located in floc FS2. The  
 803 location of the cross-section created within FS2 is shown in (a) and the region of the  
 804 cross-section containing the floc is shown in (b). The trapezoidal shape of the  
 805 sectioned block is highlighted in orange both in (a) and (b), while the boundary of the  
 806 SEM image of the cross-section shown in (b) is defined in 3D space in (a) in pink.  
 807 The SEM-BSE image montage (c) obtained from the cross-section through floc FS2  
 808 enabled the identification of floc constituents (d) and characterisation of floc structure  
 809 in 2D. The locations of Rols FS2-A and FS2-B selected for further analysis are  
 810 shown in (c) and (d).

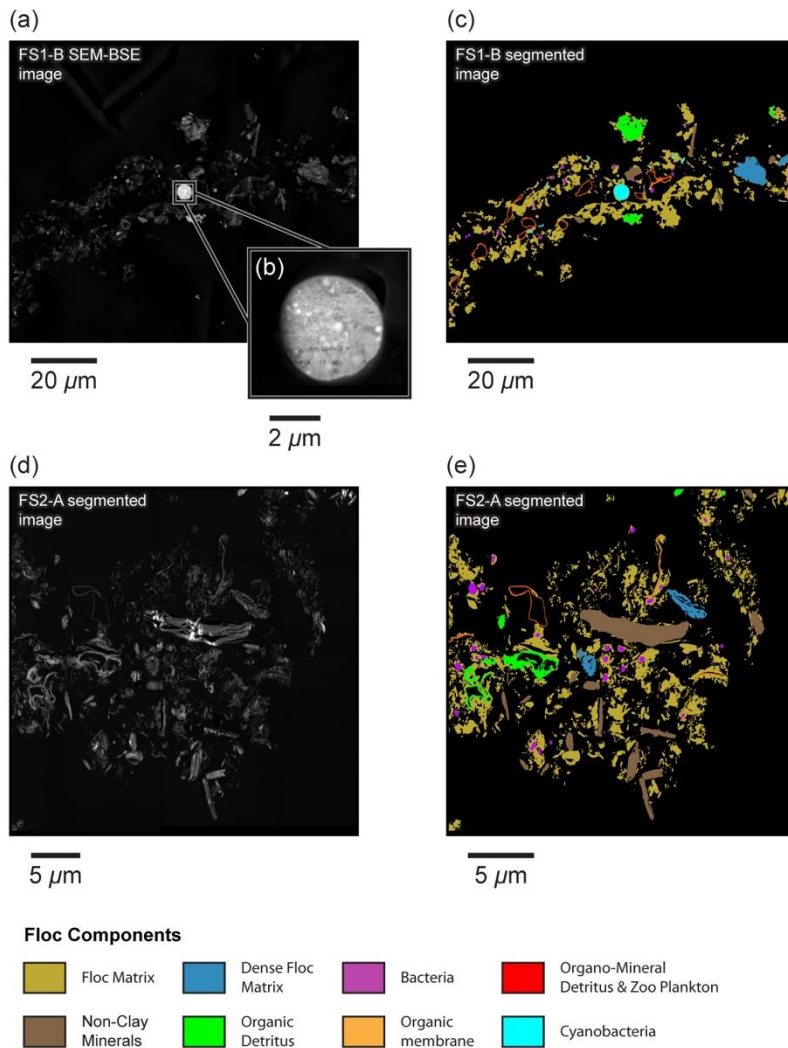
811



812

813 **Supplementary Fig. S4.** Individual SEM-EDS elemental maps collected from the  
 814 cross-section through floc FS2. (a) Inorganic signals for Al and Si; (b) combined  
 815 signal (phase map) for Al and Si; (c) Organic signals for Pb, Os, and U; (d) combined  
 816 signal for Pb, Os, and U.

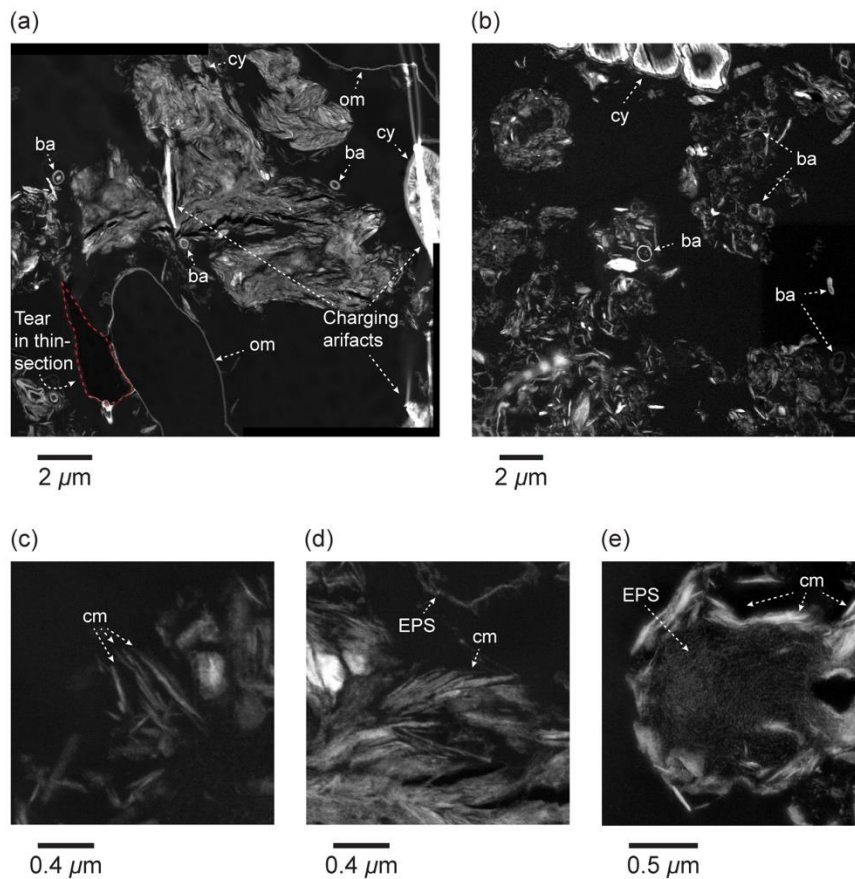
817



818

819 **Supplementary Fig. S5.** Characterisation of floc sub-micrometre composition and  
 820 structure in 2D within Rol FS1-B (a) and FS2-A (c). The locations of Rols FS1-B and  
 821 FS2-A are shown in Fig. 3c and Fig. S4 of Supplementary Materials respectively. (b)  
 822 shows a magnified subset from (a) that isolates a single cyanobacteria to  
 823 demonstrates how differential staining of subcellular structures has taken place.

824



825

826 **Supplementary Fig. S6.** Selected STEM images illustrating the materials and  
 827 structures commonly observed within flocs FS1 and FS2. Regions of high and low  
 828 (clay) particle occupation are shown in (a) and (b) respectively. Note that regions of  
 829 high occupation primarily consisted of clay minerals aligned face-to-face, whereas  
 830 low occupation regions contained a variety of materials (e.g., clays, decaying organic  
 831 detritus, bacteria etc.). The high grey-scale values (c. >70) exhibited by units of high  
 832 occupation likely relates to clays coated in organic material in the nanometre range  
 833 filling the pore space between clay minerals. Regions of lower occupation were  
 834 commonly observed to consist of sub-units composed of clay platelets aligned face-  
 835 to-face and/or edge to face (c-d) and clay minerals arranged around a central  
 836 bacteria (see Fig. 5a). EPS can be observed filling the nm and μm pores within the  
 837 floc matrix (e).

838

## **Characterising the composition and multiscale structure of suspended sediment aggregates using 2D and 3D correlative microscopy**

### Highlights:

- Imaging workflow developed enabling multiscale floc properties to be explored for first time
- Correlative imaging enables visualisation and quantification of floc composition and structure
- Range of scale-dependent interactions observed that highlight the non-fractal nature of flocs

1 **Development of novel 2D and 3D correlative microscopy to characterise the**  
2 **composition and multiscale structure of suspended sediment aggregates.**

3

4 Jonathan A.T. Wheatland <sup>a,b,c</sup>, Kate L. Spencer <sup>c</sup>, Ian G. Droppo <sup>d</sup>, Simon J. Carr <sup>c,e</sup>  
5 Andrew J. Bushby<sup>a,b,\*</sup>

6 <sup>a</sup> School of Engineering & Materials Science, Queen Mary University of London, Mile  
7 End Road, London E1 4NS, UK

8 <sup>b</sup> The NanoVision Centre, Queen Mary University of London, Mile End Road, London  
9 E1 4NS, UK

10 <sup>c</sup> School of Geography, Queen Mary University of London, Mile End Road, London  
11 E1 4NS, UK

12 <sup>d</sup> Environment and Climate Change Canada, 867 Lakehouse Road, P.O. Box 5050,  
13 Burlington, Ontario L7S 1A1, Canada

14 <sup>e</sup> Department of Science, Natural Resources and Outdoor Studies, University of  
15 Cumbria, Ambleside, Cumbria LA22 8BB, UK

16 \* Corresponding author. Email address: [a.j.bushby@qmul.ac.uk](mailto:a.j.bushby@qmul.ac.uk)

17

18 **Abstract**

19 Suspended cohesive sediments form aggregates or ‘flocs’ and are often closely  
20 associated with carbon, nutrients, pathogens and pollutants, which makes  
21 understanding their composition, transport and fate highly desirable. Accurate  
22 prediction of floc behaviour requires the quantification of 3-dimensional (3D)  
23 properties (size, shape and internal structure) that span several scales (i.e.  
24 nanometre [nm] to millimetre [mm]-scale). Traditional techniques (optical cameras  
25 and electron microscopy [EM]), however, can only provide 2-dimensional (2D)

26 simplifications of 3D floc geometries. Additionally, the existence of a resolution gap  
27 between conventional optical microscopy (COM) and transmission EM (TEM)  
28 prevents an understanding of how floc nm-scale constituents and internal structure  
29 influence mm-scale floc properties. Here, we develop a novel correlative imaging  
30 workflow combining 3D X-ray micro-computed tomography ( $\mu$ CT), 3D focused ion  
31 beam nanotomography (FIB-nt) and 2D scanning EM (SEM) and TEM (STEM) which  
32 allows us to stabilise, visualise and quantify the composition and multi-scale  
33 structure of sediment flocs for the first time. This new technique allowed the  
34 quantification of 3D floc geometries, the identification of individual floc components  
35 (e.g., clays, non-clay minerals and bacteria), and characterisation of particle-particle  
36 and structural associations across scales. This novel dataset demonstrates the truly  
37 complex structure of natural flocs at multiple scales. The integration of multi scale,  
38 state-of-the-art instrumentation/techniques offers the potential to generate  
39 fundamental new understanding of floc composition, structure and behaviour.

#### 40 **Keywords**

41 Aquatic sediments, sediment aggregates, flocs, multiscale imaging, 2D and 3D  
42 correlative microscopy

43

#### 44 **1. Introduction**

45 Cohesive fine-grained sediments and mixed sediments in suspension influence a  
46 wide array of environmental processes and material transfers, including the  
47 transport, fate and effect of carbon, nutrients, microbiota (including pathogens) and  
48 pollutants within lakes, rivers, estuaries and the marine environment (Azam & Long  
49 2001; Rusconi et al. 2014; Rummel et al. 2017). Understanding the composition and  
50 behaviour of cohesive and mixed sediments is therefore a major issue for the

51 management of aquatic environments. However, in suspension this biotic and abiotic  
52 particulate matter forms loosely bound, complex and fragile aggregates, or 'flocs'.  
53 Flocs exhibit hydrodynamics (e.g., transport dynamics and settling) that differ  
54 significantly from those of their constituent particles (Droppo 2001; Burd & Jackson  
55 2009; Manning et al. 2010).

56 To predict the movement of cohesive sediments requires accurate  
57 quantification of floc properties that control their behaviour (e.g., size, shape,  
58 porosity and density) (Soulsby et al. 2013). Additionally, an understanding of floc  
59 composition and particle associations provides a mechanistic understanding of e.g.,  
60 pathogen and pollutant transport and elucidates microbial dynamics (Liss 2002). Yet,  
61 obtaining such empirical data is challenging since flocs are inherently fragile and  
62 their properties often span several spatial scales, i.e. nm to mm-scale. Flocs are  
63 routinely characterised based on their 'gross' scale properties (e.g., external size and  
64 shape) that can be measured in situ relatively simply and non-destructively. Floc  
65 camera systems (e.g., LabSFLOC, Manning & Dyer 2002) and laser diffraction  
66 particle sizers (e.g., LISST, Agrawal & Pottsmith 2000) are commonly used and  
67 provide additional measurements of floc settling velocities. Internal floc  
68 characteristics (e.g., structure, density and porosity) cannot be measured directly  
69 using these methods, but can be estimated using Stokes' Law and the assumption of  
70 spherical shape and fractal behaviour, i.e. structural self-similarity (Winterwerp 1998;  
71 Jarvis et al. 2005). Alternatively, sub- $\mu\text{m}$  structures and the internal composition can  
72 be observed by, for instance, TEM (Leppard et al. 1996) or optical measurement of  
73 cell colonisation (e.g., Nguyen et al. 2017). However, there is no one method that  
74 allows floc structure and composition to be observed at all relevant spatial scales or  
75 that reflects the inherent 3D nature of these characteristics. A major challenge

76 therefore is the development of methods that enable empirical observation and  
77 accurate quantification of floc characteristics, correlated across multiple length-  
78 scales.

79         The combined application of two or more imaging methods, known as  
80 correlative microscopy, overcomes the resolution limitations associated with using a  
81 single imaging technique (Liss et al. 1996; Burnett et al. 2014). Previously, COM has  
82 been applied correlatively with confocal laser scanning microscopy (CLSM) and TEM  
83 enabling the investigation of floc mm-and nm-scale properties (Leppard 1992;  
84 Droppo et al. 1996; Liss et al. 1996; Leppard et al. 1996). Observations using this  
85 approach have provided valuable insights into floc structure-function relationships,  
86 highlighting the importance of floc-colonising microorganisms and their associated  
87 exopolymeric substances (EPS) (Droppo 2001; Tolhurst et al. 2002). However, the  
88 use of these imaging methods in a truly correlative manner is hindered by the  
89 specific preparation requirements, differences in contrast mechanisms, lack of  
90 overlap in resolution and their 2-dimensionality. Methods that can combine different  
91 spatial scales and similar contrast mechanisms with both 2D and 3D information are  
92 needed to understand delicate floc structures that include both organic and inorganic  
93 materials that extend across multiple scales. The combination of X-ray tomography  
94 with EM has the capability to achieve this across length-scales from mm to nm and  
95 the resolution gap can be closed. Furthermore, with similar sample preparation  
96 procedures, both imaging techniques can be applied to a single floc sample. Such  
97 methods have been used within materials science to visualise and quantify complex,  
98 multiscale structures from the cm to nm-scale (Handschuh et al. 2013; Burnett et al.  
99 2014), and in the biological sciences (Bushby et al. 2012), but have not yet been  
100 applied to study natural environmental samples.

101             $\mu$ CT and FIB-nt are both capable of imaging complex samples in 3D.  $\mu$ CT is  
102 capable of analysing volumes at a higher resolution than COM, and for small  
103 samples can reach a resolution of tens of  $\mu$ m down to submicrometre (Cnudde &  
104 Boone 2013). It is non-destructive and thus suited to imaging delicate samples,  
105 including sediments and hydrated, flocculated clays (e.g., Sharma et al. 2017; Zhang  
106 et al. 2018). FIB-nt is capable of resolutions approaching that of TEM (c. 10 nm,  
107 Holzer et al. 2004), and occupies a niche between TEM and  $\mu$ CT. Although FIB-nt is  
108 destructive, delicate samples can be stabilised to preserve their integrity during  
109 analysis (e.g., Bushby et al. 2011), and it has recently been successfully applied to  
110 investigate the internal structure of hydrated flocs (Wheatland et al. 2017).  
111 Significantly, both  $\mu$ CT and FIB-nt provide quantitative data (Holzer et al. 2004;  
112 Ketcham & Carlson 2001), which can be used to characterise suspended sediment  
113 flocs and potentially parameterise computational models that describe floc  
114 behaviour.

115            The aim of this study is to develop a correlative workflow that enables  
116 observation, characterisation and quantification of natural suspended sediment floc  
117 structure and composition from the mm to nm-scale for the first time. This workflow,  
118 which combines 3D  $\mu$ CT and FIB-nt with 2D SEM and STEM, is applied to the  
119 investigation of natural estuarine sediment flocs. Based on feature greyscale, size  
120 and morphology criteria are developed to distinguish floc components (e.g., clay  
121 minerals, bacteria etc.) observed at different spatial scales, which are used to  
122 segment the datasets.

123

124 **2. Materials and Methods**

125 **2.1. Considerations for Correlative Imaging**

126 Several challenges exist for the correlative imaging of sediment flocs. Firstly, fragile  
127 flocs must be sampled and stabilised and contrast agents (e.g., stains) applied to  
128 enable feature recognition using different imaging modalities operating at different  
129 scales (Wheatland et al. 2017).  $\mu$ CT and EM share similar contrast mechanisms  
130 allowing object(s) of interest to be identified and correlated between datasets.  
131 However, electron-dense stains must be introduced to allow organics to be  
132 distinguished. Secondly, to achieve correlation between the different imaging  
133 methods, datasets must be registered using fiducial markers that can be imaged by  
134 all methods. Thirdly, the process of identifying nm-scale datasets nested within mm-  
135 scale samples is represents a significant challenge (Bushby et al. 2011; Burnett et al.  
136 2014). Therefore, workflows must follow a targeted approach whereby a sample is  
137 sequentially imaged at a finer scale and/or by a complimentary modality, the data  
138 from which is used to selected further regions of interest (RoI) for analysis at higher  
139 resolutions. Finally, the imaging methods used should each adequately resolve both  
140 the biotic and abiotic floc components for correlation. For example,  $\mu$ CT maps X-ray  
141 attenuation and hence images the density of an object or concentration of floc  
142 constituents at the  $\mu$ m to mm-scale. In comparison, SEM (using secondary and  
143 backscattered electrons) provides information on morphology and elemental  
144 composition at the nm to  $\mu$ m-scale. Combining this information enables important  
145 features (e.g., a pore space, clay mineral or bacteria) to be identified at different  
146 scales and resolutions. Once features have been identified, they can be segmented,  
147 quantified and visualised in both  $\mu$ CT and FIB-nt.

148

149 **2.2. Floc Capture and Stabilisation**

150 Natural sediment collected from the Thames Estuary, SE England. These sediments  
151 are typically fully saline, fine grained silty clays with organic content typically < 10%  
152 (measured as % loss on ignition, e.g., O'Shea et al. 2018). Sediment was added to  
153 an artificial seawater solution (Sigma sea salts 34 g L<sup>-1</sup>) and gently agitated using a  
154 magnetic stirrer to induce flocculation. Fragile flocs were sampled following the  
155 protocol outlined in Droppo et al. (1996), which involved settling flocs directly into  
156 plankton chambers and immobilising flocs in agarose gel.  $\mu$ CT scans of a test  
157 sample (FS0, see Fig. S1 of Supplementary Materials) were conducted in order to  
158 assess potential artefacts associated with this technique (e.g., particle-particle  
159 overlap, Droppo et al. 1996). Immobilised flocs were subsequently prepared for  
160 imaging following the block staining protocol outlined in Wheatland et al. (2017). Floc  
161 samples were rendered vacuum stable by resin embedding, which included the  
162 addition of electron dense stains (e.g., uranyl acetate etc.) to improve the contrast of  
163 organic constituents. Following resin embedding, fiducial markers (aluminium wire, c.  
164 0.5 mm diameter) were implanted in the base of each resin block for the purpose of  
165 data co-registration (see Section 2.3). Aluminium was selected as it could be easily  
166 distinguished from natural sedimentary material using all imaging methods  
167 (Hands Schuh et al. 2013).

168

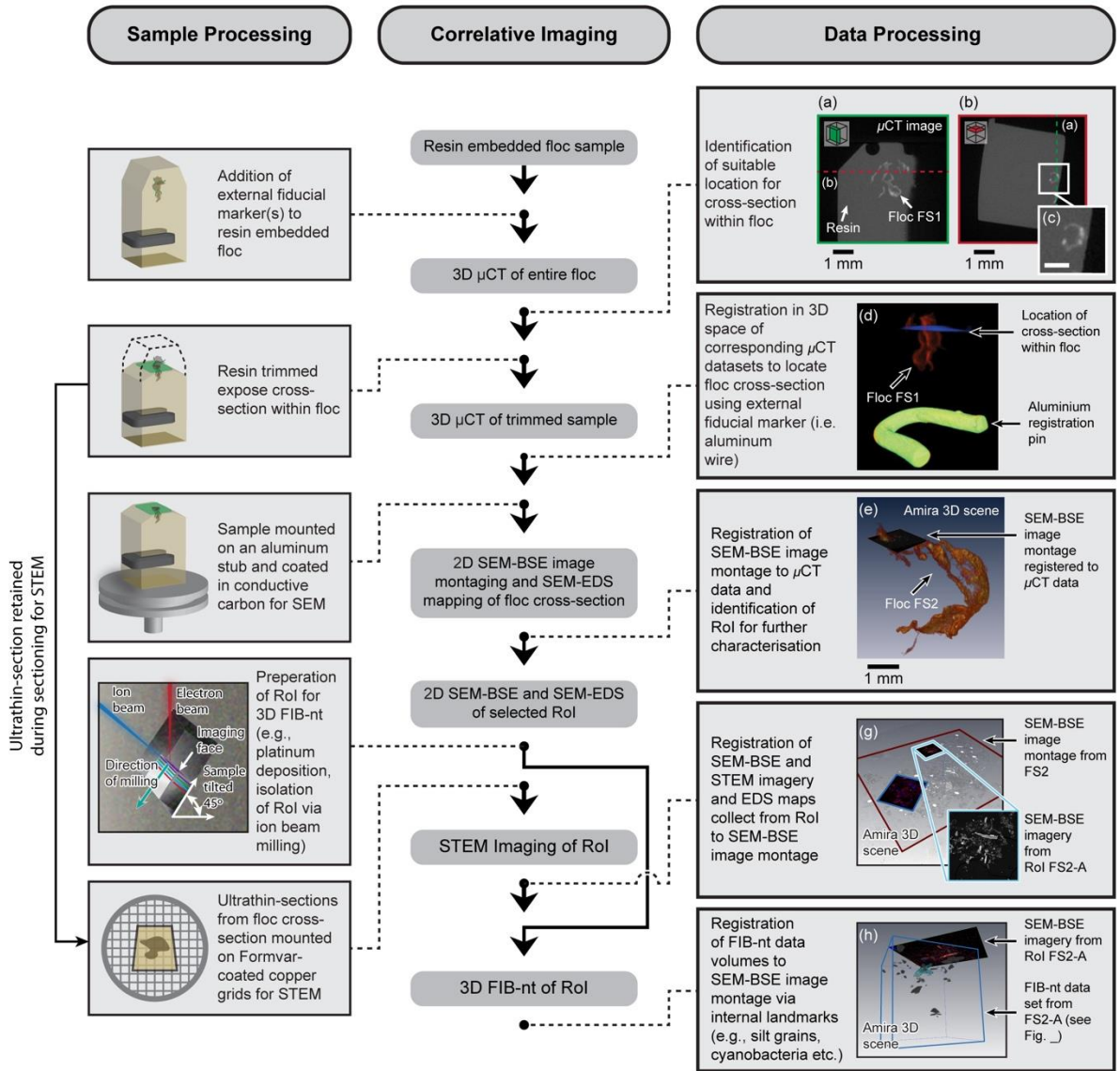


**Figure 1.** Flow diagram outlining the various stages in the correlative imaging workflow, including steps required for sample and data processing. Images (a) and (b) are orthogonal slices from the  $\mu$ CT scan of floc FS1. Grey-scale variations reflect regions of high and low X-ray attenuation (c), and indicate variability of floc constituents and structure at the sub-voxel scale. This information helps guide the selection of a suitable site for a cross-section within the floc which is exposed via ultramicrotomy. The precise location of the cross-section within the floc is then verified by re-scanning the sample using  $\mu$ CT and registering the two corresponding  $\mu$ CT datasets using the aluminium registration pin (d). 2D SEM-BSE image montages of the floc cross-section, obtained to identify suitable Rol for further analysis, are then registered to the  $\mu$ CT data (e). Following 2D SEM-BSE imaging, Rol are prepared for 3D FIB-nt (h). 2D SEM-BSE and STEM imagery and 3D FIB-nt data obtained from Rol can be registered to the image montage based on ‘internal’ fiducial markers (e.g., silt grains, cyanobacteria etc.) that can be identified in the corresponding datasets (g and h).

### 170 **2.3. Description of the Correlative Workflow**

171 The correlative workflow developed for investigating floc composition and multiscale  
172 structure is shown in Fig. 1. Low-resolution  $\mu$ CT scans (3D pixel or 'voxel' size, c. 10  
173  $\mu\text{m}^3$ ) were initially conducted to characterise floc size and morphology and identify  
174 RoI for further analysis (Fig. 1a and b). At this resolution individual floc constituents  
175  $<100\ \mu\text{m}$  (e.g., bacteria and clay minerals) cannot be resolved. However, variations  
176 in X-ray attenuation (Fig. 1c and Fig. S2 of Supplementary Materials) indicate the  
177 variability of floc constituents and structure at the sub-voxel scale. Subsequently,  
178 selected RoIs were exposed by trimming the resin-block using an ultramicrotome  
179 (Leica UCT ultramicrotome), creating a smooth cross-section suitable for 2D SEM  
180 and 3D FIB-nt. During this process, ultrathin-sections (thickness, 70–100 nm) cut  
181 directly adjacent to the cross-section were retained for STEM (Fig. 1).

182 The accurate co-registration of  $\mu\text{m}$  and nm-scale EM datasets with mm-scale  
183  $\mu$ CT scans relied on the location and characterisation of the cross-section created  
184 within the floc. Therefore, samples were re-scanned using  $\mu$ CT following  
185 ultramicrotomy to locate the floc cross-section within the original  $\mu$ CT data (Fig. 1d).  
186 This was facilitated by 'external' fiducial markers (aluminium wire) identifiable in the  
187 corresponding  $\mu$ CT datasets (Fig. 1d, see section 3.1.1). To ensure these repeat  
188 scans were directly comparable to the original  $\mu$ CT data and accurate co-  
189 registration, the position of the mechanical stage, manipulator settings (i.e. voltage  
190 and current) and resolution were kept constant.

191 2D SEM-BSE image montaging of the cross-section (block-face SEM) then  
192 provided the context within which to locate 3D FIB-nt volumes and 2D STEM  
193 imagery based on identification of 'internal' landmarks within the floc (Fig. 1g and h).  
194 Landmarks were selected that could be identified across scales and imaging

195 modalities, e.g., silt grains and cyanobacteria (see Table 1). Image montages were  
 196 obtained by systematic imaging using 2D SEM, resulting in 10's – 100's of images  
 197 that were stitched together to provide a 'panoramic' view of the entire cross-section  
 198 (pixel resolution, c. 100 nm<sup>2</sup>). Following SEM imaging, elemental maps were  
 199 obtained from selected ROI via energy dispersive X-ray spectroscopy (SEM-EDS)  
 200 which, in conjunction with contrast and morphological information from SEM  
 201 imagery, enabled identification and mapping of materials.

202 2D SEM imagery and EDS maps informed the selection suitable sites for 3D  
 203 FIB-nt. Representativity is a key consideration when selecting parameters for FIB-nt  
 204 (i.e. volume size and resolution), and must be optimised to resolve features of  
 205 interest and ensure that a representative number of particles are characterised for  
 206 statistical analysis (Bushby et al. 2011). Natural flocs are compositionally complex,  
 207 containing particles of varying morphology and size (e.g., blocky silt grains, platy  
 208 clays, and filamentous organics), and high-resolution datasets are desirable (10-15  
 209 nm) to characterise individual particles. However, a trade-off must be made between  
 210 the resolution and volume size to ensure the  $\mu$ m-scale structures into which floc  
 211 constituents are organised are adequately characterised.

212

Imaging Technique; Successive Techniques Applied →							
CT Datasets		SEM-BSE Montaging		SEM and STEM		FIB-nt	
Material	Identification Criteria	Material	Identification Criteria	Material	Identification Criteria	Material	Identification Criteria
<i>Floc</i>	Mid-range greyscale (c. 19,000 – 40,000)	<i>Floc Matrix</i>	Material with diameter c. <10 $\mu$ m, low to mid-range greyscales (c. 20 – 200)	<i>Clay Minerals</i>	2D planar morphology, size c. <5 $\mu$ m, mid-range greyscale (c. 10 - 170)	<i>Clay minerals</i>	3D planar morphology, size c. <5 $\mu$ m, mid-range greyscale (c. 10 - 170)
	Variability in composition and structure at the sub-voxel scale		Regions of low and high occupation	<i>Microbial Cells</i>	Small size (c. <10 $\mu$ m), high greyscale (c. 200 - 250),	<i>Cell Morpho-type</i>	Five cell morphotypes recognised based on

	recognised based on X-ray attenuation: low greyscale values (c. 25,000 – 40,000) correlated to regions of low-occupation, high greyscale values (c. 19,000 – 25,000) correlated to regions of high-occupation	identified based on greyscale, e.g., low occupation c. <50, high occupation c. >70		differential staining of subcellular structures		criteria outlined in Dazzo & Niccum (2015) (see Fig. 5)	
					<i>Intra-cellular Integrity</i>	Three categories of intracellular integrity (indicative of metabolic state) recognised based on criteria outlined by Heissenberger et al. (1996) (see Fig. 5)	
			<i>Organo-Mineral Debris</i>	Geometric structure, mid-range greyscale (c. 10 - 170)	<i>Organo-Mineral Debris</i>	Geometric structure, mid-range greyscale (c. 10 - 170)	
			<i>EPS</i>	Fibrillar material, diameter (2 – 15 nm)	NA		
		<i>Non-Clay Minerals</i>	Blocky/irregular morphology, particle size c. 5 – 40 µm, mid-range greyscales (c. 20 – 100)	<i>Non-Clay Minerals</i>	Blocky/irregular morphology Particle size c. 5 – 40 µm, mid-range greyscales (c. 20 – 100)	<i>Non-Clay Minerals</i>	Blocky/irregular morphology Particle size c. 5 – 40 µm, mid-range greyscales (c. 20 – 100)
		<i>Bio-Organic Material</i>	Irregularly shaped, high greyscales (c. 200 – 255)	<i>Bio-Organic Material</i>	Irregularly shaped, high greyscales (c. 200 – 255)	<i>Bio-Organic Material</i>	Irregularly shaped, high greyscales (c. 200 – 255)
		<i>Resin External to the Floc</i>	Resin external to the floc matrix, grey-scale (c. 0 – 20)	<i>Resin External to the Floc</i>	0 – 20	NA	
<i>Resin</i>	Low greyscale (c. 7,000 – 17,000)	<i>Resin Filled Pore-Space</i>	Resin filled pores within the floc matrix, low grey-scale (c. 0 – 20). NB only possible to resolve pores with diameter >30 µm	<i>µm-Scale Pore</i>	Resin filled pores within the floc matrix, low grey-scale (c. 0 – 20), diameter <10 µm	<i>µm-Scale Pore</i>	Resin filled pores within the floc matrix, low grey-scale (c. 0 – 20), diameter <10 µm
				<i>nm-Scale Pores</i>	Resin filled pores within the floc matrix, low grey-scale (c. 0 – 20), diameter >10 µm	<i>nm-Scale Pores</i>	Resin filled pores within the floc matrix, low grey-scale (c. 0 – 20), diameter >10 µm

---

<i>Aluminium</i>	High greyscale
<i>Pin</i>	(c. 45,000 – NA 65,535)

---

213 **Table 1.** Materials identified within the various 2D and 3D datasets, and the criteria used for their  
214 identification/segmentation, e.g., size, morphology, and greyscale characteristics. Note, that the  $\mu$ CT  
215 are 16-bit and therefore have a pixel depth of 65,535 greyscales, whereas the SEM and STEM  
216 imagery and FIB-nt data volumes are 8-bit with a 256 greyscale range.

217

218 Ultrathin-sections collected adjacent to the surface of the cross-section during  
219 ultramicrotomy were mounted on Formvar-covered copper grids (Gilder Grids) and  
220 coated in conductive carbon for STEM. STEM provided details of the pore space  
221 that cannot be obtained using SEM. Additionally, high-resolution elemental analysis  
222 via STEM X-ray spectroscopy (STEM-EDS) conducted on floc cross-section (SEM-  
223 EDS) enabled the precise classification of individual floc constituents that cannot be  
224 achieved via SEM-EDS.

225

## 226 **2.4. Acquisition of Image Data**

### 227 **2.4.1. 3D $\mu$ CT**

228  $\mu$ CT scans were performed using a Nikon Metrology XT-H 225 (Tokyo, Japan)  
229 micro-tomograph. This scanner was configured with a 25-225 kV 0-2000  $\mu$ A X-ray  
230 source with tungsten reflection target capable of generating polychromatic X-rays  
231 (focal spot size, c. 3  $\mu$ m), and a Perkin Elmer (Waltham, Massachusetts, USA) 16-bit  
232 flat-panel detector. Scan parameters were set to optimise contrast and resolution  
233 (voltage 150 kV; current 160  $\mu$ A; acquisition time between projections 2829 ms) with  
234 2-frame averaging. Maintaining the same scan parameters for all  $\mu$ CT scans  
235 ensured comparability between datasets. The greyscale values of resulting

236 projections represented differences in X-ray energy attenuation, related to material  
237 density and the attenuation coefficient of the materials being imaged.

238

#### 239 **2.4.2. 2D SEM, STEM and EDS**

240 2D SEM image montaging (block-face SEM) was conducted using an FIB-SEM (FEI  
241 Quanta 3D FEG, Hillsboro, Oregon, USA) fitted with a low-kV backscattered electron  
242 detector. Backscattered electron (BSE) images were collected at 3 kV accelerating  
243 voltage and 4 nA beam current to minimise the electron beam interaction volume  
244 and improve the spatial resolution of the BSE signal. Greyscale contrast of BSE  
245 images typically reflects composition. Systematic imaging of the floc cross-section  
246 generated 100's of images (pixel resolution, c. 30 – 60 nm<sup>2</sup>). Images were  
247 subsequently stitched together into montages using the Grid/Collection Stitching  
248 plugin in open source software FIJI/ImageJ (Preibisch et al. 2009).

249 SEM-EDS elemental maps, STEM images and STEM-EDS point spectra were  
250 obtained using an FEI Inspect-F SEM fitted with a split field STEM detector  
251 (Hillsboro, Oregon, USA) and equipped with an Oxford Instruments (Oxford, UK)  
252 INCA X-act energy dispersive X-ray spectrometer. For low-resolution SEM-EDS  
253 mapping of the entire floc cross-section and high-resolution elemental mapping of  
254 Rol (see section 2.3) an accelerating voltage of 10 kV (counting period, 10 – 30 min).  
255 Counting periods varied between Rol and were selected to minimise damage to the  
256 sample surface. Dark-field STEM imaging of the ultrathin-sections was achieved at  
257 an accelerating voltage of 30 kV. Point spectra (STEM-EDS) were obtained from  
258 individual particles, at an accelerating voltage of 10 kV.

259

### 260 **2.4.3. 3D FIB-nt Data Volumes**

261 3D FIB-nt was performed using a FIB-SEM (FEI Quanta 3D FEG, Hillsboro, Oregon,  
262 USA) following the protocol outlined by Bushby et al. (2011). This relied on using the  
263 automated serial sectioning and imaging software Slice & View software (FEI  
264 Hillsboro, Oregon, USA). Experimentation revealed an accelerating voltage of 30 kV  
265 and a current of 0.5 – 5 nA for the ion beam to be optimal for milling. Images were  
266 captured using the BSE signal detector operated at a voltage of 3 kV and current of  
267 4 nA, selected to match those used for 2D SEM (see section 2.4.2). The accuracy of  
268 FIB-nt relies on the stability of the FIB during milling and its ability to maintain regular  
269 intervals (i.e. slice thicknesses) between consecutive slices. An automated  
270 correction algorithm was applied during the serial sectioning procedure, which  
271 reduces or eliminates drift phenomena.

272

### 273 **2.4.4. Reconstruction and Segmentation of the 3D Data**

274 The product of  $\mu$ CT and FIB-nt are 2D projections/images of the sample/volume of  
275 interest that must be reconstructed to generate 3D volumes for visualisation and  
276 quantification. The reconstruction of  $\mu$ CT datasets was conducted using CTPro 3D  
277 (Nikon, Tokyo, Japan). Each scan generated 1,609 raw X-ray projections, yielding  
278 volumes with dimensions of  $1,024 \times 1,024 \times 1,024$  voxels (voxel size resolution, 10  
279  $\mu\text{m}^3$ ). During reconstruction artefacts (e.g., beam hardening, Ketcham & Carlson  
280 2001) were addressed by the application of specific algorithms. FIB-nt datasets were  
281 reconstructed following the protocol outlined by Bushby et al. (2011) using  
282 FIJI/ImageJ v2 (Schindelin et al. 2012). The number of images comprising FIB-nt  
283 datasets varied depending on the size of the analysed volume, ranging between 400

284 – 600 images. During setup for FIB-nt the mill thickness was adjusted to match the  
285 pixel resolution of the images, ensuring an isotropic voxel size suitable for  
286 quantitative analysis (Bushby et al. 2012).

287

#### 288 **2.4.5. Visualisation and Quantification of the Correlative Datasets**

289 The quantification and visualisation of both  $\mu$ CT and FIB-nt datasets was conducted  
290 in in FIJI/ImageJ and required material segmentation, i.e. the classification of  
291 material phases based on greyscale values and/or shape, a critical stage in image  
292 processing (Cnudde & Boone 2013). Segmentation was achieved via greyscale  
293 thresholding or using a semi-automated segmentation tool plugin (Trainable WEKA  
294 Segmentation, TWS v2.1.0) capable of machine learning (Arganda-Carreras et al.  
295 2017). The choice between these segmentation methods was guided by appraisal of  
296 dataset complexity, including the number of bulk phases and the overlap between  
297 phase greyscale envelopes common in natural environmental materials. Resulting  
298 binary volumes were then quantified using the 3DRoiManager plugin (Ollion et al.  
299 2013), which provided quantitative measurements of material properties, e.g., size,  
300 shape and greyscale intensities etc.

301

#### 302 **2.4.6. Co-Registration of Datasets**

303 The process of aligning multiscale datasets (i.e. co-registration) is a critical aspect of  
304 the correlative workflow, allowing information obtained using different imaging  
305 modalities and different spatial scales to be directly related. Co-registration of the  
306 multiscale 2D/3D datasets was achieved in the visualisation software Avizo (FEI  
307 Visualisation Sciences Group, Berlin, Germany). The success of registration is  
308 dependent upon the identification of fiducial markers in the different datasets. Co-

309 registration of  $\mu$ CT datasets relied upon the identification of the aluminium wire  
310 implanted within the resin block, whilst internal landmarks (e.g., silt particles, bacteria  
311 etc.) were used in the co-registration of higher resolution 2D and 3D datasets. Fig. 1  
312 shows the sequence of steps taken to co-register the correlative datasets. Coarse  
313 alignment was manually conducted using the Transform Editor tool within Avizo,  
314 while fine registration was conducted automatically using the Landmark Surface  
315 Warp module applied using a rigid transformation algorithm.

316

### 317 **3. Results and Discussion**

#### 318 **3.1. Overview of the Multiscale Datasets**

##### 319 **3.1.1. 3D Floc Sub-mm Structure and Internal Density**

320 Volumetric renderings of three floc samples (FS1, FS2 and FS3) generated based  
321 on the  $\mu$ CT data (resolution, c.  $10 \mu\text{m}^3$ ) are shown in Fig. 2. For each 3D  
322 reconstruction greyscale contrast (16-bit pixel depth, e.g., 65,536 greyscales)  
323 between the flocs, surrounding resin and aluminium fiducial markers was sufficient to  
324 allow segmentation based on simple thresholding. This is illustrated in Fig. 1a and b  
325 that show cross-sectional greyscale images taken from the reconstructed  $\mu$ CT scan  
326 of FS1, in which the floc and surrounding resin are easily distinguishable. Scan  
327 parameters were kept constant for each of the flocs, and thus datasets are directly  
328 comparable. Table 1 details the criteria (e.g., greyscale range, size and shape etc.)  
329 for identify the different material phases; i) resin ii) floc, and iii) aluminium registration  
330 pin. The result of the segmentation procedure was a binary masks which formed the  
331 basis for subsequent visualisations and quantitative analysis (Fig. 2 and Table 2).

332 Quantitative analysis of the floc samples showed FS2 to have the largest  
333 volume, with a total occupied volume (i.e. voxel count) of  $5.04 \times 10^8 \mu\text{m}$  (Table 2).

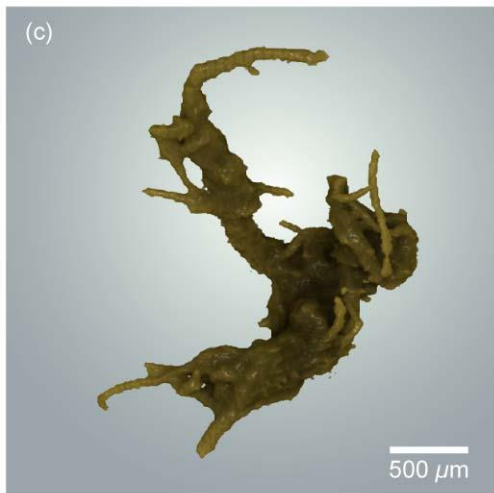
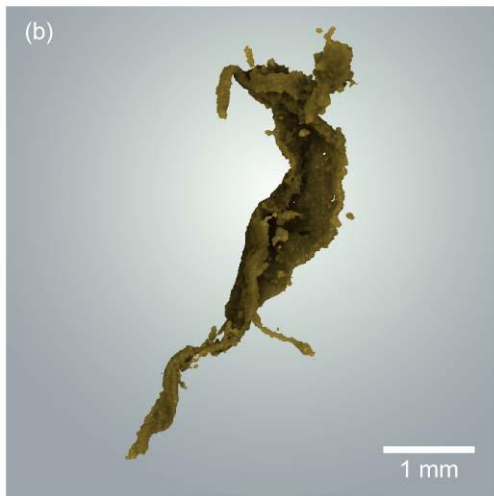
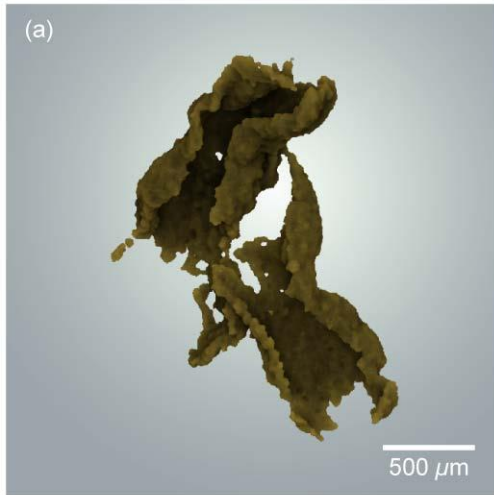


**Figure 2.** 3D visualisations of the floc samples FS1 (a) and FS2 (b) and FS3 (c) generated in Drishti from X-ray  $\mu\text{CT}$  data.

334 Descriptions of floc diameter ( $D$ ) and height to width ratios ( $H/W$ ) were made using  
335 the Feret diameter, i.e. the distance between two parallel planes enclosing an object.

336 Based on these the floc samples can be described as macroflocs ( $D > 160 \mu\text{m}$ ;  
 337 Manning & Dyer 2002) that exhibit elongate ( $H/W > 2:1$ ) and highly contorted  
 338 morphologies. Flocs FS2 and FS3 exhibit filamentous protuberances projecting  
 339 beyond their peripheries, likely related to the presence of cyanobacteria (confirmed  
 340 by SEM, STEM and FIB-nt dataset, see sections 3.1.2, 3.1.3 and 3.1.4). FS1 was  
 341 observed to differ significantly from FS2 and FS3, being composed of three distinct  
 342 sub-units, connected by narrow linkages  $c. \leq 30 \mu\text{m}$ . Each of the floc samples  
 343 exhibited regions of high and low X-ray attenuation (Table 1 and Fig. 2c and Fig. S2  
 344 of Supplementary Materials). The distribution of regions of high attenuating elements  
 345 within floc FS2 are shown in a 3D rendering in Fig. S2 of Supplementary Materials.  
 346 This information provided a means of identifying RoI for further analysis (see Section  
 347 3.1.2 and Fig. 3a-c and Fig. S3 of Supplementary Materials).

348

Floc Sample	Floc Volume ( $\mu\text{m}^3$ )	Feret Diameter ( $\mu\text{m}$ )			H/W
		Major	Intermediate	Minor	
FS1	$1.95 \times 10^8$	2414.54	1298.65	631.29	3:1
FS2	$5.04 \times 10^8$	11183.83	755.82	266.06	4:1
FS3	$2.44 \times 10^8$	945.03	800.19	323.23	2:1

349 **Table 2.** 3D quantitative measures of floc geometry (volume and Feret diameter) and  
 350 shape (height/width ratio).

351

### 352 **3.1.2. 2D Floc Micrometre-Structure and Composition Revealed in** 353 **Cross-Section**

354 Fig. 3c shows the 2D SEM-BSE image montage collected from the cross-section of  
 355 floc FS1 (resolution,  $c. 60 \text{ nm}^2$ ), (FS2, resolution,  $c. 30 \text{ nm}^2$  and individual SEM-EDS

356 elemental maps are shown in Fig. S2 and Fig. S4 respectively). Similar to  $\mu$ CT,  
 357 greyscale contrast (8-bit pixel depth, e.g., 256 greyscales) was sufficient to allow  
 358 flocculated material to be segmented from surrounding resin. However, the higher  
 359 resolution of SEM also enabled the recognition of additional floc components, which  
 360 could be classified based on particle size, shape and greyscale value and further  
 361 validated by comparison with SEM-EDS elemental maps. Four additional materials  
 362 were identified; i) resin filled pore-space, ii) floc matrix (e.g., clays, unicellular  
 363 bacteria, organo-mineral debris), iii) individual non-clay mineral grains (e.g., quartz,  
 364 feldspar and mica) and iv) large bio-organic and organic structures (e.g., organic  
 365 detritus, diatoms, cyanobacteria) (Table 1 and Fig. 3d). Particles  $<10\ \mu\text{m}$  (e.g., EPS,

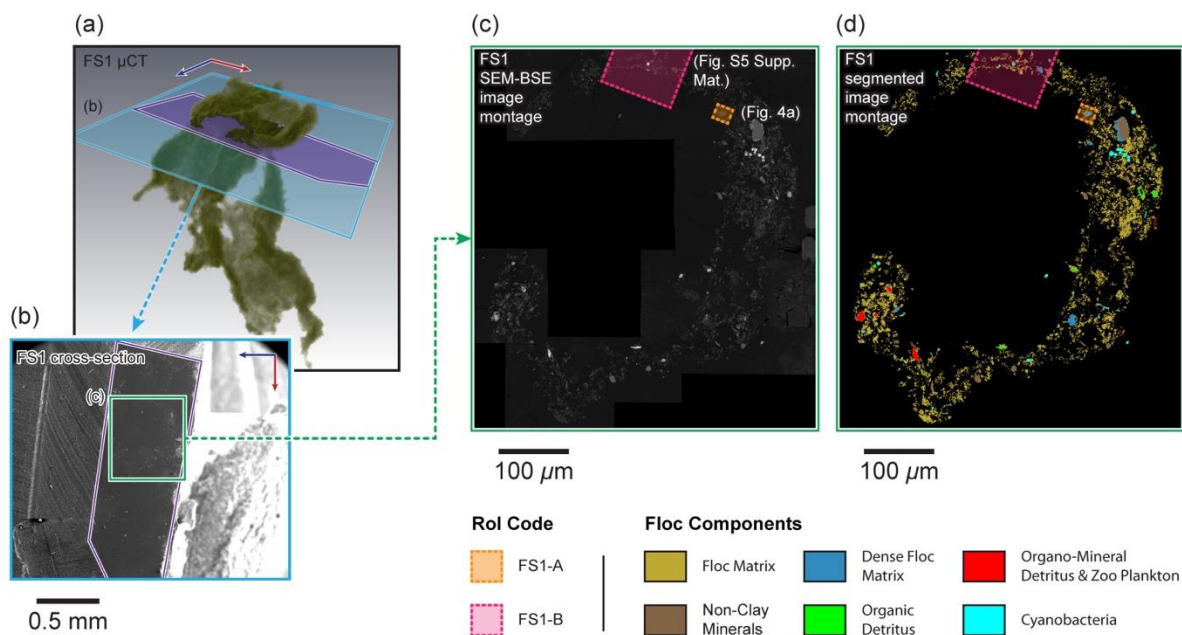


**Figure 3.** Analysis of the cross-section located in floc FS1. The location of the cross-section created within FS1 is shown in (a) and the region of the cross-section containing the floc is shown in (b). The trapezoidal shape of the sectioned block is highlighted in purple both in (a) and (b), while the boundary of the SEM image of the cross-section shown in (b) is defined in 3D space in (a) in blue. The SEM-BSE image montage (c) obtained from the cross-section through floc FS1 enabled the identification of floc constituents (d) and characterisation of floc structure in 2D. The locations of Rol selected for further analysis are shown in (c) and (d).

366 clay minerals and unicellular bacteria) could not be accurately segmented and were  
367 identified collectively as 'floc matrix'. The floc matrix is likely to be compositionally  
368 complex, however, SEM-EDS revealed strong signals for Fe, Al/Si and Si (Fig. S4 of  
369 Supplementary Materials), indicating the presence of iron oxyhydroxides, clay  
370 minerals and silicates. Constituents were unevenly distributed within the floc matrix,  
371 with regions of low occupation characterised by high porosity and low greyscale  
372 values (c. <50) and regions of high occupation exhibiting low porosity and high  
373 greyscale values (c. >70) (Fig. 3 and Table 1).

374 Non-clay mineral grains were differentiated based on their blocky/irregular  
375 morphology, uniform greyscale and elemental signature (Si, Fe). In comparison, bio-  
376 organic material and biota could be identified relatively easily based on their high  
377 greyscale values (c. 200 – 255) due to heavy metal (Pb, Os and U) staining (see  
378 also elemental phase map, Fig. S4 of Supplementary Materials). Strong signals for  
379 Pb, Os and U related to heavy metal-stained organics, typically large features  
380 (diameter, >10 µm) such as cyanobacteria and organic detritus, while an associated  
381 signal of Si (blue) was indicative of eukaryotic plankton (e.g., diatom, foraminifera).

382

### 383 **3.1.3. 2D Submicrometre and Nanometre Structure and Composition of** 384 **Selected Rol**

385 For each floc several Rol were identified based on structural and/or compositional  
386 characteristics revealed in SEM-BSE imagery and SEM-EDS elemental maps (see  
387 Section 3.1.2). Fig. 3 and Fig. S3 of Supplementary Materials show the locations of  
388 Rols selected for FS1 and FS2 respectively. Rols were targeted to either  
389 characterise further floc nm composition and particle-particle interactions via STEM,

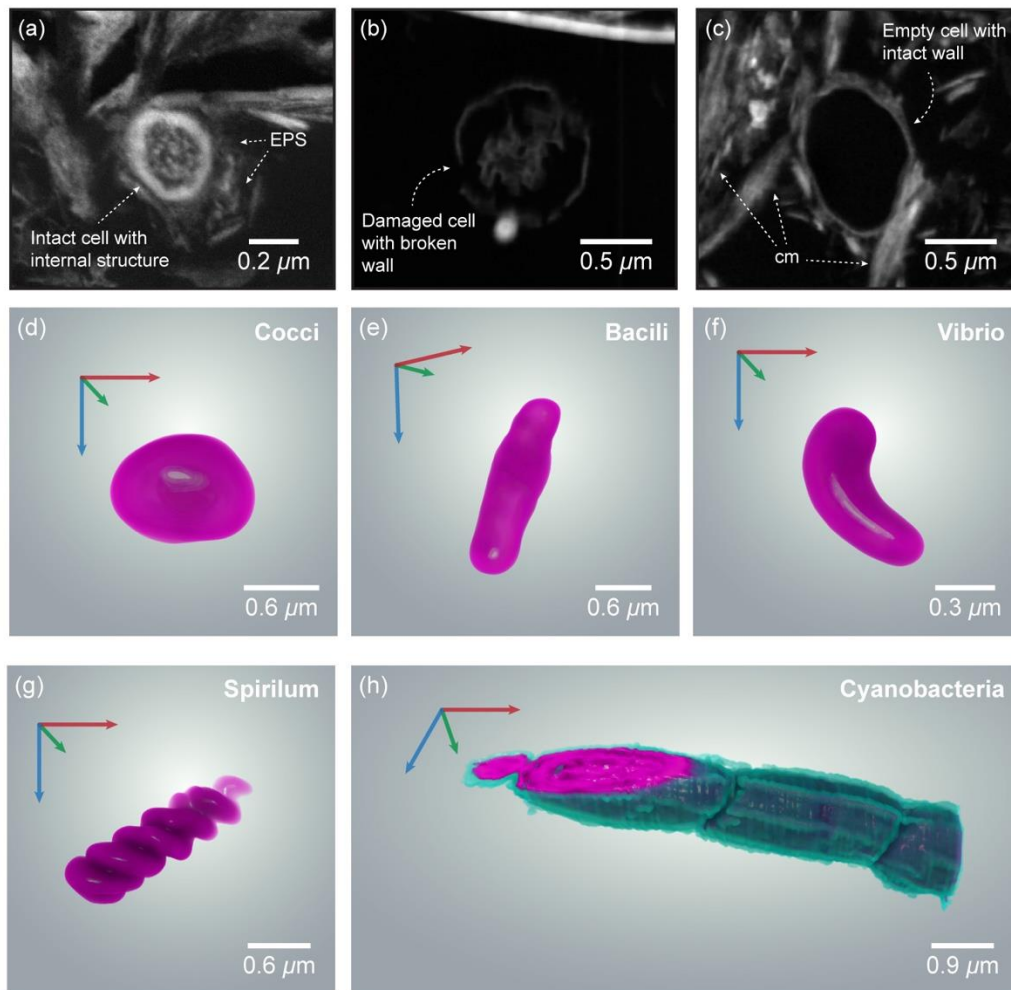


**Figure 5.** Characterisation of bacterial cells. (a – c) STEM images showing examples of the three categories of intracellular integrity used as an indicator of the fidelity of stabilised flocs to their original structure. (d – g) Examples of different bacterial cellular morphologies reconstructed based on 3D FIB-nt data. (a) intact bacteria displaying an undamaged cell wall, cytoplasm (grainy structure) and nucleoplasm (denser region towards the centre of the cell); (b) damaged bacterial cell with a broken cell wall and degraded cytoplasm and/or nucleoplasm; (c) empty cell lacking plasma. (d) cocci, (e) bacilli, (f) vibrio, (g) spirillum and (h) cyanobacteria.

390 or selected for SEM imaging to define submicrometre structure. Selected SEM-BSE  
 391 (resolution, c. 25 - 30 nm<sup>2</sup>) and STEM (resolution, c. 5 - 10 μm<sup>2</sup>) imagery and  
 392 corresponding SEM-EDS elemental maps are shown in Fig. 4 and Fig. S5 of  
 393 Supplementary Materials.

394 The four main floc constituents (pore-space, floc matrix, non-clay mineral  
395 grains, and large bioorganic and organic structures) were also identified in SEM-BSE  
396 and STEM imagery. However, the higher resolution enabled further distinction  
397 between materials within the floc matrix: i) clay minerals, ii) microbial cells, iii)  
398 organo-mineral debris, and iv) EPS (Table 1). Microbial cells could be easily  
399 identified due to their high greyscale values (c. >200) and differential staining of  
400 subcellular structures (Fig. S5 of Supplementary Materials). High-resolution STEM  
401 imagery revealed internal/external cell structure allowing the classification of  
402 microbes based on their metabolic state (Heissenberger et al. 1996) as: i) intact, ii)  
403 damaged and iii) empty (e.g., Fig. 5a – c). Whilst the resolution of SEM imagery  
404 prevented the detection of EPS 2 – 20 nm in diameter (Leppard 1992), its presence  
405 is confirmed by STEM imagery (Fig. S6 of Supplementary Materials). EPS was  
406 observed to be closely associated or ‘bound’ to the cell walls of metabolically active  
407 microbes, whilst ‘soluble’ EPS exuded by microorganisms was found throughout the  
408 floc matrix and often associated with clay minerals (Fig. S6 of Supplementary  
409 Materials).

410 To investigate density variations within the floc matrix (see Section 3.1.2, Fig.  
411 3 and Figs. S3 and S4 of Supplementary Materials), Rols FS1-A and FS2-B (Fig. 4a  
412 and e) were selected to encompass regions exhibiting high and low occupation.  
413 Within both high and low occupation regions clay minerals were rarely observed in  
414 isolation, but were observed in units of 10’s of particles. STEM imagery revealed  
415 several common particle associations, including units of clay platelets aligned face-  
416 to-face and/or edge to face, and clay minerals arranged around a central bacterium  
417 (Fig. S6 of Supplementary Materials). Low density regions of the floc matrix mainly  
418 consisted of particle associations arranged in open, ‘card-house’ structures, and

419 were highly porous (Fig. 4a). STEM showed the nanometre pore space between  
420 primary particles filled with exopolymeric material, whilst EPS was notably absent in  
421 the larger micrometre pore channels (Fig. S6 of Supplementary Materials). In  
422 comparison, high density areas consisted primarily of closely packed clay minerals  
423 dispersed with pyrite (Fe+S) (Fig. 4c), and had a lower porosity and high organic  
424 signal (Fig. 4d).

425

#### 426 **3.1.4. 3D Submicrometre-Structure and Composition of Selected Rol**

427 Volumetric renderings of two FIB-nt volumes obtained from FS2, labelled FS2-A and  
428 FS2-B and corresponding to the Rol of the same name (see Fig. 4e and Fig. S5 of  
429 Supplementary Materials), are shown in Figs. 6 and 7 respectively. The large volume  
430 size of FS2-A (c.  $8 \times 10^4 \mu\text{m}^3$ , voxel size c. 67 nm) enabled the organisation of large  
431 submicrometre structures to be revealed in 3D, while the higher resolution of FS2-B  
432 (c.  $5 \times 10^3 \mu\text{m}^3$ , voxel size c. 15 nm) allowed for the detailed characterisation of  
433 constituents and particle-particle associations.

434 FIB-nt datasets were segmented following Wheatland et al. (2017). The  
435 primary floc constituents (resin filled pore-space, floc matrix, non-clay minerals, and  
436 large bioorganic and organic structures) and floc matrix constituents (clays minerals,  
437 microbial cells and organo-mineral debris) identified in 2D SEM and STEM were also  
438 identified in FIB-nt (Table 1 and Fig. 6 and 7). Additionally, the enhanced spatial  
439 resolution of FS2-B enabled the segmentation of closely packed particles c.  $<2 \mu\text{m}$   
440 (e.g., clays within the floc matrix), enabling their reconstruction in 3D (Fig. 7e). This  
441 is demonstrated in Fig. 7d in which individual clays can be discriminated in 2D slices  
442 from the FIB-nt dataset. Several of the particle-particle associations identified within  
443 SEM and STEM data (see Section 3.1.3 and Fig. S6 of Supplementary Materials)

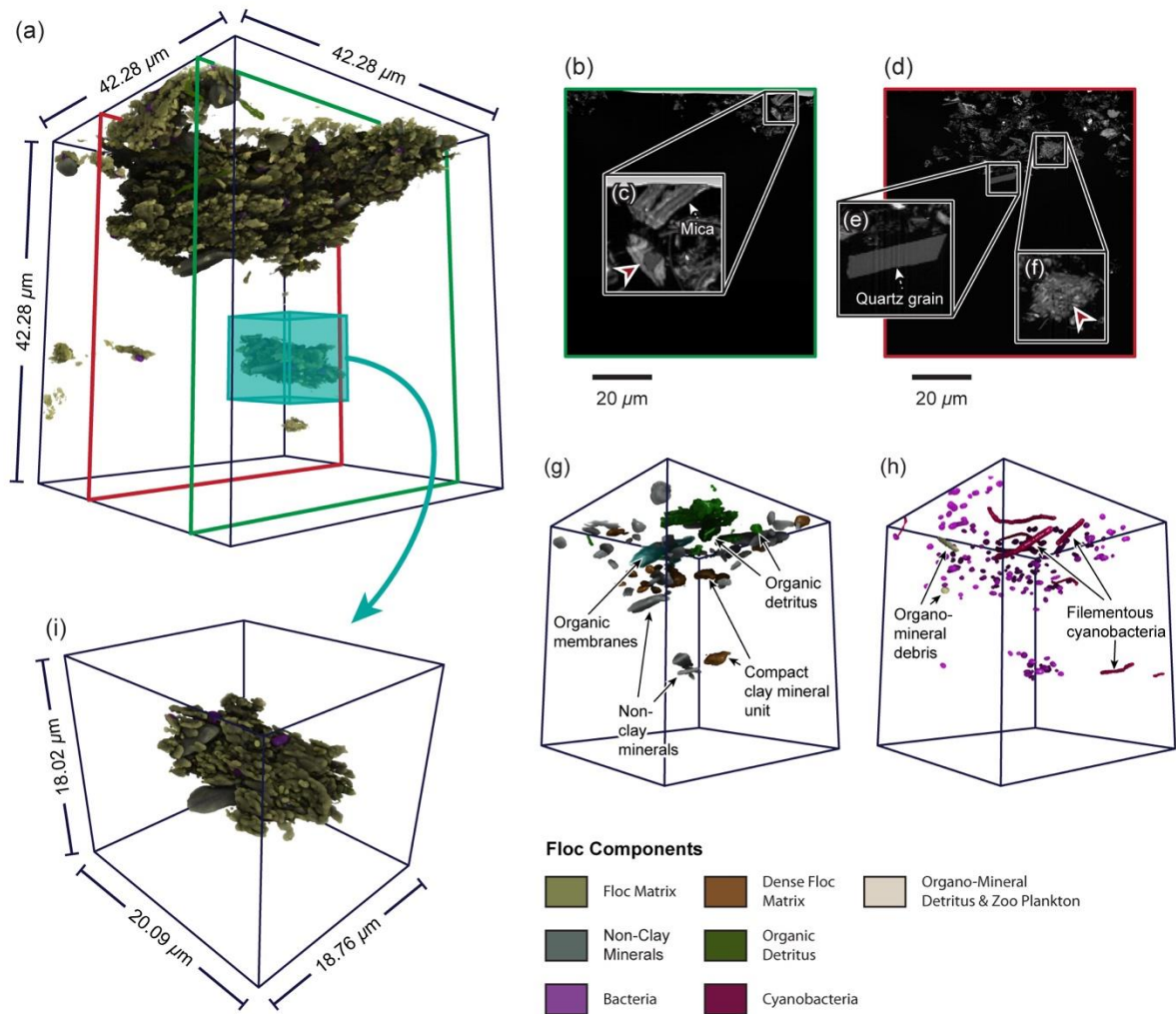


**Figure 6.** 3D reconstructions of the FIB-nt volume Rol FS2-A: (a) 3D rendering of the segmented components identified within FS2-A; (b - c) Selected BSE images from the FIB-nt dataset illustrating the differences in grey-scale and morphology that enable feature segmentation, note the red arrow shown in (c) highlights a region of high particle occupation. The locations from which the 2D BSE images shown in (b) and (c) were taken from within the FIB-nt dataset are indicated by coloured lines shown in (a); (g) Same as (a) but with selected materials rendered transparent to reveal the non-clay minerals, organic membranes and amorphous organic detritus; (h) Same as (a) but with certain materials rendered transparent to reveal the individual bacteria, cyanobacteria and organomineral debris (diatom frustules); (e) Sub-volume taken for FS2-A showing an isolated microfloc (location indicated in (a)).

444 were also identified in FS2-B. Visualised in 3D these structures are revealed to be  
 445 discrete units, separable from surrounding floc matrix by nanopores (Fig. 7e and f).

446 Fig. 7e shows a particle association consisting of clay minerals aligned face-to-face,  
447 while Fig. 7f shows clay particles aligned around a central bacterium. Examination of  
448 the floc matrix reveals micrometre pore channels delineating the boundaries of  
449 discrete structural units 10's  $\mu\text{m}$  in diameter (e.g., Fig. 6i). These structures usually  
450 consist of several particle-particle associations and larger primary particles (e.g., silt  
451 grains, organic detritus), loosely arranged in an open, card-house structure, linked  
452 together by filamentous cyanobacteria.

453 Quantification reveals the occupied volume of FS2-A largely consists of  
454 inorganic material, with clays accounting for c. 98% of occupied space and non-clay  
455 minerals c. 0.5% (Table 3). In contrast, a larger proportion of FS2-B is occupied by  
456 organics, which accounted for c. 34% of the occupied volume compared to inorganic  
457 material, c. 66%. Within both FIB-nt datasets micrometre pore channels can be  
458 identified together with elongated nanopores throughout the floc matrix (Fig. 6 and  
459 7). Combined, these give a total porosity of c. 95 % and c. 52 % for FS2-A and FS2-  
460 B respectively. The resolution and 3D nature of the datasets enabled the  
461 classification of microbial cells based on morphotype (Dazzo & Niccum 2015) and  
462 five categories were recognised: i) cocci, ii) regular straight rods (e.g., bacilli), iii)  
463 curved/U-rods (e.g., vibrio), iv) spirals (e.g., spirilla) and v) unbranched filaments  
464 (e.g., cyanobacteria) (Fig. 6d - h). Cocci were characterised as near spherical  
465 (length/width, <2:1) with diameters <1.5  $\mu\text{m}$  (Fig. 6h), frequently forming groups of  
466 several cells. In comparison, bacilli exhibited a straight, rod-like morphology  
467 (length/width, <16:1) and were larger (diameter, c. 2  $\mu\text{m}$ ). Cells with a crescent  
468 curvature (comma-shaped) were identified as vibrio, and had similar dimensions to  
469 bacilli (Fig. 5d – h). Although observed less frequently, spirilla were classified as  
470 elongated cells displaying a distinctive repeated waveform (e.g., corkscrew-shaped).

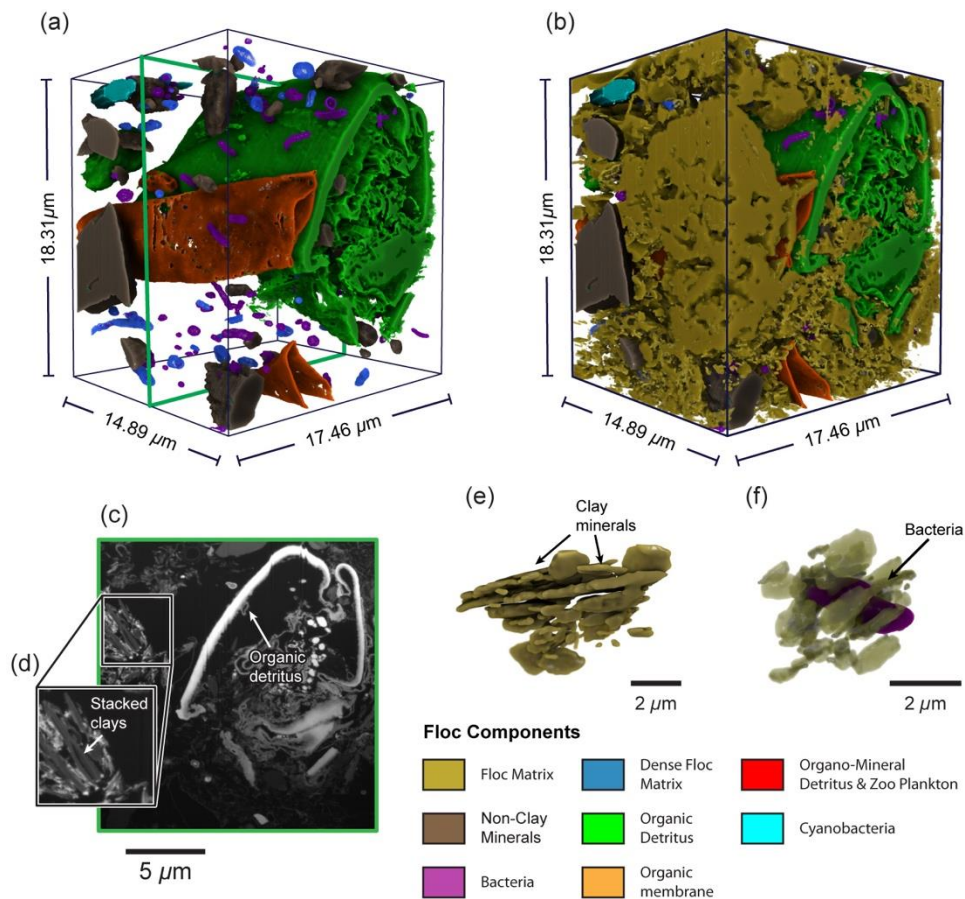


**Figure 7.** 3D reconstructions of the FIB-nt volume Rol FS2-B: (a) 3D rendering of the segmented components identified within FS2-B; (c) Selected BSE image from the FIB-nt dataset illustrating the differences in grey-scale and morphology that enable feature segmentation. The locations from which the 2D BSE image shown in (c) was taken from within the FIB-nt dataset are indicated by the green coloured line shown in (a); (d) Sub-set from (c) showing clay minerals aligned face-to-face and/or edge-to-face; (e) 3D reconstruction of (d); (f) Clay particle arranged radially around a bacterial cell (bacteria false-coloured purple).

471 Filamentous (cyanobacteria) bacteria could be easily distinguished from other cell  
 472 types based on elongated shape (length/width, >16:1), and were present in a  
 473 number of forms, ranging from cells 1 – 2 μm in diameter to larger varieties  
 474 (diameters, c. >3 μm) (Fig. 5h). The quantities of cell morphotypes and their  
 475 intracellular integrity (e.g., intact, damaged or empty, Heissenberger et al. 1996) are  
 476 shown in Table 4.

FIB-nt Sample	Total Volume ( $\mu\text{m}^3$ )	Floc Constituents (Vol. %)						
		Porosity		Floc Matrix			Other	
		Micro-Porosity	Nano-Porosity	Clay Minerals	Bacteria	Organo-Mineral Debris	Organic Detritus	Non-Clay Minerals
FS2-A	c. $8 \times 10^4$	91.4	3.80	4.08	0.07	0.01	0.23	0.41
FS2-B	c. $5 \times 10^3$	-	51.79	31.96	0.45	0.07	17.16	2.15

477 **Table 3.** Volume fractions for the segmented components of FIB-nt datasets FS2-A  
478 and FS2-B.

479

FIB-nt Sample	Total Bacteria (Count)	Intracellular Integrity (% of Total Count)		Cell Morphotype (% of Total Count)				
		Intact Cells	Damaged and Empty Cells	Cocci	Regular Straight Rod	Curved/U-Rod	Unbranched Filament	Spiral
FS2-A	239	73.2	26.8	48.95	28.03	17.57	5.44	0
FS2-B	118	76.4	23.6	41.53	32.20	19.49	4.24	2.54

480 **Table 4.** Total count of bacteria, numbers of intact, damaged and empty cells and  
481 proportions of different cell morphotypes identified in FIB-nt datasets FS2-A and  
482 FS2-B.

483

484

### 485 **3.2. Validation of Floc Stabilisation Method**

486 Interpretation and quantification of 3D flocs relies on an assumption that the  
487 characteristics observed are representative of true floc structure and not artefacts of  
488 sampling, storage and preparation (Liss et al. 1996; Wheatland et al. 2017). The  
489 correlative workflow demonstrated above permits the validation of floc integrity in this  
490 context by enabling observation of 3D floc structure across multiple spatial scales.

491 Fluid exchanges and sample dehydration are essential for the chemical  
492 stabilisation process, but can result in the distortion and/or rupture of delicate cellular  
493 structures. While a number of cells identified in the 3D FIB-nt datasets were  
494 classified as either damaged or empty (Heissenberger et al. 1996) (Table 4),  
495 Wheatland et al. (2017) notes that the presence of damaged cells in itself is not  
496 indicative of inadequate stabilisation, since active microbial communities contain  
497 cells of all states of life including decay. More diagnostic of the state of preservation  
498 is the presence of intact cells, as rupture due to poor stabilisation would be expected  
499 to be systemic. Within the FIB-nt datasets intact cells accounted for c. >50% of the  
500 total number of cells, a higher percentage compared than that of the total number of  
501 metabolically active bacteria usually found in natural microbial communities (c.  
502 <30%, Ward & Johnson 1996). The loss of soluble EPS (i.e. EPS unassociated with  
503 bacterial cells) from the floc matrix during fluid exchanges can result in severe  
504 perturbation (Leppard et al. 1996). Previous studies have estimated up to 50–80% of  
505 EPS can be removed in certain instances from the floc matrix following stabilisation  
506 (Leppard et al. 1996), with the primary effect on the floc being the rearrangement of  
507 primary particles and compression of floc structures (recorded as shrinkage) (Liss et  
508 al. 1996). STEM imagery obtained from the floc samples reveals the presence of  
509 exopolymeric material, observed as dense networks in the nanometre pore space  
510 between primary particles (e.g., clays and bacteria) and distributed throughout the  
511 floc matrix (Fig. S6 of Supplementary Materials). This suggest that the little  
512 extraction of the EPS network within the floc matrix has taken place. The use of  
513 plankton chambers for floc capture and agarose gel for floc immobilisation help  
514 minimise the destructive forces associated with traditional sampling methods (e.g.,  
515 floc breakage via pipetting) (Droppo et al. 1996). However, morphological changes

516 can result if flocs interact once settled, e.g., false aggregation of flocs and/or  
517 pseudoplastic contortion of delicate structures with overburden pressure.  
518 Examination of flocs of immobilised in agarose prior to resin embedding provides a  
519 means of assessing the degree of interaction between neighbouring flocs. 2D cross-  
520 sectional images taken from the  $\mu$ CT of test sample FS0 (Fig. S1 of Supplementary  
521 Materials) reveal minimal overlap between neighbouring floc particles, suggesting  
522 morphological changes to be minimal. This is supported by the 3D visualisation of  
523 individual flocs (FS1, FS2 and FS3, Fig. 3 and Movie 1) that indicate delicate  
524 structures (e.g., filamentous protuberances, Fig. 3b and c) remained intact following  
525 settling and during the addition of agarose and sub-sampling for stabilisation.

526

### 527 **3.3. Merits of the Correlative Workflow**

528 This imaging workflow enables for the first time floc composition and 3D structure to  
529 be investigated at all relevant spatial scales, from primary particles to entire flocs  
530 several mm in size. This represents a significant advance in our ability to  
531 characterise flocs, filling the resolution gap between traditional imaging techniques  
532 (e.g., TEM, CLSM and COM) (Fig. 8).

533 The success of the workflow critically depends upon the quality (i.e. resolution,  
534 signal-to-noise ratio) and degree of similarity (i.e. resolution and mechanisms for  
535 contrast generation) between the different datasets (Caplan et al. 2011; Handschuh  
536 et al. 2013). Image quality is of particular importance, since it determines the  
537 accuracy with which features can be identified, segmented and quantified. Within  
538  $\mu$ CT and EM datasets the boundaries between objects are not always well defined,  
539 but can consist of a transitional zone 3 – 5 pixels wide (Holzer et al. 2014;  
540 Wheatland et a. 2017). Depending on the pixel/voxel resolution of the dataset the

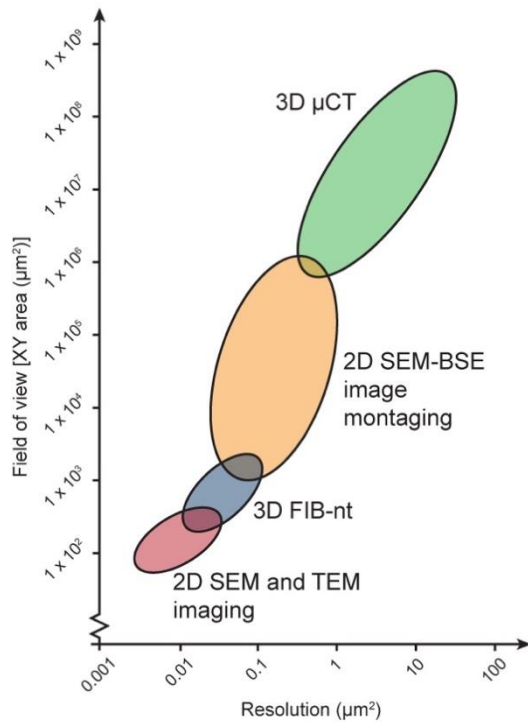


**Figure 8.** Length-scales over which the 2D and 3D imaging techniques employed within correlative workflow operate, with corresponding typical cross-section (XY) and resolution achievable by each technique. Note that the imaging methods used overlap, enabling truly correlative examination of floc structure from the nm to mm-scale.

541 maximum error is usually considered to be half the width of this zone. Further  
 542 discussion regarding the process of segmentation and potential errors is outlined in  
 543 Wheatland et al. (2017).

544 Fig. 3 shows the correlative 2D and 3D datasets collected from FS1 registered  
 545 in a single 3D scene. To locate the floc cross-section, aluminium wire was used as a  
 546 fiducial marker to register the  $\mu$ CT data collected after ultramicrotomy to the original  
 547  $\mu$ CT dataset of the intact flocs (see Section 2.3 and Fig. 1d). Segmentation of the

548 aluminium wire would ideally result in it being represented by similar number voxels

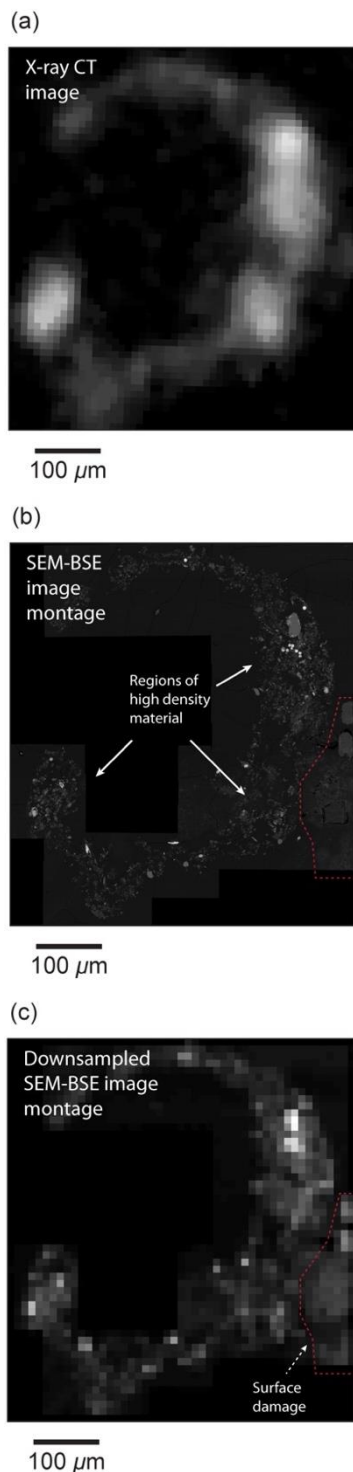


**Figure 9.** Comparison of  $\mu\text{CT}$  with SEM-BSE. Down-sampling the pixel size of the SEM-BSE image montage (c) to match that of the  $\mu\text{CT}$  data (c.  $10\ \mu\text{m}$ ), enabled comparison between the SEM-BSE image montage (b) and corresponding  $\mu\text{CT}$  slice (a). This provides a means of validating the potential floc structures responsible for different greyscale values within the  $\mu\text{CT}$  dataset. Regions of the floc observed to contain high concentrations highlighted in (b) of particles in the BSE-SEM image montages were shown to exhibit high grey-scale values in the  $\mu\text{CT}$  dataset (a).

549 in the corresponding  $\mu$ CT datasets. Within both pairs of  $\mu$ CT data the wire was easily  
550 segmented from other material phases based on its high greyscales (e.g., see  
551 Section 3.1.1 and Fig. 2). However, discrepancies in the size of the segmented  
552 aluminium wire were observed – 1.6% for FS1 and 3.8% for FS2 – which likely  
553 resulted from scan artefacts, i.e. secondary edge effects due to partial volume effect.  
554 Assuming an even distribution of the extraneous voxels around the surface area of  
555 the aluminium fiducial marker, the minimum offset between co-registered datasets  
556 can be estimated to be of the order of less than a voxel (c. 3 – 6  $\mu$ m) over a total 3D  
557 size of  $10 \times 10^8 \mu$ m. With evidence of only minor peripheral misalignment of the  
558 registered datasets, the co-registration of the 3D  $\mu$ CT scans has been successful.

559 2D SEM-BSE image montages of the floc cross-sections were critical for the  
560 co-registration of 2D and 3D nm and  $\mu$ m datasets with the sub mm-scale 3D  $\mu$ CT  
561 data. The trapezoidal shape of the cross-sections (Fig. 3b and Fig. S3 of  
562 Supplementary Materials) can be defined in the  $\mu$ CT datasets, enabling the SEM-  
563 BSE image montages to be tied to the surface within an accuracy of 3 – 6 voxels (c.  
564 30 – 60  $\mu$ m). However, further confidence in the accuracy of the co-registration can  
565 be obtained by comparing the actual shape of the floc boundary depicted in the two  
566 datasets. Reducing the pixel resolution of the SEM-BSE image montages (i.e. down-  
567 sampling) to match that of the  $\mu$ CT datasets (c. 10  $\mu$ m) enables a direct comparison  
568 between the SEM-BSE image montages and  $\mu$ CT data (Fig. 9), which indicates the  
569 error to be less than a voxel (c. <10  $\mu$ m). In addition, the features responsible for the  
570 variations observed in  $\mu$ CT greyscale values, that reflect the variability of floc  
571 constituents and structure at the sub-voxel scale (representing the impact of partial  
572 volume effects, cf. Ketcham & Carlson 2001), can be confirmed by comparing the  
573 down-sampled SEM-BSE image montage with the corresponding  $\mu$ CT slice. Fig. 9

574 demonstrates that regions of the SEM-BSE image montage identified as containing  
575 high concentrations of particles correspond to regions of high attenuation (high  
576 greyscales) within  $\mu$ CT. The similar imaging conditions selected for both SEM-BSE  
577 imaging (montaging and imaging of Rol) and FIB-nt allowed reference landmarks  
578 within the corresponding datasets to be recognised with a high degree of certainty  
579 (20 – 60 nm). As the contrast mechanisms in both SEM-BSE and dark-field STEM  
580 are similar (related to atomic number) fiducial markers internal to the floc (e.g., silt  
581 grains and bacteria etc.) could be easily identified. However, inspection of the  
582 overlaid STEM images following co-registration with SEM imagery revealed  
583 discrepancies in the positions of these markers. These displacements are likely the  
584 result of ultramicrotomy, as shear stresses imposed during sectioning are known to  
585 cause thin-section compression (Peachey 1958).

586

### 587 **3.4 Applications of 3D Floc Structural and Compositional Data**

588 Providing such detailed 3D analysis of flocs is not readily applicable for field scale  
589 quantification of suspended sediment aggregates. However, this technique has the  
590 potential, through targeted experimental or field campaigns, to provide new  
591 understanding of floc composition and controls on floc characteristics and structures.  
592 For example, these datasets quantify 3D floc characteristics (e.g., size, shape and  
593 porosity) that are critical input parameters to cohesive sediment transport models.

594       Additionally, the datasets demonstrate the complex structural associations and  
595 particle-particle interactions found at different spatial scales and levels of  
596 aggregation. These are frequently hypothesised in the literature or inferred from 2D  
597 observations of gross floc characteristics (e.g., Maggi et al. 2007; Lee et al. 2011).  
598 These particle-particle associations reflect the materials present in suspension

599 during floc development and their interactions. Here, the particle associations  
600 including clays oriented face-to-face and/or edge-to-face likely occur due to a  
601 combination of electrochemical interactions (i.e. cohesion), and the additional  
602 binding forces provided by organic materials resulting in bioflocculation, i.e. adhesion  
603 (Liss et al. 1996; Righetti & Lucarelli 2010). Yet the short distances ( $10^1$  to  $10^3$  nm)  
604 over which these forces (cohesion and adhesion) operate mean that these structures  
605 are clearly scale-dependent. Larger structural units consisting of several particle-  
606 particle associations and individual primary particles (e.g., silt grains, amorphous  
607 organic detritus etc.) were found throughout the floc samples. Therefore, this new  
608 method could provide data to challenge or validate simplified descriptors of floc  
609 structure e.g., self-similarity or fractal geometry (e.g., Khelifa & Hill 2006).

610 Our data also demonstrate and quantify the microbial associations with  
611 flocculated material. For example, demonstrating the importance of cell morphotype  
612 on floc shape and strength. Here, filamentous cyanobacteria cross-link smaller  
613 structural units (observed in 2D SEM and 3D FIB-nt) promoting interactions between  
614 these structural units and providing structural connectivity and flexibility (e.g.,  
615 Nguyen et al. 2007). Their strongly elongate shape and propensity to align has a  
616 strong influence on floc development, promoting the growth of non-spherical flocs.  
617 Additionally, filaments extending from the periphery of the flocs provide anchor  
618 points to facilitate floc growth through interactions with other flocs (Burger et al  
619 2017).

620

#### 621 **4. Conclusion**

622 The development of a novel correlative workflow provides datasets demonstrating  
623 the complex composition and multiscale 3D structure of aquatic sediment flocs. This

624 work provides the most detailed floc structural analysis to date and provides the  
625 following specific advantages:

- 626 • 2D and 3D imaging techniques can be applied in a systematic manner to  
627 successfully obtain a complete set of overlapping, co-registered datasets from  
628 a single floc sample. The resultant datasets enable the identification and  
629 quantification of floc composition and structures across multiple length-scales.  
630 This approach improves on traditional 2D correlative microscopy by providing  
631 truly correlative datasets that are quantifiable.
- 632 • The orientation of multi-scale and multi-modal datasets in 3D space presents  
633 a significant challenge, but can be successfully overcome using fiducial  
634 markers. This is reliant on selecting imaging techniques that share similar  
635 contrast mechanisms, to ensure that landmark features can be detected at  
636 different spatial scales.
- 637 • Particle-particle and structural associations can be directly related across  
638 length-scales. Structures that are scale-dependent can be recognised,  
639 providing further evidence for interactions that have previously been  
640 hypothesised. The imaging workflow therefore provides a means of obtaining  
641 quantitative measures of floc composition and structure and a better  
642 understanding of the mechanisms promoting floc growth.
- 643 • The correlative workflow is adaptable, and the potential exists for further  
644 research to design targeted experiments to explore relationships between floc  
645 structure and behaviour, controls on floc stability and structure, and floc  
646 microbial communities.

647

648 **Acknowledgements**

649 J.A.T.W. would like to thank the Engineering and Physical Sciences Research Council  
650 for the award of a scholarship and the Queen Mary University of London Postgraduate  
651 Research Fund. K.L.S, A.J.B and S.J.C acknowledge the Natural Environmental  
652 Research Council (NE/N011678/1) for funding. Jemima Burden (MRC Laboratory for  
653 Molecular Cell Biology, University College London) is thanked for her help with sample  
654 preparation.

655

## 656 **References**

- 657 Agrawal, Y.C., Pottsmith, H.C. 2000. Instruments for particle size and settling  
658 velocity observations in sediment transport. *Mar. Geol.* 168 (1–4), 89-114.
- 659 Arganda-Carreras, I., Kaynig, V., Rueden, C., Eliceiri, K.W., Schindelin, J.,  
660 Cardona, A., Seung, H.S. 2017. Trainable Weka Segmentation: a machine  
661 learning tool for microscopy pixel classification. *Bioinformatics* 33 (15), 2424-  
662 2426.
- 663 Azam, F., Long, R.A. 2001. Sea snow microcosms. *Nature* 414, 495-498.
- 664 Burd, A.B. Jackson, G.A. 2009. Particle aggregation. *Annu. Rev. Mar. Sci.* 1, 65-90.
- 665 Burger, W., Krysiak-Baltyn, K., Scales, P.J., Martin, G.J.O., Stickland, A.D., Gras,  
666 S.L. 2017. The influence of protruding filamentous bacteria on floc stability and  
667 solid-liquid separation in the activated sludge process. *Water Res.* 123, 578-  
668 585.
- 669 Burnett, T.L., McDonald, S.A., Gholinia, A., Geurts, R., Janus, M., Slater, T., Haigh,  
670 S.J., Ornek, C., Almuaili, F., Engelberg, D.L., Thompson, G.E., Withers, P.J.  
671 2014. Correlative tomography. *Sci. Rep.* 4, 1-6.

672 Bushby, A.J., Png, K.M.Y., Young, R.D., Pinali, C., Knupp C., Quantock A.J. 2011.  
673 imaging three-dimensional tissue architectures by focused ion beam scanning  
674 electron microscopy. *Nat. Protoc.* 6 (6), 845-858.

675 Bushby, A.J., Mariggi, G., Armer, H.E.J., Collinson, L.M. 2012. Correlative Light and  
676 Volume EM: Using Focused Ion Beam Scanning Electron Microscopy to image  
677 transient events in model organisms. *Methods Cell Biol.* 111, 357-382.

678 Caplan, J., Niethammer, M., Taylor, R.M., Czymmek, K.J. 2011. The power of  
679 correlative microscopy: multi-modal, multi-scale, multi-dimensional. *Curr. Opin.*  
680 *Struct. Biol.* 21 (5), 686-693.

681 Cnudde, V., Boone, M.N. 2013. High-resolution X-ray computed tomography in  
682 geosciences: A review of the current technology and applications. *Earth-Sci.*  
683 *Rev.* 23, 1-17.

684 Dazzo F.B., Niccum, B.C. 2015. Use of CMEIAS image analysis software to  
685 accurately compute attributes of cell size, morphology, spatial aggregation and  
686 color segmentation that signify in situ ecophysiological adaptations in microbial  
687 biofilm communities. *Computation* 3, 72-98.

688 Droppo, I.G. 2001. Rethinking what constitutes suspended sediments. *Hydrol.*  
689 *Process.* 15 (9), 1551-1564.

690 Droppo, I.G. 2003. A new definition of suspended sediment: implications for the  
691 measurement and prediction of sediment transport. In: Bogen, J., Fergus, T.,  
692 Walling, D. (Eds.), *Erosion and Sediment Transport Measurement in Rivers:*  
693 *Technological and Methodological Advances.* IAHS Publication No. 249,  
694 International Association of Hydrological Sciences, Wallingford, pp. 238.

695 Droppo, I.G., Flannigan, D.T., Leppard, G.G., Jaskot, C., Liss, S.N. 1996. Flocculation  
696 stabilization for multiple microscopic techniques. *Appl. Environ. Microbiol.* 62,  
697 3508-3515.

698 Handschuh, S., Baeumler, N., Schwaha, T., Ruthensteiner, B. 2013. A correlative  
699 approach for combining microCT, light and transmission electron microscopy in  
700 a single 3D scenario. *Front. Zool.* 10, 1-16.

701 Heissenberger A., Leppard, G.G., Herndl, G.J. 1996. Relationship between the  
702 intracellular integrity and the morphology of the capsular envelope in attached  
703 and free-living marine bacteria. *Appl. Environ. Microbiol.* 62 (12), 4521-4528.

704 Holzer, L., Indutnyi, F., Gasser, P.H., Münch, B., Wegmann, M. 2004. Three-  
705 dimensional analysis of porous BaTiO<sub>3</sub> ceramics using FIB nanotomography.  
706 *J. Microsc.* 216 (1), 84-95.

707 Jarvis, P., Jefferson, B., Gregory, J., Parsons, S.A. 2005. A review of floc strength  
708 and breakage. *Water Res.* 39 (14), 3121-3137.

709 Ketcham, R.A., Carlson, W.D. 2001. Acquisition, optimization and interpretation of X-  
710 ray computed tomographic imagery: applications to the geosciences. *Comput.*  
711 *Geosci.* 27, 381-400.

712 Khelifa, A. Hill, P.S. 2006. Models for effective density and settling velocity of flocs.  
713 *J. Hydraul. Res.* 44, 390-401.

714 Lee, B.J., Toorman, E., Molz, F., Wang, J., 2011. A two-class population balance  
715 equation yielding bimodal flocculation of marine or estuarine sediments. *Water*  
716 *Res.* 45, 2131–2145.

717 Leppard, G.G. 1992. Size, morphology and composition of particulates in aquatic  
718 ecosystems: solving speciation problems by correlative electron microscopy.  
719 *The Analyst* 117 (3), 595-603.

720 Leppard, G.G., Heissenberger, A., Herndl, G.J. 1996. Ultrastructure of marine snow.  
721 I. Transmission electron microscopy methodology. *Mar. Ecol. Prog. Ser.* 135,  
722 289-298.

723 Liss, S.N. 2002. Microbial Flocs Suspended Biofilms. In: Bitton, G. (Ed.),  
724 Encyclopaedia of Environmental Microbiology (Vol. 4). John Wiley and Sons,  
725 New York, NY, pp. 2000-2012.

726 Liss, S.N., Droppo, I.G., Flannigan, D.T., Leppard, G.G. 1996. Floc architecture in  
727 wastewater and natural riverine systems. *Environ. Sci. Technol.* 30 (2), 680-  
728 686.

729 Maggi, F., Mietta, F., Winterwerp, J.C. 2007. Effect of variable fractal dimension on  
730 the floc size distribution of suspended cohesive sediment. *J. Hydrol.* 343 (1-2),  
731 43-55.

732 Manning, A.J., Dyer, K.R. 2002. The use of optics for the in situ determination of  
733 flocculated mud characteristics. *J. Opt. A-Pure Appl. Op.* 4, 71-81.

734 Nguyen, T.H., Tang, F.H., Maggi, F. 2017. Optical Measurement of cell Colonization  
735 Patterns on Individual Suspended Sediment aggregates. *J. Geophys. Res.*  
736 *Earth Surf.* 122 (10), 1794-1807.

737 Nguyen, T.P., Hankins, N.P., Hilal, N. 2007. A comparative study of the flocculation  
738 behaviour and final properties of synthetic and activated sludge in wastewater  
739 treatment. *Desalination* 204 (1), 277-295.

740 Ollion, J., Cochenec, J., Loll, F., Escudé, C., Boudier, T. 2013. TANGO: a generic  
741 tool for high-throughput 3D image analysis for studying nuclear organization.  
742 *Bioinformatics* 29, 1840-1841.

743 O'Shea, F.T., Cundy, A.B, Spencer, K.L. The contaminant legacy from historic  
744 coastal landfills and their potential as source of diffuse pollution. *Mar. Pollut.*  
745 *Bull.* 128, 446-455.

746 Peachey, L.D. 1958. Thin Sections: I. A study of section thickness and physical  
747 distortion produced during microtomy. *J. Biophys. Biochem. Cytol.* 4 (3), 233-  
748 242.

749 Preibisch, S., Saalfeld, S., Tomancak, P. 2009. Globally optimal stitching of tiled 3D  
750 microscopic image acquisitions. *Bioinformatics* 25 (11), 1463-1465.

751 Righetti, M., Lucarelli, C. 2010. Resuspension phenomena of benthic sediments: the  
752 role of cohesion and biological adhesion. *River Res. Appl.* 26, 404-413.

753 Rummel, C.D., Jahnke, A., Gorokhova, E., Kühnel, D., Schmitt-Jansen, M. 2017.  
754 Impacts of Biofilm Formation on the Fate and Potential Effects of Microplastic in  
755 the Aquatic Environment. *Environ. Sci. Technol.* 4 (7), 258 - 267

756 Rusconi, R., Guasto, J. S., Stocker, R. 2014. Bacterial Transport Suppressed by  
757 Fluid Shear. *Nat. Phys.* 10 (3), 212–217.

758 Schindelin, J., Arganda-Carreras, I., Frise, E., Kaynig, V., Longair, M., Pietzsch, T.,  
759 Preibisch, S., Rueden, C., Saalfeld, S., Schmid, B., Tinevez, J-Y., White, D. J.,  
760 Hartenstein, V., Eliceiri, K., Tomancak, P., Cardona, A. 2012. Fiji: an open-  
761 source platform for biological-image analysis. *Nature Methods* 9 (7), 676-682.

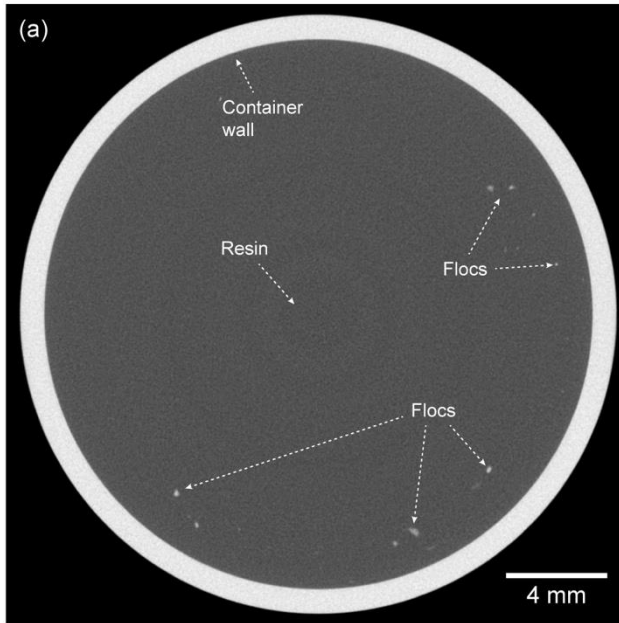
762 Sharma, S., Lin, C-L., Miller, J.D. 2017. Multi-scale features including water content  
763 of polymer induced kaolinite floc structures. *Miner. Eng.* 101, 20-29.

764 Soulsby, R.L., Manning, A.J., Spearman, J., Whitehouse, R.J.S. 2013. Settling  
765 velocity and mass settling flux of flocculated estuarine sediments. *Mar. Geol.*  
766 339, 1-12.

- 767 Tolhurst, T.J., Gust, G., Paterson, D.M. 2002. The influence on an extra-cellular  
768 polymeric substance (EPS) on cohesive sediment stability. In: Winterwerp,  
769 J.C., Kranenburg, C. (Eds.), *Fine Sediment Dynamics in the Marine  
770 Environment - Proceedings in Marine Science 5*. Elsevier Science, Amsterdam,  
771 pp. 409-425
- 772 Ward, A.K., Johnson, M.D. 1996. Heterotrophic microorganisms. In: Hauer, F.R.,  
773 Lamberti, G.A. (Eds.), *Methods in Stream Ecology*. Academic Press, San  
774 Diego, CA, pp. 233-268.
- 775 Wheatland, J.A.T., Bushby, A.J., Spencer, K.L. 2017. Quantifying the structure and  
776 composition of flocculated suspended particulate matter using focused ion  
777 beam nanotomography. *Environ. Sci. Technol.* 51 (16), 8917-8925.
- 778 Winterwerp, J.C. 1998. A simple model for turbulence induced flocculation of  
779 cohesive sediment. *J. Hyd. Eng. Res.* 36 (3), 309-326.
- 780 Zhang, N., Thompson, C.E.L., Townend, I.H., Rankin, K.E., Paterson, D.M., Manning  
781 A.J. 2018. Nondestructive 3D imaging and quantification of hydrated biofilm-  
782 sediment aggregates using X- ray microcomputed tomography. *Environ. Sci.*  
783 *Technol.* 52 (22), 13306-13313.

784

## 785 SUPPLEMENTARY FIGURES



786

787 **Supplementary Fig. S1.**  $\mu$ CT cross-sectional image from the scan of test sample

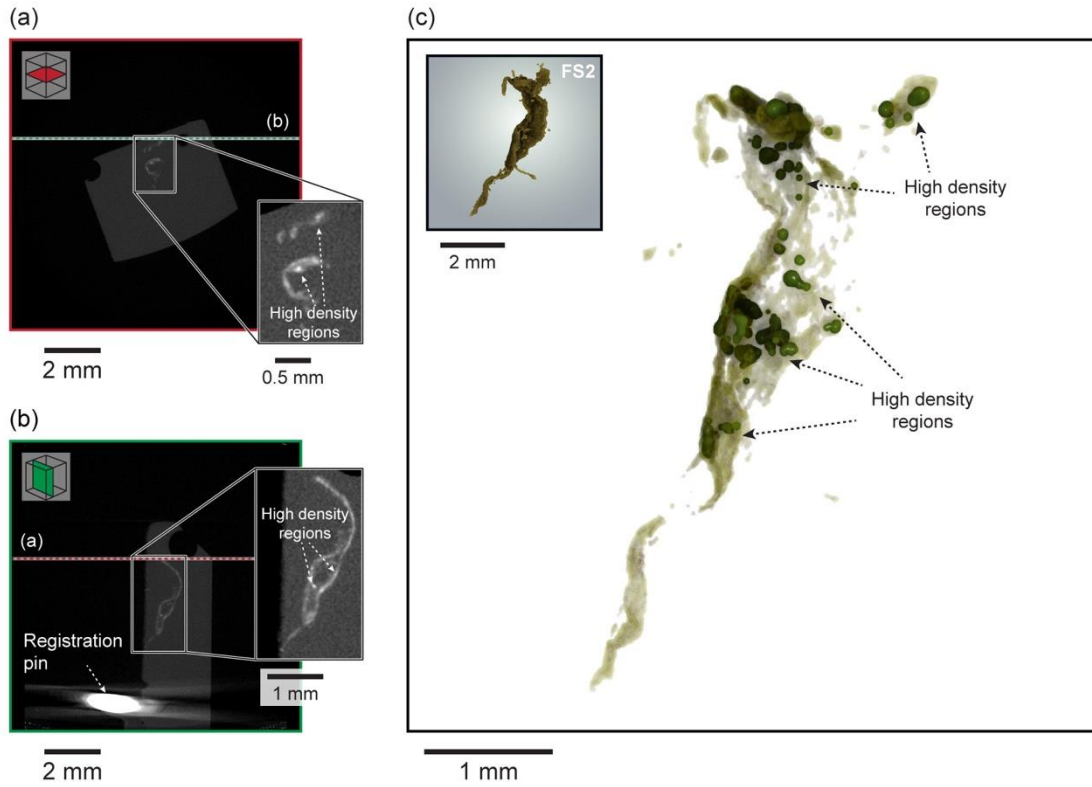
788 FS0, note the minimal overlap between neighbouring floc particles.

789

790

791

792



793

794

795

796

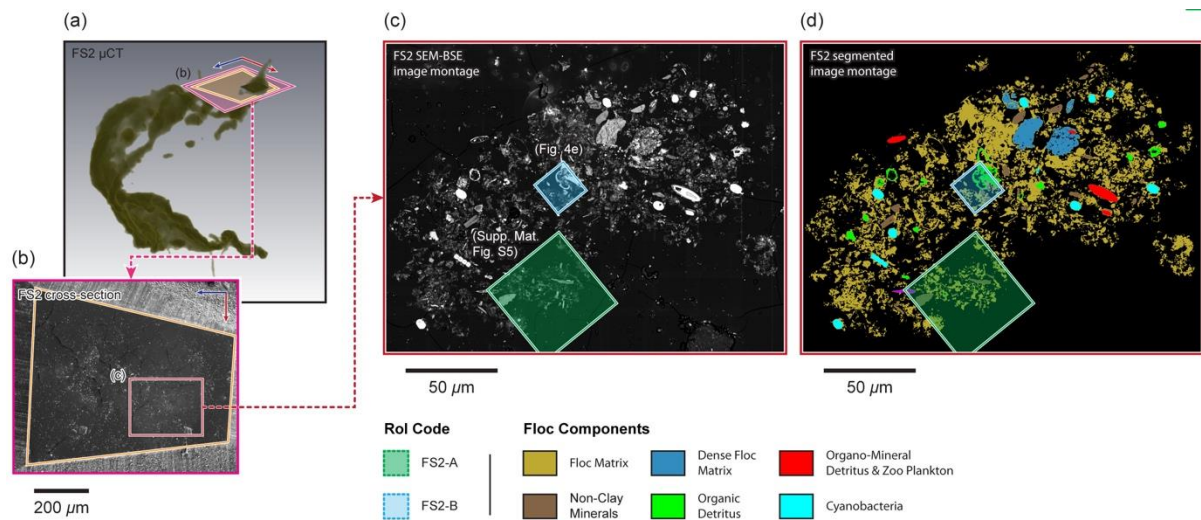
797

798

799

800

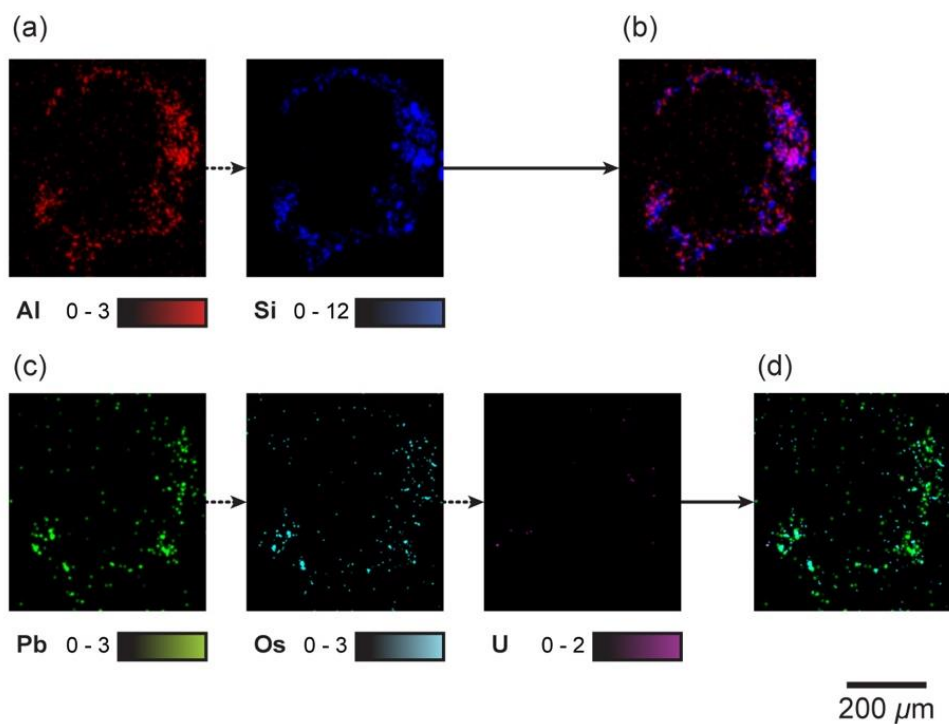
**Supplementary Fig. S2.** 3D visualisations of the floc samples FS2 (c). (a) and (b) are image slices taken in two orthogonal planes from the  $\mu$ CT data; note the regions of high and low X-ray attenuation within the floc shown in the magnified sub-sets; (c) shows a 3D visualisation of floc FS2 but with the regions of low X-ray attenuation rendered semi-transparent to reveal the regions of high attenuation.



801

802 **Supplementary Fig. S3.** Analysis of the cross-section located in floc FS2. The  
 803 location of the cross-section created within FS2 is shown in (a) and the region of the  
 804 cross-section containing the floc is shown in (b). The trapezoidal shape of the  
 805 sectioned block is highlighted in orange both in (a) and (b), while the boundary of the  
 806 SEM image of the cross-section shown in (b) is defined in 3D space in (a) in pink.  
 807 The SEM-BSE image montage (c) obtained from the cross-section through floc FS2  
 808 enabled the identification of floc constituents (d) and characterisation of floc structure  
 809 in 2D. The locations of Rols FS2-A and FS2-B selected for further analysis are  
 810 shown in (c) and (d).

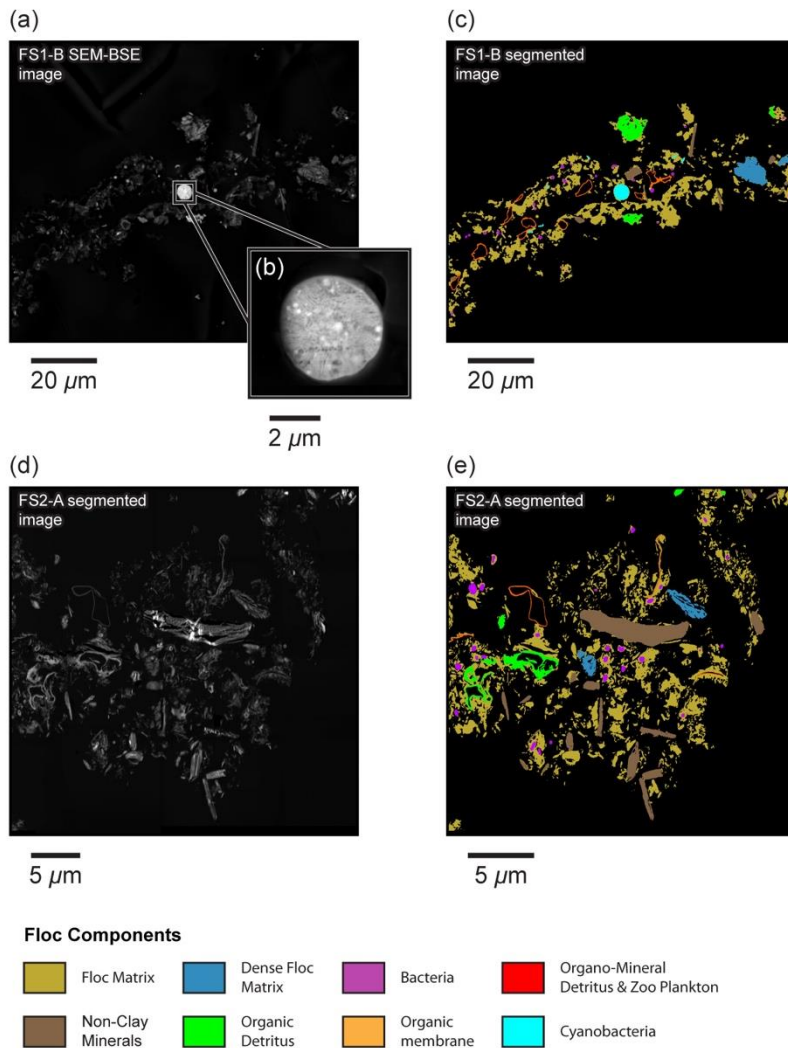
811



812

813 **Supplementary Fig. S4.** Individual SEM-EDS elemental maps collected from the  
 814 cross-section through floc FS2. (a) Inorganic signals for Al and Si; (b) combined  
 815 signal (phase map) for Al and Si; (c) Organic signals for Pb, Os, and U; (d) combined  
 816 signal for Pb, Os, and U.

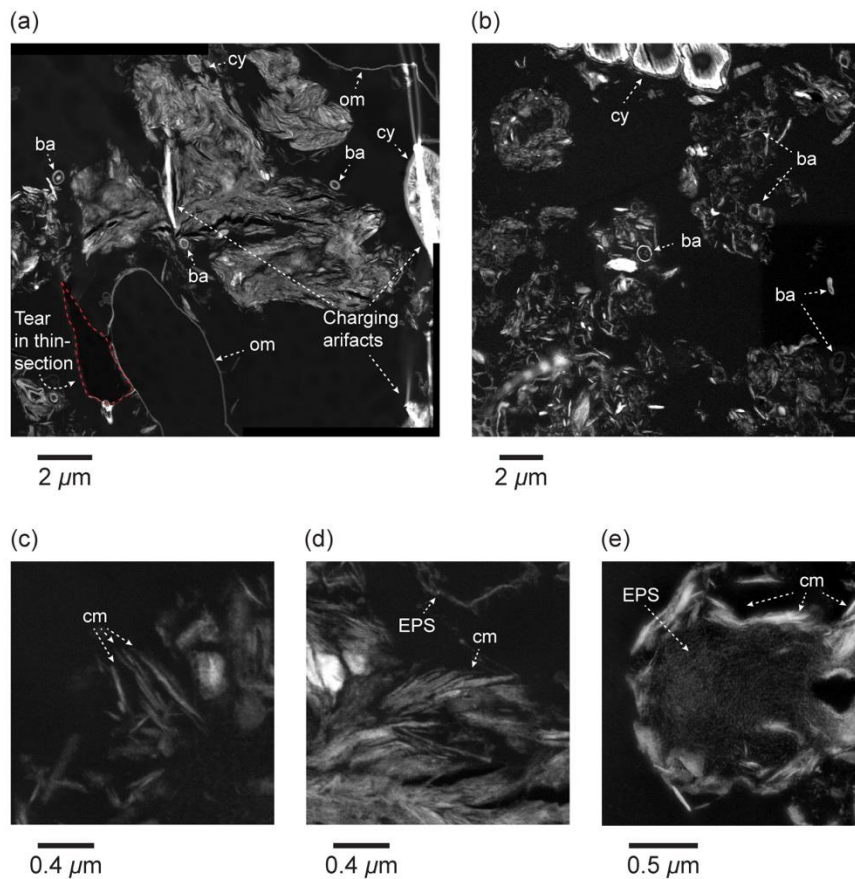
817



818

819 **Supplementary Fig. S5.** Characterisation of floc sub-micrometre composition and  
 820 structure in 2D within Rol FS1-B (a) and FS2-A (c). The locations of Rols FS1-B and  
 821 FS2-A are shown in Fig. 3c and Fig. S4 of Supplementary Materials respectively. (b)  
 822 shows a magnified subset from (a) that isolates a single cyanobacteria to  
 823 demonstrates how differential staining of subcellular structures has taken place.

824



825

826 **Supplementary Fig. S6.** Selected STEM images illustrating the materials and  
 827 structures commonly observed within flocs FS1 and FS2. Regions of high and low  
 828 (clay) particle occupation are shown in (a) and (b) respectively. Note that regions of  
 829 high occupation primarily consisted of clay minerals aligned face-to-face, whereas  
 830 low occupation regions contained a variety of materials (e.g., clays, decaying organic  
 831 detritus, bacteria etc.). The high grey-scale values (c. >70) exhibited by units of high  
 832 occupation likely relates to clays coated in organic material in the nanometre range  
 833 filling the pore space between clay minerals. Regions of lower occupation were  
 834 commonly observed to consist of sub-units composed of clay platelets aligned face-  
 835 to-face and/or edge to face (c-d) and clay minerals arranged around a central  
 836 bacteria (see Fig. 5a). EPS can be observed filling the nm and μm pores within the  
 837 floc matrix (e).

838

**Declaration of interests**

The authors declare that they have no known competing financial interests or personal relationships that could have appeared to influence the work reported in this paper.

The authors declare the following financial interests/personal relationships which may be considered as potential competing interests:

The authors declare that they have no competing interests that may have affected the work presented in this paper.